

Power output and wake effects of very large wind farms investigated by large-eddy simulations

Von der Fakultät für Mathematik und Physik
der Gottfried Wilhelm Leibniz Universität Hannover

zur Erlangung des akademischen Grades
Doktor der Naturwissenschaften
Dr. rer. nat.

genehmigte Dissertation von

M.Sc. Oliver Maas

2023

Referent: apl. Prof. Dr. Siegfried Raasch (Leibniz Universität Hannover)
1. Korreferent: Prof. Dr. Björn Maronga (Leibniz Universität Hannover)
2. Korreferent: assoz. Prof. Dr. Mostafa Bakhoday Paskyabi (Universität
Bergen, Norwegen)
Tag der Promotion: 15. November 2023

Abstract

Wind energy will be one of the most important energy sources in the carbon-neutral energy system of the future. A small but rapidly growing share of the installed wind capacity consists of offshore wind farms, which benefit from the high wind speeds and small turbulence intensities that prevail offshore. However, with the increasing expansion of offshore wind energy, these beneficial conditions are being affected by the wind farms themselves. Offshore wind farms can produce long wakes in which the wind speed is reduced and the turbulence intensity is enhanced. Additionally, the power output of the wind farm is reduced due to wake losses inside the wind farm. The aim of this thesis is to investigate the power output and wake effects of large (multi-gigawatt) wind farms with large-eddy simulations. Wind farms of this size have never been investigated before.

The results show that the flow in large wind farms is more complex than in small (sub-gigawatt) wind farms. Large wind farms cause a counterclockwise flow deflection in the order of 10° due to a reduced Coriolis force inside the wind farm. The wind farm induced speed deficit spreads into the entire boundary layer and causes the flow to diverge in the vertical direction. This results in a vertical displacement of the inversion layer, which excites stationary gravity waves in the free atmosphere. The gravity waves affect the pressure distribution near the surface and cause a significant flow blockage resulting in speed deficits of approximately 10% upstream of the wind farm. Smaller wind farms can also excite gravity waves, but their amplitude and blockage effect is much weaker. Simulations with wind farms that have a finite size in both lateral directions show that large wind farms cause a significant flow divergence in the crosswise direction. Large wind farms generate wakes with a length in the order of 100 km. Longer wakes (in terms of wind speed deficit) occur for shallower boundary layers and smaller turbine spacings. The effect of the atmospheric stability on the wake length could not clearly be stated because this parameter can not be changed without affecting others. The wake length in terms of turbulence intensity was found to be in the order of 10 km and to be independent of the wind farm size.

In the simulated cases, large wind farms achieved wind farm efficiencies of only 41% – 64% in contrast to 66% – 88% for small wind farms. The boundary layer height significantly affects the efficiency of large wind farms but not the efficiency of small wind farms. Energy budget analyses have shown that the advection of kinetic energy by the mean flow is the largest energy source for small wind farms. However, for large wind farms the largest energy source is the vertical turbulent flux of kinetic energy. For large wind farms the energy input by the geostrophic forcing becomes more dominant. This source is also enhanced by an increase in the ageostrophic wind speed component resulting from the counterclockwise flow deflection. A comparison with analytical wake models shows that their power output prediction deviates from the large-eddy simulation results by up to 40% and that they can not reproduce the flow complexity of large wind farms. The reason is that the wake models neglect relevant physical processes and energy sources and sinks. Further large-eddy simulation case studies with a systematic variation of the relevant parameters are needed to learn more about the flow behavior in large wind farms and to improve existing wake models.

Keywords: very large wind farms; power output, wake effects, large-eddy simulation

Contents

List of Abbreviations

1	Introduction	1
1.1	Current knowledge about wind farm flows and wind farm power output . . .	2
1.1.1	Wind farm flow	3
1.1.2	Wind farm power output	5
2	Methods	7
2.1	The large-eddy simulation model PALM	7
2.1.1	Governing equations and subgrid-scale models	7
2.1.2	Wind turbine model	9
2.2	Energy budget analysis	13
2.2.1	Derivation of an equation for the conservation of kinetic energy	13
2.2.2	Averaging in time	14
2.2.3	Integration over a control volume	16
3	Wake properties and power output of very large wind farms	21
3.1	Declaration of Contributions	21
3.2	Research Article	21
4	From gigawatt to multi-gigawatt wind farms	47
4.1	Declaration of Contributions	47
4.2	Research Article	47
5	Large-eddy simulation of a 15 GW wind farm	71
5.1	Declaration of Contributions	71
5.2	Research Article	71
6	Summary and open research questions	87
6.1	Summary	87
6.2	Open research questions	89
	Acknowledgements	91
	Bibliography	93
	Curriculum Vitae	99

List of Abbreviations

BL	Boundary layer
CBL	Convective boundary layer
DNS	Direct numerical simulation
IEA	International Energy Agency
IL	Inversion layer
IRENA	International Renewable Energy Agency
KE	Kinetic energy
LES	Large-eddy simulation
NBL	Neutral boundary layer
NREL	National Renewable Energy Laboratory
PALM	Parallelized Large-eddy Simulation Model
RANS	Reynolds-averaged Navier-Stokes
SBL	Stable boundary layer
SGS	Subgrid-scale

1 Introduction

Wind energy will be one of the most important energy sources in the carbon-neutral energy system of the future (IEA, 2022). Already today, wind energy makes up more than 10 % of the globally installed electricity generation capacity (IRENA, 2023). A small but rapidly growing share of the installed wind capacity consists of offshore wind farms. Despite the higher installation costs of offshore wind farms, they can compete with the low cost of onshore wind energy due to the high wind speeds and small turbulence intensities present offshore. However, with the increasing expansion of offshore wind energy, these beneficial conditions are being affected by the wind farms themselves. Offshore wind farms can produce long wakes in which the wind speed is reduced and the turbulence intensity is enhanced. Additionally, the power output of the wind farm is reduced due to wake losses inside the wind farm. The term wind farm efficiency is often used to quantify these farm-internal wake losses. The wind farm efficiency is the ratio of the actual wind farm power to the power that the wind farm would produce if all wind turbines would be located in free-stream conditions.

The wind farm efficiency and the length of the wake depends on the meteorological conditions and the wind farm properties. Smaller wind farm efficiencies and longer wakes occur for stable stratifications, shallow boundary layers and small turbine spacings (Dörenkämper et al., 2015; Ghaisas et al., 2017; Hansen et al., 2012; Nilsson et al., 2015; Platis et al., 2018; Witha et al., 2014). More recent research results show that large wind farms can trigger gravity waves in the overlying free atmosphere, which induce pressure gradients in the boundary layer. These pressure gradients cause significant flow blockage in front of the wind farm, resulting in a wind speed and power reduction already in the first turbine row (Bleeg et al., 2018; Allaerts and Meyers, 2019; Wu and Porté-Agel, 2017).

The above described knowledge about wind farm flows is based on measurements and simulations for wind farms that have a size of currently existing wind farms. These wind farms have a length of approximately 10 km and a rated power below 1 GW. Future wind farm clusters will have a length of up to 100 km and a rated power of more than 10 GW. Thus it is questionable whether the above described results are still valid for wind farm clusters of this scale. These wind farm clusters do not exist yet and can therefore only be studied by simulations. Because the wind turbine power is proportional to the third power of the wind speed, these simulations must be very accurate. The most accurate simulation technique that is still computationally feasible is large-eddy simulation (LES). LES models resolve the largest, most energetic turbulent eddies in the atmospheric boundary layer and can thus capture relevant processes like the turbulent transport of energy and momentum.

The aim of this thesis is to study the power output and flow effects of multi-gigawatt wind farms with LES and to answer these questions:

- How to design an LES setup that is suitable for simulating the flow in large wind farms?
- What are the fundamental differences between the flow in small (sub-gigawatt) and large (multi-gigawatt) wind farms and why do they occur?
- How does the wind farm wake of a large wind farm depend on the stability and the boundary layer height?
- Which wind farm efficiencies can be achieved in large wind farms and how do they depend on the stability, boundary layer height and turbine spacing?

- What are the most important energy sources and sinks in a large wind farm?
- How do analytical wake models perform for large wind farms and how can they be improved?

These questions are answered in three research articles that can be found in Sects. 3, 4 and 5.

The first article is an LES case study of potential wind farms in the German Bight. The wind farms have a total capacity of up to 20 GW, which corresponds to the planned offshore wind capacity for the selected areas (BSH, 2022). Different stabilities, boundary layer heights and turbine spacings are investigated to determine their effect on the wind farm flow and power output.

The aim of the second article is to compare small wind farms with large wind farms more systematically than it was possible in the first article. The comparison is made between two wind farms that have a length of 13 km and 90 km. The wind farms are effectively infinitely wide due to cyclic boundary conditions in the crosswise direction. The more idealized setup allows for a more quantitative evaluation of the results. An energy budget analysis is made to identify the most relevant energy sources and sinks inside small and large wind farms.

The aim of the third article is to simulate a 15 GW wind farm with a finite width and to compare the results with analytical wake models. Discrepancies between the models are explained by investigating the energy budgets inside the wind farm. In this study the wind farm has a finite width to include effects that may arise due to the wind farm boundaries that are not present in the second study.

1.1 Current knowledge about wind farm flows and wind farm power output

This section shall give a short overview of the current knowledge about wind farm flows. The focus will be on LES studies, but references to Reynolds-averaged Navier-Stokes (RANS) simulations and measurements are also made. LES studies of wind farm flows can be categorized into three different types of wind farm setups:

1. **Infinite wind farm setup:** The wind farm is effectively infinitely large in both lateral directions due to cyclic boundary conditions in both lateral directions.
2. **Semi-infinite wind farm setup:** The wind farm is effectively infinitely wide in the crosswise direction due to cyclic boundary conditions in that direction, but has a finite length in the streamwise direction.
3. **Finite wind farm setup:** The wind farm has a finite length and width.

The infinite wind farm setup may contain only one wind turbine, representing an infinite array of wind turbines due to the cyclic boundary conditions along the two lateral directions. The turbine spacing is equal to the domain length in the respective direction. This setup was used in the first LES studies of wind farm flows due to its simple implementation and low computational cost. Examples are Abkar and Porté-Agel (2013), Abkar and Porté-Agel (2014), Calaf et al. (2010), Calaf et al. (2011), Johnstone and Coleman (2012), Lu and Porté-Agel (2011), Lu and Porté-Agel (2015), Meyers and Meneveau (2010), Meyers and Meneveau (2013), Porté-Agel et al. (2014) and VerHulst and Meneveau (2014). Using this strategy allows to study the flow in an infinitely large wind farm, also called fully-developed wind farm flow. The results show that boundary layers that contain a wind farm are thicker and have a greater ageostrophic wind speed component than boundary layers without a wind

farm. The higher ageostrophic wind speed component increases the energy input by the geostrophic forcing (synoptic-scale pressure gradient). This energy is transported down to the wind farm level by the vertical turbulent flux of kinetic energy and is, to a large extent, extracted by the wind turbines. The drawback of the infinite wind farm setup is that it is very unrealistic and does not allow to study the global blockage effect, the wind farm wake or any other effect that may arise from the discontinuity at a wind farm leading and trailing edge. These effects can be studied with the semi-infinite wind farm setup.

In the semi-infinite wind farm setup, the wind farm has a finite length in the streamwise direction. In the crosswise direction, the wind farm extends to the domain boundaries, which are cyclic, so that the wind farm is still infinitely wide. This setup can not use cyclic boundary conditions in the streamwise direction because then the wake flow would reenter at the inflow. Designing a robust and realistic setup is thus more difficult than in the infinite wind farm case. Details about how this problem can be solved are provided in the method sections in all of the three research articles of this thesis. Examples for this kind of setup can be found in Allaerts and Meyers (2016), Allaerts and Meyers (2017), Allaerts and Meyers (2018), Andersen et al. (2015), Centurelli et al. (2021), Segalini and Chericoni (2021), Stevens et al. (2016), Wu and Porté-Agel (2017) and Zhang et al. (2019). The results of these studies are presented together with the finite wind farm studies.

The finite wind farm setup typically also uses cyclic boundary conditions in the crosswise direction to allow for wind veer and turbulence at these boundaries. However, the domain is wider than the wind farm, so that the wind farm has a finite width (in the crosswise direction). Studies that use this kind of setup either use an idealized wind farm layout or a layout of an existing, real wind farm. Examples can be found in Dörenkämper et al. (2015), Ghaisas et al. (2017), Lanzilao and Meyers (2022), Nilsson et al. (2015), Porté-Agel et al. (2013), Witha et al. (2014) and Wu and Porté-Agel (2015).

In the following, the results of the semi-infinite and finite wind farm studies as well as results from measurements will be reviewed. The effect of the wind farm on the flow field will be discussed first, and afterwards the focus will be on the wind farm power output. It is important to note that all the presented results are based on relatively small wind farms. Wind farm lengths range from 4.8 km (Lanzilao and Meyers, 2022) to 18.9 km (Andersen et al., 2015) in the semi-infinite wind farm studies and from 2.38 km (Witha et al., 2014) to 14.85 km (Lanzilao and Meyers, 2022) in the finite wind farm studies. However, future wind farm clusters will have a length of up to 100 km so that the flow might behave very differently than described below. Wind farms of this size have never been investigated before and it is the aim of this thesis to fill this research gap.

1.1.1 Wind farm flow

According to Porté-Agel et al. (2020), the flow through a wind farm can be categorized into five different regions:

- Induction region
- Entrance region
- Fully-developed region
- Exit region

The induction region is located upstream of the wind farm and is characterized by a wind speed reduction that is related to the so-called global blockage effect. Field measurements (Bleeg et al., 2018) as well as simulations (Allaerts and Meyers, 2019; Wu and Porté-Agel, 2017) have shown that the wind speed reduction $2.5 D$ upstream of the wind farm can be as

large as 9 %, especially for shallow boundary layers and large wind farms. The speed deficit is much greater than a linear superposition of the induction/blockage effect of the individual turbines (Centurelli et al., 2021). The reason for the significant speed deficit is a positive pressure gradient in the induction region. This pressure gradient is induced by stationary gravity waves in the free atmosphere, which are excited by the upward displacement of the inversion layer above the wind farm (Allaerts and Meyers, 2017). Since the wind turbine power is proportional to the third power of the wind speed, this speed reduction causes a significant reduction in the power of the wind turbines in the first row. However, inside the wind farm, the pressure gradient is negative and tends to accelerate the flow and increase the turbine power. Consequently, the gravity wave induced pressure gradients redistribute energy from upstream parts of the wind farm to downstream parts of the wind farm (Allaerts and Meyers, 2017; Lanzilao and Meyers, 2022).

The entrance region is located at the entrance of the wind farm. It is a transition region between the undisturbed flow in the induction region and the fully-developed region further downstream. In this region, the momentum extraction by the wind turbines is not balanced by momentum-adding processes like the vertical turbulent flux of kinetic energy or pressure gradients so that the wind speed decreases in the streamwise direction and the turbine power decreases accordingly. The wind speed deficit at turbine level spreads into the above lying boundary layer by turbulent momentum exchange, so that an internal boundary layer forms above the wind farm. For neutrally stratified boundary layers the internal boundary layer grows according to Elliot's $x^{4/5}$ power law, where x is the distance from the wind farm leading edge (Elliott, 1958; Stevens et al., 2016; Allaerts and Meyers, 2016, 2017). In the entrance region most of the energy is provided by flow deceleration (streamwise divergence of kinetic energy advection) and the vertical turbulent flux of kinetic energy. Due to the flow deceleration and the mass conservation constraint the flow diverges in the vertical direction and a significant amount of kinetic energy is lost by vertical advection (Allaerts and Meyers, 2017; Segalini and Chericoni, 2021).

The fully-developed region is characterized by an approximately constant wind speed and turbine power along the streamwise direction. The momentum extraction by the wind turbines is balanced by the vertical turbulent flux of kinetic energy from the overlying boundary layer, the energy input by the geostrophic forcing and the pressure gradients. LES studies have shown that the transition to the fully-developed region can take 100 times the boundary layer height and that sometimes no fully-developed region exists (Wu and Porté-Agel, 2017; Allaerts and Meyers, 2017). While the flow might be in balance in the streamwise direction, it is not in balance in the crosswise direction due to the reduction in Coriolis force. This imbalance results in a counterclockwise wind direction change (Allaerts and Meyers, 2016).

The exit region is located at the downstream part of the wind farm and is characterized by an increase in wind speed and a potential increase in turbine power. This effect is caused by a negative pressure gradient that is induced by stationary gravity waves above the wind farm (Allaerts and Meyers, 2017; Wu and Porté-Agel, 2017). The strength of that effect depends on the lapse rate in the free atmosphere (Smith, 2009). The exit region only exists for wind farms that are large enough to excite gravity waves.

The wake region is the region downstream of the wind farm in which the wind speed and the turbulence intensity have not yet recovered to the level present upstream of the induction region. As aircraft measurements have shown, offshore wind farm wakes can be several tens of kilometers long in case of stable boundary layers (Platis et al., 2018). Wind speed deficits and wake lengths are larger in stable boundary layers and smaller in convective boundary layers. This behavior is caused by higher turbulence intensities and thus a more effective entrainment of momentum into the wake in convective boundary layers (Witha et al., 2014; Dörenkämper et al., 2015; Ghaisas et al., 2017). Van Der Laan and Nørmark Sørensen (2017)

have shown that the wake of a single wind turbine or a small wind farm is deflected clockwise (on the northern hemisphere). This effect is explained by a vertical exchange of crosswise momentum between the wind farm layer and the above lying boundary layer in which the wind is veered to the right. Allaerts and Meyers (2016), however, have shown that for larger wind farms the wake is deflected counterclockwise by $2 - 3^\circ$ due to a reduction in Coriolis force in the wind farm and that this effect is greater for shallower boundary layers.

1.1.2 Wind farm power output

A good relative measure for the wind farm performance is the wind farm efficiency. The wind farm efficiency is the ratio of the actual wind farm power to the power that the wind farm would produce if all wind turbines were located in free-stream conditions. In many measurement and simulation studies it is assumed that the first turbine row of a wind farm experiences free-stream conditions and that the power of these turbines can be used as a reference to calculate the wind farm efficiency. However, this strategy neglects the global blockage effect and can thus result in a significant overestimation of the wind farm efficiency (Allaerts et al., 2018). Consequently, it is important to use an isolated wind turbine to define the reference power. In field measurement campaigns such a turbine often does not exist but in simulation studies the reference power can easily be obtained by performing a separate simulation with only one turbine.

The wind farm efficiency depends on many meteorological parameters such as the turbulence intensity, the surface layer stability, the boundary layer height and the free atmosphere lapse rate. The wind farm efficiency also depends on wind farm parameters such as the turbine spacing and the turbine configuration (aligned/staggered).

Higher wind farm efficiencies are achieved in convective boundary layers due to higher turbulence intensities and thus shorter wakes compared to neutral and stable boundary layers (Hansen et al., 2012; Nilsson et al., 2015; Ghaisas et al., 2017; Witha et al., 2014). Higher wind farm efficiencies are achieved for thick boundary layers because they contain more kinetic energy than shallow boundary layers (Allaerts and Meyers, 2016). The free atmosphere lapse rate affects the wavelength of the stationary gravity waves that are triggered by a wind farm and thus also affects the wind farm efficiency. Wu and Porté-Agel (2017) have shown that a greater lapse rate in the free atmosphere results in a greater global blockage effect. The annual effect of self-induced gravity waves on the power output of a 4 GW wind farm is $4 - 6\%$ (Allaerts et al., 2018).

A smaller turbine spacing increases the wind farm power output because there are more turbines per surface area but decreases the wind farm efficiency due to increased wake losses. For staggered turbine configurations the power output primarily depends on the geometric mean of the streamwise and crosswise turbine spacing. However, for aligned turbine configurations the power output primarily depends on the streamwise spacing (Stevens et al., 2016). A vertical staggering of the turbines, i.e. using different hub heights, is only effective in the entrance region. In the fully-developed region there is no benefit because the power is limited by the vertical turbulent flux of kinetic energy (Zhang et al., 2019).

2 Methods

Wind farm flows can be studied by field measurements, wind tunnel measurements or simulations. Simulations can be performed with non-turbulence-resolving models that only describe the mean flow (Reynolds-averaged Navier-Stokes, RANS) or with turbulence-resolving methods. Simulations that resolve turbulence on all scales are called direct numerical simulations (DNS). A DNS of atmospheric flows usually requires a grid spacing on the order of 1 mm and is thus not computationally feasible for the simulation of wind farm flows that require domain sizes on the order of 10^4 km^3 . The simulation method applied in this thesis is called large-eddy simulation (LES). LES models resolve only the largest turbulent eddies and require grid spacings on the order of 10 m for turbine wake resolving simulations. For a typical domain size of $100 \text{ km} \times 100 \text{ km} \times 1 \text{ km}$, this results in 10 billion grid points, which is a grid size that is manageable on modern supercomputers. Compared with measurements, simulations have the big advantage that the meteorological and wind farm parameters can be freely chosen and are exactly known. Additionally, all variables of interest can be output at every point in space and time without measurement error. Coriolis and buoyancy effects are considered, which is usually impossible for wind tunnel experiments. In contrast to RANS models, LES models resolve the largest, most energetic turbulent eddies, which is crucial to accurately capture the turbulent energy exchange in wind farm flows. Parameterization errors are usually small because only the small, less energetic eddies are parameterized. However, LES also has some disadvantages: The simulations are computationally expensive, so only a few simulations can be performed. The domain layout and boundary conditions have to be chosen with great care to avoid the introduction of artificial and unrealistic effects. For example, the mean flow and the turbulence at the inflow must be in a steady state to avoid horizontal gradients in the model domain. The grid spacing must be chosen small enough to resolve the turbulence in the boundary layer and the wind turbine wakes.

2.1 The large-eddy simulation model PALM

2.1.1 Governing equations and subgrid-scale models

The large-eddy simulations in this thesis are carried out with the Parallelized Large-eddy Simulation Model **PALM**. PALM is developed at the Institute of Meteorology and Climatology of the Leibniz University Hannover, Germany. An extensive description of PALM can be found in Maronga et al. (2015) and Maronga et al. (2020). In the following, only the parts that are relevant for this study are described.

PALM solves the non-hydrostatic, incompressible Navier-Stokes equations in Boussinesq-approximated form. In this thesis the effects of humidity are neglected. The equations for the conservation of mass, momentum and thermal energy then are:

$$\frac{\partial u_j}{\partial x_j} = 0, \quad (2.1)$$

$$\frac{\partial u_i}{\partial t} = -\frac{\partial u_i u_j}{\partial x_j} - \epsilon_{ijk} f_j u_k + \epsilon_{i3j} f_3 u_{g,j} - \frac{1}{\rho_0} \frac{\partial \pi^*}{\partial x_i} + g \frac{\theta - \langle \theta \rangle}{\langle \theta \rangle} \delta_{i3} - \frac{\partial}{\partial x_j} \tau_{ij} + d_i, \quad (2.2)$$

$$\frac{\partial \theta}{\partial t} = -\frac{\partial u_j \theta}{\partial x_j} - \frac{\partial}{\partial x_j} (\widetilde{u_j'' \theta''}), \quad (2.3)$$

where angular brackets indicate horizontal averaging, a double prime indicates subgrid-scale (SGS) quantities, a tilde denotes filtering over a grid volume and is omitted for a better readability except for the SGS temperature flux ($\widetilde{u_j''\theta''}$). The velocity components are u_i ($u_1 = u$, $u_2 = v$, $u_3 = w$), the spatial coordinates are x_i ($x_1 = x$, $x_2 = y$, $x_3 = z$) with $i, j, k \in \{1, 2, 3\}$, θ is potential temperature, t is time, $f_i = (0, 2\Omega \cos(\phi), 2\Omega \sin(\phi))$ is the Coriolis parameter with the Earth's angular velocity $\Omega = 0.729 \times 10^{-4} \text{ rad s}^{-1}$ and the geographical latitude ϕ . The geostrophic wind speed components are $u_{g,j}$ and the basic state density of dry air is ρ_0 . The modified perturbation pressure is $\pi^* = p + \frac{2}{3}\rho_0 e$, where p is the perturbation pressure and $e = \frac{1}{2}\widetilde{u_i''u_i''}$ is the SGS turbulence kinetic energy. The gravitational acceleration is $g = 9.81 \text{ m s}^{-2}$, δ is the Kronecker delta, $\tau_{ij} = (\widetilde{u_i''u_j''} - \frac{2}{3}e\delta_{ij})$ is the deviatoric stress tensor and d_i are the forces of the wind turbine model, which is described in Sec. 2.1.2.

The turbulence closure, i.e. the parameterization of the SGS covariance terms $\widetilde{u_i''u_j''}$ and $\widetilde{u_j''\theta''}$, is performed by a 1.5-order closure after Deardorff (1980). Two different modified versions of this closure are used in this thesis:

- **Deardorff model:** SGS model proposed by Deardorff (1980), modified by Moeng and Wyngaard (1988) and Saiki et al. (2000).
- **Dai model:** SGS model proposed by Dai et al. (2021), which is based on the Deardorff model.

The turbulence closure of the Deardorff model assumes that the SGS flux is proportional to the local gradient of the respective resolved-scale flow quantity:

$$\begin{aligned} \widetilde{u_i''u_j''} - \frac{2}{3}e\delta_{ij} &= -K_m \left(\frac{\partial u_i}{\partial x_j} + \frac{\partial u_j}{\partial x_i} \right), \\ \widetilde{u_j''\theta''} &= -K_h \frac{\partial \theta}{\partial x_j}, \end{aligned} \quad (2.4)$$

where K_m and K_h are the local SGS eddy diffusivities of momentum and heat, respectively:

$$\begin{aligned} K_m &= c_m l \sqrt{e}, \\ K_h &= \left(1 + \frac{2l}{\Delta} \right) K_m, \end{aligned} \quad (2.5)$$

where $c_m = 0.1$ and Δ is the geometric mean of the grid spacings in the three directions:

$$\Delta = (\Delta x \Delta y \Delta z)^{1/3}. \quad (2.6)$$

The mixing length l is calculated as

$$l = \begin{cases} \min(1.8z, \Delta, L_b) & \text{for } \frac{\partial \theta}{\partial z} > 0 \\ \min(1.8z, \Delta) & \text{for } \frac{\partial \theta}{\partial z} \leq 0 \end{cases} \quad (2.7)$$

and depends on the height z , Δ and, in case of a locally stable stratification, the buoyancy length scale L_b :

$$L_b = 0.76 \frac{\sqrt{e}}{N}. \quad (2.8)$$

Here, N is the Brunt-Väisälä frequency:

$$N = \sqrt{\frac{g}{\theta} \frac{\partial \theta}{\partial z}}. \quad (2.9)$$

The SGS turbulence kinetic energy is calculated with the following prognostic equation:

$$\frac{\partial e}{\partial t} = -u_j \frac{\partial e}{\partial x_j} - \left(\widetilde{u_i'' u_j''} \right) \frac{\partial u_i}{\partial x_j} + \frac{g}{\langle \theta \rangle} \widetilde{u_3'' \theta''} - \frac{\partial}{\partial x_j} \left[u_j'' \left(\widetilde{e + \frac{p''}{\rho_0}} \right) \right] - \epsilon, \quad (2.10)$$

where ϵ is the SGS dissipation rate within a grid volume, calculated as:

$$\epsilon = \left(0.19 + 0.74 \frac{l}{\Delta} \right) \frac{e^{3/2}}{l} \quad (2.11)$$

and the pressure term is calculated as follows:

$$- \left[u_j'' \left(\widetilde{e + \frac{p''}{\rho_0}} \right) \right] = -2K_m \frac{\partial e}{\partial x_j}. \quad (2.12)$$

The Dai model was developed to reduce the grid spacing sensitivity of the Deardorff model for stable boundary layer simulations. As shown by Dai et al. (2021), the Dai model produces much less grid spacing sensitive results than the Deardorff model. It also allows for coarser grid spacings in stable boundary layers, making the simulation of very large wind farms computationally feasible. For the Dai model the mixing length calculation changes to:

$$l = \begin{cases} \left(\frac{1}{\kappa z} + \frac{1}{L_b} \right)^{-1} & \text{for } \frac{\partial \theta}{\partial z} > 0 \\ \min(1.8z, \Delta) & \text{for } \frac{\partial \theta}{\partial z} \leq 0, \end{cases} \quad (2.13)$$

where $\kappa = 0.4$ is the von Kármán constant. The eddy diffusivities are calculated as follows:

$$K_h = \begin{cases} K_m & \text{for } \frac{\partial \theta}{\partial z} > 0 \\ 3K_m & \text{for } \frac{\partial \theta}{\partial z} \leq 0. \end{cases} \quad (2.14)$$

2.1.2 Wind turbine model

The effect of wind turbines on the atmospheric flow is parameterized by the wind turbine model, which is part of PALM. An advanced actuator disc model with rotation (ADM-R) is used to model the effect of the rotor disc on the flow. The actuator disc is a permeable disc that imposes axial and tangential forces on the flow. The axial forces represent the rotor thrust and extract momentum from the flow. The tangential forces represent the rotor torque and add angular momentum in the opposite direction of the rotational direction of the rotor, so that the wake rotates. Including these rotational effects comes with nearly no additional computational cost but results in a better representation of real wakes (Steinfeld et al., 2015; Wu and Porté-Agel, 2015). The term *advanced* means that the disc is subdivided into several rings and each ring is subdivided into several segments to account for a nonuniform distribution of forces inside the disc that may arise from a turbulent and sheared inflow velocity field (see Fig. 2.1).

The axial and tangential force f_a and f_t at each disc segment are calculated from the lift and drag force f_l and f_d that the rotor blades would generate at this radial position:

$$\begin{aligned} f_a &= f_l \cos \phi + f_d \sin \phi, \\ f_t &= f_l \sin \phi - f_d \cos \phi, \end{aligned} \quad (2.15)$$

where ϕ is the angle between the velocity vector \mathbf{v}_{rel} and the rotor disc (see Fig. 2.2) and f_l

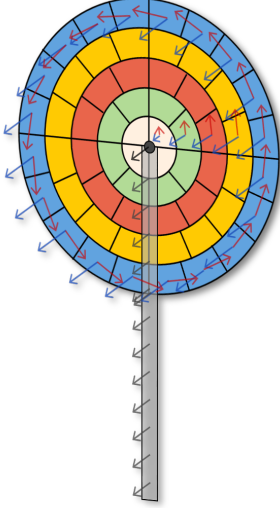


Figure 2.1: Schematic of the actuator disc model with rotation. The actuator disc is subdivided into several segments for which the axial and tangential forces are calculated. Also shown are the drag forces of the tower (not used in this thesis). Figure taken from the PALM documentation: <https://palm.muk.uni-hannover.de/trac/wiki/doc/tec/wtm>.

and f_d are the lift and drag forces, calculated as follows:

$$\begin{aligned} f_l &= \frac{1}{2} \rho v_{rel}^2 c_l s A, \\ f_d &= \frac{1}{2} \rho v_{rel}^2 c_d s A. \end{aligned} \quad (2.16)$$

Here, ρ is the air density, c_l and c_d are the lift and drag coefficient of the blade profile at that radial position, A is the area of the disc segment and s is the solidity factor, describing the percentage of the circumference that is covered with blades at that radial position r :

$$s = \frac{N_b l_c}{2\pi r}, \quad (2.17)$$

where $N_b = 3$ is the number the rotor blades and l_c is the chord length of the rotor blade profile (see Fig. 2.2). The axial and tangential forces of all N_s disc segments are used to calculate the thrust force F_{rot} and the torque M_{rot} of the entire rotor disc:

$$\begin{aligned} F_{rot} &= \sum_{i=1}^{N_s} f_{a,i}, \\ M_{rot} &= \sum_{i=1}^{N_s} f_{t,i} r_i, \end{aligned} \quad (2.18)$$

where r_i is the radial position of the respective segment center. The mechanical power provided by the rotor is

$$P_{rot} = M_{rot} \omega_{rot}, \quad (2.19)$$

where ω_{rot} is the rotational speed of the rotor given in radians per second. A change in the rotational speed of the rotor is determined by an imbalance between the rotor torque M_{rot}

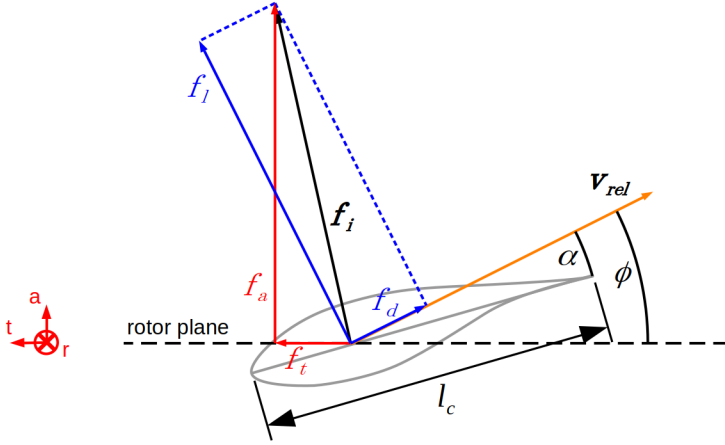


Figure 2.2: Rotor blade section with chord length l_c at radius r . Shown are the angle of attack α , the inflow angle ϕ , the inflow velocity relative to the blade section \mathbf{v}_{rel} , the aerodynamic force generated by the blade section \mathbf{f}_i , which can be decomposed into lift force f_l and drag force f_d or into an axial force f_a and tangential force f_t .

and the generator torque M_{gen} :

$$\frac{\partial \omega}{\partial t} = \frac{M_{rot} - M_{gen}}{I}, \quad (2.20)$$

where I is the moment of inertia of the entire drive train. In this thesis, the 15 MW reference wind turbine of the National Renewable Energy Laboratory (NREL) is used, which has a direct drive so that no gear ratio has to be taken into account (Gaertner et al., 2020). The generator torque is determined by a torque controller with a characteristic speed-torque-curve, as shown in Fig. 2.3. The torque controller is an adapted version of the controller of the NREL 5 MW reference wind turbine (Jonkman et al., 2009) because implementing the controller of the 15 MW turbine would add unnecessary complexity to the wind turbine model. In this thesis, the wind turbines operate in region 2 (below rated power) in which both controllers prescribe a torque curve that results in the optimal tip speed ratio and power coefficient.

The axial and tangential forces in Eq. (2.15) do not only affect the wind turbine performance but also affect the surrounding flow field. The segment forces are distributed onto the surrounding grid points by a smearing kernel η to avoid numerical instabilities:

$$\mathbf{f}(x, y, z) = \sum_{i=1}^N -\mathbf{f}_i \eta(d), \quad (2.21)$$

where $\mathbf{f}(x, y, z)$ is the force vector at a grid point, \mathbf{f}_i is the force vector at a disc segment and d is the distance between the grid point and the center of the disc segment. Note the negative sign that transforms the forces that act on the rotor disc into forces that act on the flow (Newton's third law of motion). Often a Gaussian smearing kernel is used, e.g. in Wu and Porté-Agel (2011):

$$\eta_G(d) = \frac{1}{\epsilon^3 \pi^{3/2}} \exp\left(-\frac{d^2}{\epsilon^2}\right), \quad (2.22)$$

where ϵ is a parameter that defines the width of the Gaussian smearing kernel. However, this

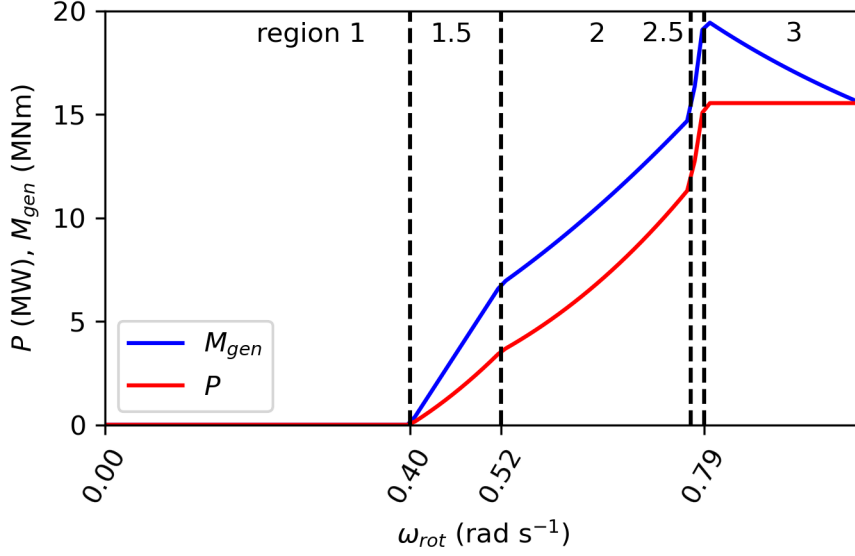


Figure 2.3: Torque-speed relationship of the torque controller. M is the generator torque set by the controller and P is the resulting mechanical generator power (before electric losses).

equation can not be computed efficiently so that in PALM the Gaussian smearing kernel is approximated by a smearing kernel that is based on a fourth order polynomial (see Fig. 2.4):

$$\eta(d) = \begin{cases} \frac{1}{\epsilon^3 \pi^{3/2}} \left[\left(\frac{1}{\epsilon_0^4} d^4 - \frac{2}{\epsilon_0^2} d^2 \right) + 1 \right] & \text{for } d < \epsilon_0 \\ 0 & \text{for } d \geq \epsilon_0. \end{cases} \quad (2.23)$$

Here, ϵ_0 is the distance at which the polynomial becomes zero and thus defines the size of the smearing kernel. It is chosen in such a way that the volume integrals of η_G and η have the same value, so that the sum of the smeared forces is the same for both methods:

$$\epsilon_0 = \left(\frac{105}{32} \right)^{\frac{1}{3}} \pi^{\frac{1}{6}} \epsilon \approx 1.798 \epsilon. \quad (2.24)$$

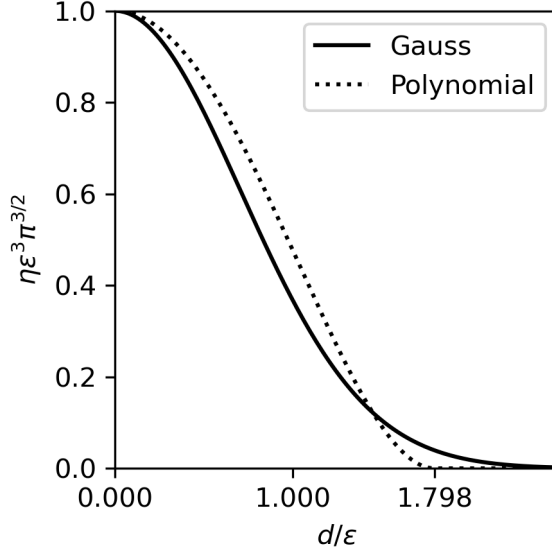


Figure 2.4: Smearing kernel based on Gaussian distribution (η_G) and smearing kernel based on a fourth-order polynomial (η) with distance to disc segment d and kernel width ϵ .

2.2 Energy budget analysis

The second and third research article in this thesis contain an energy budget analysis to identify relevant energy sources and sinks inside wind farms. The methodology of this energy budget analysis is described only briefly to keep the articles short. However, the details of the methodology might be of great value to anybody who wants to perform a similar energy budget analysis with PALM. The aim of this section is to derive the required equations and to show which data output is required. To obtain an equation for the kinetic energy budget of the resolved-scale flow inside a control volume three steps have to be taken:

1. Derive an equation for the conservation of kinetic energy (KE) from PALM's equation for the conservation of momentum (Multiply the momentum equation with u_i).
2. Average in time and assume stationarity.
3. Integrate over the control volume.

2.2.1 Derivation of an equation for the conservation of kinetic energy

An equation for the conservation of KE can be obtained by multiplying PALM's equation for the conservation of momentum (Eq. 2.2) with u_i :

$$\underbrace{u_i \frac{\partial u_i}{\partial t}}_1 = -\underbrace{u_i \frac{\partial u_i u_j}{\partial x_j}}_2 - \underbrace{\epsilon_{ijk} f_j u_i u_k}_3 + \underbrace{u_i \epsilon_{i3j} f_3 u_{g,j}}_4 - \underbrace{\frac{1}{\rho_0} \frac{\partial \pi^*}{\partial x_i} u_i}_5 + \underbrace{g \frac{\theta - \langle \theta \rangle}{\langle \theta \rangle} \delta_{i3} u_i}_6 + \underbrace{u_i \frac{\partial}{\partial x_j} \tau_{ij}}_7 + \underbrace{u_i d_i}_8. \quad (2.25)$$

The meaning of the individual terms is:

1. Rate of change of KE with $\text{KE} = E_k = \frac{1}{2} u_i u_i$.
2. Divergence of advection of KE.

3. Work done by the Coriolis force. This term is zero because the Coriolis force always acts perpendicular to the velocity and thus does no work on the flow:

$$\begin{aligned}
 \epsilon_{ijk} f_j u_i u_k &= \epsilon_{i1k} f_1 u_i u_k + \epsilon_{i2k} f_2 u_i u_k + \epsilon_{i3k} f_3 u_i u_k \\
 &= \epsilon_{213} f_1 u_2 u_3 + \epsilon_{312} f_1 u_3 u_2 + \epsilon_{123} f_2 u_1 u_3 + \epsilon_{321} f_2 u_3 u_1 + \epsilon_{132} f_3 u_1 u_2 + \epsilon_{231} f_3 u_2 u_1 \\
 &= (-f_1 u_2 u_3 + f_1 u_3 u_2) + (+f_2 u_1 u_3 - f_2 u_3 u_1) + (-f_3 u_1 u_2 + f_3 u_2 u_1) \\
 &= 0.
 \end{aligned} \tag{2.26}$$

4. Work done by the geostrophic forcing:

$$u_i \epsilon_{ij3} f_3 u_{g,j} = u_2 \epsilon_{231} f_3 u_{g,1} + u_1 \epsilon_{132} f_3 u_{g,2} = u_2 f_3 u_{g,1} - u_1 f_3 u_{g,2}. \tag{2.27}$$

5. Work done by the perturbation pressure gradient.
 6. Work done by buoyancy, which can only be done on the vertical velocity component u_3 .
 7. Work done by the SGS shear stress.
 8. Work done by the wind turbines.

With the above made rearrangements the equation reads as follows:

$$\underbrace{\frac{1}{2} \frac{\partial u_i u_i}{\partial t}}_1 = \underbrace{-\frac{1}{2} \frac{\partial u_i u_i u_j}{\partial x_j}}_2 \underbrace{-0}_3 + \underbrace{(u_2 f_3 u_{g,1} - u_1 f_3 u_{g,2})}_4 - \underbrace{\frac{1}{\rho_0} \frac{\partial \pi^*}{\partial x_i} u_i}_5 + \underbrace{g \frac{\theta - \langle \theta \rangle}{\langle \theta \rangle} u_3}_6 + \underbrace{u_i \frac{\partial}{\partial x_j} \tau_{ij}}_7 + \underbrace{u_i d_i}_8. \tag{2.28}$$

2.2.2 Averaging in time

Averaging equation 2.28 in time gives:

$$\underbrace{\overline{\frac{1}{2} \frac{\partial u_i u_i}{\partial t}}}_1 = \underbrace{-\overline{\frac{1}{2} \frac{\partial u_i u_i u_j}{\partial x_j}}}_2 \underbrace{-\overline{0}}_3 + \underbrace{\overline{(u_2 f_3 u_{g,1} - u_1 f_3 u_{g,2})}}_4 - \underbrace{\overline{\frac{1}{\rho_0} \frac{\partial \pi^*}{\partial x_i} u_i}}_5 + \underbrace{\overline{g \frac{\theta - \langle \theta \rangle}{\langle \theta \rangle} u_3}}_6 + \underbrace{\overline{u_i \frac{\partial \tau_{ij}}{\partial x_j}}}_7 + \underbrace{\overline{u_i d_i}}_8. \tag{2.29}$$

The Reynolds decomposition is applied, which decomposes a variable v into a mean part \bar{v} and a fluctuating part v' :

$$v = \bar{v} + v'. \tag{2.30}$$

The Reynolds averaging rules are applied during the averaging process:

- $\overline{v'} = 0$
- $\overline{c v} = c \bar{v}$, where c is a constant
- $\overline{u + v} = \bar{u} + \bar{v}$
- $\overline{(\bar{u} v)} = \bar{u} \bar{v}$
- $\overline{\frac{\partial v}{\partial x}} = \frac{\partial \bar{v}}{\partial x}$.

The following assumptions and rearrangements can be made:

- Term 1: Assume stationarity:

$$\frac{1}{2} \frac{\overline{\partial u_i u_i}}{\partial t} = 0 \quad (2.31)$$

- Term 2: Split the velocity components into a mean and a fluctuating part ($u_i = \bar{u}_i + u'_i$):

$$\begin{aligned} -\frac{1}{2} \frac{\overline{\partial u_i u_i u_j}}{\partial x_j} &= -\frac{1}{2} \frac{\partial}{\partial x_j} \left(\overline{(\bar{u}_i + u'_i)(\bar{u}_i + u'_i)(\bar{u}_j + u'_j)} \right) \\ &= -\frac{\partial}{\partial x_j} \left(\frac{1}{2} (\bar{u}_i \bar{u}_i + \overline{u'_i u'_i}) \bar{u}_j + \bar{u}_i \overline{u'_i u'_j} + \frac{1}{2} \overline{u'_i u'_i u'_j} \right) \\ &= -\frac{\partial}{\partial x_j} \left(\bar{u}_j \bar{E}_k + \bar{u}_i \overline{u'_i u'_j} + \frac{1}{2} \overline{u'_i u'_i u'_j} \right) \end{aligned} \quad (2.32)$$

- Term 5: Split the velocity components and the perturbation pressure into a mean and a fluctuating part ($u_i = \bar{u}_i + u'_i$, $\pi^* = \bar{\pi}^* + \pi^{*'}$):

$$\begin{aligned} -\frac{1}{\rho_0} \frac{\overline{\partial \pi^*}}{\partial x_i} u_i &= -\frac{1}{\rho_0} \frac{\overline{\partial (\bar{\pi}^* + \pi^{*'})}}{\partial x_i} (\bar{u}_i + u'_i) \\ &= -\frac{1}{\rho_0} \left(\frac{\partial \bar{\pi}^*}{\partial x_i} \bar{u}_i + \frac{\partial \bar{\pi}^*}{\partial x_i} u'_i + \frac{\partial \pi^{*'}}{\partial x_i} \bar{u}_i + \frac{\partial \pi^{*'}}{\partial x_i} u'_i \right) \\ &= -\frac{1}{\rho_0} \left(\frac{\partial \bar{\pi}^*}{\partial x_i} \bar{u}_i + \frac{\partial \bar{\pi}^*}{\partial x_i} u'_i + \frac{\partial \pi^{*'}}{\partial x_i} \bar{u}_i + \frac{\partial \pi^{*'}}{\partial x_i} u'_i \right) \\ &= -\frac{1}{\rho_0} \left(\frac{\partial \bar{\pi}^*}{\partial x_i} \bar{u}_i + \frac{\partial \pi^{*'}}{\partial x_i} u'_i \right) \end{aligned} \quad (2.33)$$

- Term 7: Split term into two terms using the product rule:

$$u_i \frac{\overline{\partial \tau_{ij}}}{\partial x_j} = \frac{\overline{\partial u_i \tau_{ij}}}{\partial x_j} - \tau_{ij} \frac{\partial u_i}{\partial x_j} \quad (2.34)$$

This results in:

$$\begin{aligned} 0 &= -\frac{\partial}{\partial x_j} \left(\bar{u}_j \bar{E}_k + \bar{u}_i \overline{u'_i u'_j} + \frac{1}{2} \overline{u'_i u'_i u'_j} \right) + \bar{u}_2 f_3 u_{g,1} - \bar{u}_1 f_3 u_{g,2} \\ &\quad - \frac{1}{\rho_0} \left(\frac{\partial \bar{\pi}^*}{\partial x_i} \bar{u}_i + \frac{\partial \pi^{*'}}{\partial x_i} u'_i \right) + g \frac{\overline{\theta - \langle \theta \rangle}}{\langle \theta \rangle} u_3 + \frac{\overline{\partial u_i \tau_{ij}}}{\partial x_j} - \tau_{ij} \frac{\partial u_i}{\partial x_j} + \overline{u_i d_i}. \end{aligned} \quad (2.35)$$

2.2.3 Integration over a control volume

Integrating Eq. (2.35) over the control volume Ω and regrouping the terms gives:

$$\begin{aligned}
 0 = & - \underbrace{\int_{\Omega} \frac{\partial \bar{u}_j \bar{E}_k}{\partial x_j} d\Omega}_{\mathcal{A}} - \underbrace{\int_{\Omega} \frac{\partial}{\partial x_j} \bar{u}_i \overline{u'_i u'_j} d\Omega}_{\mathcal{F}} + \underbrace{\int_{\Omega} \frac{\partial}{\partial x_j} \bar{u}_i \overline{\tau_{ij}} d\Omega}_{\mathcal{F}} - \underbrace{\int_{\Omega} \frac{\partial}{\partial x_j} \frac{1}{2} \overline{u'_j u'_i u'_i} d\Omega}_{\mathcal{F}} - \underbrace{\int_{\Omega} \frac{u'_i}{\rho_0} \frac{\partial \pi^{*i}}{\partial x_i} d\Omega}_{\mathcal{F}} \\
 & + \underbrace{\int_{\Omega} (\bar{u}_2 f_3 u_{g,1} - \bar{u}_1 f_3 u_{g,2}) d\Omega}_{\mathcal{G}} - \underbrace{\int_{\Omega} \frac{\bar{u}_i}{\rho_0} \frac{\partial \pi^*}{\partial x_i} d\Omega}_{\mathcal{P}} + \underbrace{\int_{\Omega} g \frac{\overline{\theta - \langle \theta \rangle}}{\langle \theta \rangle} u_3 d\Omega}_{\mathcal{B}} \\
 & - \underbrace{\int_{\Omega} \overline{\tau_{ij} \frac{\partial u_i}{\partial x_j}} d\Omega}_{\mathcal{D}} - \underbrace{\mathcal{R} + \int_{\Omega} \overline{u_i d_i} d\Omega}_{\mathcal{W}},
 \end{aligned} \tag{2.36}$$

The terms of Eq. (2.36) are categorized as follows:

\mathcal{A} : Divergence of the advection of KE

\mathcal{F} : Divergence of the turbulent fluxes of KE

\mathcal{G} : Energy input by the geostrophic forcing

\mathcal{P} : Energy input by mean perturbation pressure gradients

\mathcal{B} : Energy input by buoyancy forces

\mathcal{D} : Dissipation by SGS model less the residual \mathcal{R}

\mathcal{W} : Energy extraction by the wind turbines.

Equation (2.36) has a positive residual \mathcal{R} because the magnitude of the calculated dissipation is underestimated, which has two reasons: First, the local velocity gradients are underestimated because they are calculated with central differences. Second, the 5th order upwind advection scheme of Wicker and Skamarock (2002) has numerical dissipation, suppressing the magnitude of the smallest eddies, for which the gradients and the dissipation are highest (Maronga et al., 2013). The positive residual is subtracted from the negative dissipation term \mathcal{D} to compensate for the underestimated magnitude of the calculated dissipation.

The terms in \mathcal{A} and \mathcal{F} are volume integrals of a divergence of a quantity, which can be converted to surface integrals of the quantity itself (Gauss's theorem), allowing for a much faster computation:

$$\mathcal{A} = \underbrace{\left[\int_{\Gamma_x} (-\bar{u}_1 \bar{E}_k) d\Gamma_x \right]_{x_l}^{x_r}}_{\mathcal{A}_x} + \underbrace{\left[\int_{\Gamma_y} (-\bar{u}_2 \bar{E}_k) d\Gamma_y \right]_{y_s}^{y_n}}_{\mathcal{A}_y} + \underbrace{\left[\int_{\Gamma_z} (-\bar{u}_3 \bar{E}_k) d\Gamma_z \right]_{z_b}^{z_t}}_{\mathcal{A}_z}, \tag{2.37}$$

$$\begin{aligned}
 \mathcal{F} = & \underbrace{\left[\int_{\Gamma_x} \left(-\bar{u}_i \overline{u'_i u'_1} + \overline{u_i \tau_{i1}} - \frac{1}{2} \overline{u'_1 u'_i u'_i} - \frac{\overline{u'_1 \pi^{*i}}}{\rho_0} \right) d\Gamma_x \right]_{x_l}^{x_r}}_{\mathcal{F}_x} + \\
 & \underbrace{\left[\int_{\Gamma_y} \left(-\bar{u}_i \overline{u'_i u'_2} + \overline{u_i \tau_{i2}} - \frac{1}{2} \overline{u'_2 u'_i u'_i} - \frac{\overline{u'_2 \pi^{*i}}}{\rho_0} \right) d\Gamma_y \right]_{y_s}^{y_n}}_{\mathcal{F}_y} + \\
 & \underbrace{\left[\int_{\Gamma_z} \left(-\bar{u}_i \overline{u'_i u'_3} + \overline{u_i \tau_{i3}} - \frac{1}{2} \overline{u'_3 u'_i u'_i} - \frac{\overline{u'_3 \pi^{*i}}}{\rho_0} \right) d\Gamma_z \right]_{z_b}^{z_t}}_{\mathcal{F}_z}.
 \end{aligned} \tag{2.38}$$

Here, \mathcal{A}_x , \mathcal{A}_y and \mathcal{A}_z are the advection of KE through the left/right boundaries (Γ_x), south/north boundaries (Γ_y) and bottom/top boundaries (Γ_z), respectively (see Fig. 2.5). The terms \mathcal{F}_x , \mathcal{F}_y and \mathcal{F}_z are the turbulent fluxes through the left/right, south/north and bottom/top boundaries, respectively.

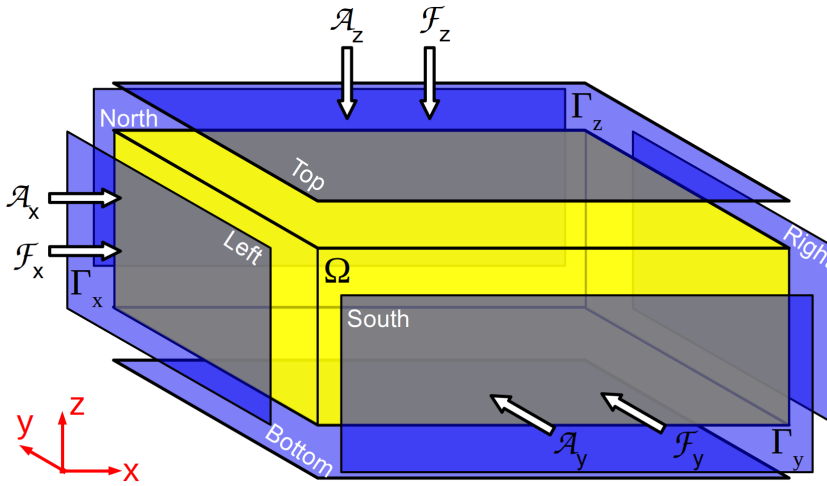


Figure 2.5: Schematic of the control volume Ω and its boundaries Γ_x , Γ_y and Γ_z .

To show more clearly which data output is required, the summation convention in the first three terms of \mathcal{F} is broken up:

$$\begin{aligned}
 \mathcal{F}_{1x} &= - \left[\int_{\Gamma_x} \bar{u}_i \overline{u'_i u'_1} d\Gamma_x \right]_{x_l}^{x_r} = - \left[\int_{\Gamma_x} (\bar{u} \overline{u' u'} + \bar{v} \overline{v' u'} + \bar{w} \overline{w' u'}) d\Gamma_x \right]_{x_l}^{x_r}, \\
 \mathcal{F}_{1y} &= - \left[\int_{\Gamma_y} \bar{u}_i \overline{u'_i u'_2} d\Gamma_y \right]_{y_s}^{y_n} = - \left[\int_{\Gamma_y} (\bar{u} \overline{u' v'} + \bar{v} \overline{v' v'} + \bar{w} \overline{w' v'}) d\Gamma_y \right]_{y_s}^{y_n}, \\
 \mathcal{F}_{1z} &= - \left[\int_{\Gamma_z} \bar{u}_i \overline{u'_i u'_3} d\Gamma_z \right]_{z_b}^{z_t} = - \left[\int_{\Gamma_z} (\bar{u} \overline{u' w'} + \bar{v} \overline{v' w'} + \bar{w} \overline{w' w'}) d\Gamma_z \right]_{z_b}^{z_t},
 \end{aligned} \tag{2.39}$$

$$\begin{aligned}
 \mathcal{F}_{2x} &= \left[\int_{\Gamma_x} \overline{u_i \tau_{i1}} d\Gamma_x \right]_{x_l}^{x_r} = \left[\int_{\Gamma_x} (\overline{u} \tau_{11} + \overline{v} \tau_{21} + \overline{w} \tau_{31}) d\Gamma_x \right]_{x_l}^{x_r}, \\
 \mathcal{F}_{2y} &= \left[\int_{\Gamma_y} \overline{u_i \tau_{i2}} d\Gamma_y \right]_{y_s}^{y_n} = \left[\int_{\Gamma_y} (\overline{u} \tau_{12} + \overline{v} \tau_{22} + \overline{w} \tau_{32}) d\Gamma_y \right]_{y_s}^{y_n}, \\
 \mathcal{F}_{2z} &= \left[\int_{\Gamma_z} \overline{u_i \tau_{i3}} d\Gamma_z \right]_{z_b}^{z_t} = \left[\int_{\Gamma_z} (\overline{u} \tau_{13} + \overline{v} \tau_{23} + \overline{w} \tau_{33}) d\Gamma_z \right]_{z_b}^{z_t},
 \end{aligned} \tag{2.40}$$

$$\begin{aligned}
 \mathcal{F}_{3x} &= - \left[\int_{\Gamma_x} \frac{1}{2} \overline{u'_1 u'_i u'_i} d\Gamma_x \right]_{x_l}^{x_r} = - \frac{1}{2} \left[\int_{\Gamma_x} (\overline{u' u' u'} + \overline{u' v' v'} + \overline{u' w' w'}) d\Gamma_x \right]_{x_l}^{x_r}, \\
 \mathcal{F}_{3y} &= - \left[\int_{\Gamma_y} \frac{1}{2} \overline{u'_2 u'_i u'_i} d\Gamma_y \right]_{y_s}^{y_n} = - \frac{1}{2} \left[\int_{\Gamma_y} (\overline{v' u' u'} + \overline{v' v' v'} + \overline{v' w' w'}) d\Gamma_y \right]_{y_s}^{y_n}, \\
 \mathcal{F}_{3z} &= - \left[\int_{\Gamma_z} \frac{1}{2} \overline{u'_3 u'_i u'_i} d\Gamma_z \right]_{z_b}^{z_t} = - \frac{1}{2} \left[\int_{\Gamma_z} (\overline{w' u' u'} + \overline{w' v' v'} + \overline{w' w' w'}) d\Gamma_z \right]_{z_b}^{z_t}.
 \end{aligned} \tag{2.41}$$

The product of the fluctuations in the above equations (e.g. $\overline{w' u' u'}$) can not be computed directly because the mean value of the respective quantity is not known during the simulation. However, these products can be calculated in the post-processing, if the product of the absolute values (e.g. $\overline{w u u}$, $\overline{u u}$, $\overline{w u}$) is computed and part of the output:

$$\begin{aligned}
 \overline{w' u' u'} &= \overline{(w - \overline{w})(u - \overline{u})(u - \overline{u})} = \overline{(w - \overline{w})(u^2 - 2u\overline{u} + \overline{u}^2)} \\
 &= \overline{w u^2} - \overline{w u} \overline{u} - 2\overline{w u \overline{u}} + 2\overline{w} \overline{u \overline{u}} + \overline{w \overline{u}^2} - \overline{w} \overline{u}^2 \\
 &= \overline{w u^2} - \overline{w} \overline{u}^2 - 2\overline{w u} \overline{u} + 2\overline{w} \overline{u}^2.
 \end{aligned} \tag{2.42}$$

Table 2.1 lists the output quantities required for the calculation of all terms in Eq. (2.36). All first-order moments and second-order moments of the velocity components are required. Additionally, all third-order moments except for $\overline{w v w}$ are required. The calculation of the buoyancy term (\mathcal{B}) and the Dissipation term (\mathcal{D}) is performed online during the simulation. The user code that generates this output, as well as the post-processing script that calculates the terms of Eq. 2.36 is available at the Research Data Repository of the Leibniz University Hannover (Maas, 2022).

Table 2.1: Required output quantities for the energy budget analysis.

Quantity	Used in term	Quantity	Used in term
1 \bar{u}	$\mathcal{A}, \mathcal{F}, \mathcal{G}, \mathcal{P}$	19 \overline{www}	\mathcal{F}_3
2 \bar{v}	$\mathcal{A}, \mathcal{F}, \mathcal{G}, \mathcal{P}$	20 $\overline{u\tau_{11}}$	\mathcal{F}_2
3 \bar{w}	$\mathcal{A}, \mathcal{F}, \mathcal{P}$	21 $\overline{u\tau_{12}}$	\mathcal{F}_2
4 \overline{uu}	$\mathcal{A}, \mathcal{F}_1, \mathcal{F}_3$	22 $\overline{u\tau_{13}}$	\mathcal{F}_2
5 \overline{uv}	$\mathcal{F}_1, \mathcal{F}_3$	23 $\overline{v\tau_{21}}$	\mathcal{F}_2
6 \overline{uw}	$\mathcal{F}_1, \mathcal{F}_3$	24 $\overline{v\tau_{22}}$	\mathcal{F}_2
7 \overline{vv}	$\mathcal{A}, \mathcal{F}_1, \mathcal{F}_3$	25 $\overline{v\tau_{23}}$	\mathcal{F}_2
8 \overline{vw}	$\mathcal{F}_1, \mathcal{F}_3$	26 $\overline{w\tau_{31}}$	\mathcal{F}_2
9 \overline{ww}	$\mathcal{A}, \mathcal{F}_1, \mathcal{F}_3$	27 $\overline{w\tau_{32}}$	\mathcal{F}_2
10 \overline{uuu}	\mathcal{F}_3	28 $\overline{w\tau_{33}}$	\mathcal{F}_2
11 \overline{uuv}	\mathcal{F}_3	29 $\overline{\pi^*}$	$\mathcal{P}, \mathcal{F}_4$
12 \overline{uuw}	\mathcal{F}_3	30 $\overline{u\pi^*}$	\mathcal{F}_4
13 \overline{uvv}	\mathcal{F}_3	31 $\overline{v\pi^*}$	\mathcal{F}_4
14 \overline{uvw}	-	32 $\overline{w\pi^*}$	\mathcal{F}_4
15 \overline{www}	\mathcal{F}_3	33 $\overline{g \frac{\theta - \langle \theta \rangle}{\langle \theta \rangle} u_3}$	\mathcal{B}
16 \overline{vvv}	\mathcal{F}_3	34 $\overline{\tau_{ij} \frac{\partial u_i}{\partial x_j}}$	\mathcal{D}
17 \overline{vww}	\mathcal{F}_3	35 $\overline{u_i d_i}$	\mathcal{W}
18 \overline{vww}	\mathcal{F}_3		

3 Wake properties and power output of very large wind farms for different meteorological conditions and turbine spacings: a large-eddy simulation case study for the German Bight

3.1 Declaration of Contributions

O. Maas and S. Raasch selected and designed the simulated cases. O. Maas performed the simulations and wrote the manuscript. Data analysis and manuscript preparation were guided by S. Raasch. The paper was edited by Sandrine Aubrun and reviewed by Dries Allaerts and one anonymous referee.

3.2 Research Article

Maas, O. and Raasch, S.: Wake properties and power output of very large wind farms for different meteorological conditions and turbine spacings: a large-eddy simulation case study for the German Bight, *Wind Energy Science*, 7, 715–739, doi: 10.5194/wes-7-715-2022, 2022.
©The authors 2021. CC BY 4.0 License

Wind Energ. Sci., 7, 715–739, 2022
<https://doi.org/10.5194/wes-7-715-2022>
 © Author(s) 2022. This work is distributed under
 the Creative Commons Attribution 4.0 License.



Wake properties and power output of very large wind farms for different meteorological conditions and turbine spacings: a large-eddy simulation case study for the German Bight

Oliver Maas and Siegfried Raasch

Institute of Meteorology and Climatology, Leibniz University Hannover, Hanover, Germany

Correspondence: Oliver Maas (maas@meteo.uni-hannover.de)

Received: 2 August 2021 – Discussion started: 23 August 2021

Revised: 17 February 2022 – Accepted: 27 February 2022 – Published: 25 March 2022

Abstract. Germany’s expansion target for offshore wind power capacity of 40 GW by the year 2040 can only be reached if large portions of the Exclusive Economic Zone in the German Bight are equipped with wind farms. Because these wind farm clusters will be much larger than existing wind farms, it is unknown how they will affect the boundary layer flow and how much power they will produce. The objective of this large-eddy simulation study is to investigate the wake properties and the power output of very large potential wind farms in the German Bight for different turbine spacings, stabilities and boundary layer heights. The results show that very large wind farms cause flow effects that small wind farms do not. These effects include, but are not limited to, inversion layer displacement, counterclockwise flow deflection inside the boundary layer and clockwise flow deflection above the boundary layer. Wakes of very large wind farms are longer for shallower boundary layers and smaller turbine spacings, reaching values of more than 100 km. The wake in terms of turbulence intensity is approximately 20 km long, in which longer wakes occur for convective boundary layers and shorter wakes for stable boundary layers. Very large wind farms in a shallow, stable boundary layer can excite gravity waves in the overlying free atmosphere, resulting in significant flow blockage. The power output of very large wind farms is higher for thicker boundary layers because thick boundary layers contain more kinetic energy than thin boundary layers. The power density of the energy input by the geostrophic pressure gradient limits the power output of very large wind farms. Because this power density is very low (approximately 2 W m^{-2}), the installed power density of very large wind farms should be small to achieve a good wind farm efficiency.

1 Introduction

At present, the global installed wind power capacity from offshore wind farms is increasing rapidly. According to the expansion targets of the current leading offshore wind markets (the United Kingdom, Germany and China), the offshore wind power capacity will be subject to significant growth over the next decades. The German expansion target for offshore wind power capacity is 40 GW by the year 2040, which is more than the global installed offshore wind power capacity of 32.5 GW in the year 2020 (WindSeeG, 2020; Herzig, 2020). The otherwise undisturbed flow at offshore sites will

be increasingly modified by wind farms, affecting the wind farm power output but also the meteorological conditions in the wake. For wind farms with a state-of-the-art size of approximately 100 turbines and a length of approximately 5 km, these effects have been extensively investigated experimentally and numerically and are generally well understood.

However, the size of future wind farms or clusters of wind farms will be 1 or 2 orders of magnitude larger than today’s (see Fig. 1). Because no wind farms of this size exist currently, new insights into the behavior of the flow through wind farms and the resulting power output can only be provided by simulations. The most accurate method that re-

solves all the relevant processes such as the turbulent momentum and heat transport that is still computationally feasible is large-eddy simulation. In recent years many large-eddy simulations of wind farm flows have been carried out. A comprehensive review can be found in Porté-Agel et al. (2020). Some of the investigations consisted of an infinite wind farm setup with cyclic boundary conditions in the streamwise and crosswise directions (e.g., Lu and Porté-Agel, 2011; Calaf et al., 2011; Johnstone and Coleman, 2012). With these methods, the limiting case of an infinite wind farm can be investigated at relatively low computational cost due to the small domain size. Johnstone and Coleman (2012) used this method to compare a neutral boundary layer flow with and without wind turbines. The wind turbines increased the boundary layer height and the ageostrophic wind component inside the boundary layer, which led to a higher energy input by the pressure gradient. Simple one-dimensional models for the wind speed profile inside and above an infinite wind farm have been developed by, for example, Frandsen (1992), Calaf et al. (2010), and Abkar and Porté-Agel (2013).

Some authors used a semi-infinite wind farm setup with cyclic boundary conditions only in the crosswise direction (Stevens et al., 2016; Allaerts and Meyers, 2017; Wu and Porté-Agel, 2017). Allaerts and Meyers (2017) simulated a 15 km long wind farm in a conventionally neutral boundary layer (CNBL) with different heights. In the shallow boundary layer cases, the wind-farm-induced flow deceleration led to upward displacement of the inversion layer which triggered stationary gravity waves in the free atmosphere. These gravity waves can impose favorable and unfavorable streamwise pressure gradients upstream, inside and downstream of the wind farm, which can result in significant flow acceleration or deceleration.

Large-eddy simulations of existing wind farms have been carried out, e.g., the wind farms Horns Rev with eighty 2 MW turbines (Porté-Agel et al., 2013; Wu and Porté-Agel, 2015), Alpha Ventus with twelve 5 MW turbines, Lillgrund with 48 2.3 MW turbines (Churchfield et al., 2012; Nilsson et al., 2015) and EnBW Baltic 1 with twenty-one 2.3 MW turbines (Witha et al., 2014).

To date, there have been no studies of wind farms of finite size with variable meteorological conditions, nor have spatial and energy scales of future wind farms (on the order of 100 km and 10 GW) been investigated. With this study we want to fill this gap by performing large-eddy simulations of very large, finite size wind farms for different stabilities, turbine spacings and boundary layer heights. We provide new insights into the wake properties and power output of very large wind farms and how these depend on the varied parameters. Specifically we want to answer these questions.

1. How is the flow inside and above the boundary layer affected by very large wind farms?

2. How long is the wake in terms of speed deficit and turbulence intensity?
3. What physical processes drive the wake recovery?
4. How much power output or power density can be expected for very large wind farms?
5. What effect does the turbine spacing and the boundary layer height have on questions 1–4?

Instead of using an idealized wind farm shape, we investigate a potential future wind farm scenario in the German Bight, which is shown in Fig. 1. The scenario assumes that all priority areas for future wind farms are equipped with 15 MW wind turbines. This results in a total number of up to 2088 wind turbines with a total wind farm capacity of up to 31 GW. More than 7 billion grid points are required to fill the large domain with a turbine wake-resolving grid. The simulations were carried out on 5120 cores on one of the supercomputers of the North German Supercomputing Alliance (HLRN). A simulation required a wall-clock time of 25 to 50 h. To our knowledge, this large-eddy simulation case study exceeds other studies in terms of wind farm area and total wind turbine number by at least 1 order of magnitude.

The numerical model, setup and boundary conditions are described in Sect. 2. The simulation results regarding the wake properties and the power output are shown and discussed in Sect. 3. Section 4 concludes and discusses the results of the study.

2 Methods

2.1 Numerical model

The simulations were performed with the Parallelized Large-eddy Simulation Model (PALM) (Maronga et al., 2020), which is developed at the Institute of Meteorology and Climatology of Leibniz Universität Hannover, Germany. Several wind farm flow investigations have been successfully conducted with this code in the past (e.g., Witha et al., 2014; Dörenkämper et al., 2015). PALM solves the non-hydrostatic, incompressible Navier–Stokes equations in Boussinesq-approximated form. The equations for the conservation of mass, momentum and internal energy spatially filtered over a grid volume then read as follows:

$$\frac{\partial u_j}{\partial x_j} = 0, \quad (1)$$

$$\begin{aligned} \frac{\partial u_i}{\partial t} = & -\frac{\partial u_i u_j}{\partial x_j} - \epsilon_{ijk} f_j u_k + \epsilon_{i3j} f_3 u_{g,j} \\ & - \frac{1}{\rho_0} \frac{\partial \pi^*}{\partial x_i} + g \frac{\theta - \langle \theta \rangle}{\langle \theta \rangle} \delta_{i3} - \frac{\partial}{\partial x_j} (\overline{u_i'' u_j''}) - \frac{2}{3} e \delta_{ij}, \end{aligned} \quad (2)$$

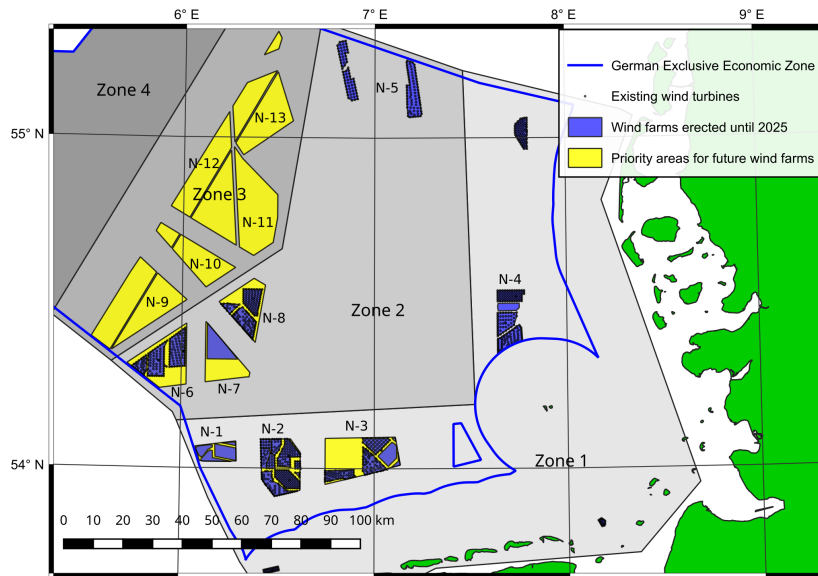


Figure 1. Existing wind farms and priority areas for future wind farms in the German Exclusive Economic Zone in the German Bight. The map is based on data that are publicly available at <https://www.geoseaportal.de> (last access: 4 March 2021).

$$\frac{\partial \theta}{\partial t} = -\frac{\partial u_j \theta}{\partial x_j} - \frac{\partial}{\partial x_j} (\overline{u_j'' \theta''}), \quad (3)$$

where angular brackets indicate horizontal averaging, and a double prime indicates subgrid-scale (SGS) quantities, $i, j, k \in \{1, 2, 3\}$, u_i, u_j, u_k are the velocity components in the respective directions (x_i, x_j, x_k) , θ is potential temperature, t is time, $f_i = (0, 2\Omega \cos(\phi), 2\Omega \sin(\phi))$ is the Coriolis parameter with the Earth's angular velocity $\Omega = 0.729 \times 10^{-4} \text{ rad s}^{-1}$ and the geographical latitude ϕ . The geostrophic wind speed components are $u_{g,j}$, and the basic state density of dry air is ρ_0 . The modified perturbation pressure is $\pi^* = p^* + \frac{2}{3} \rho_0 e$, where p^* is the perturbation pressure, and $e = \frac{1}{2} \overline{u_i'' u_i''}$ is the SGS turbulence kinetic energy. The gravitational acceleration is $g = 9.81 \text{ m s}^{-2}$, and δ is the Kronecker delta.

The SGS model uses a 1.5-order closure according to Deardorff (1980), modified by Moeng and Wyngaard (1988) and Saiki et al. (2000). Recently, the modified version of Dai et al. (2021) has been implemented in PALM, which allows for coarser grid spacings in stable boundary layers due to reduced grid spacing sensitivity. This modified version is used for the simulation of wind farms in a stable boundary layer.

The following features of PALM are relevant for the performed simulations. It is possible to prescribe a surface heating or cooling rate instead of prescribing a surface heat flux. Stable boundary layers can also be generated by imitating warm air advection by using a large-scale forcing. Convective boundary layer growth can be compensated for by ap-

plying a large-scale subsidence to the potential temperature field. A Rayleigh damping layer can be used in order to avoid gravity wave reflection at the top of the domain.

The wind turbines are represented by an advanced actuator disc model with rotation (ADM-R) that acts as an axial momentum sink and an angular momentum source (inducing wake rotation). The ADM-R is described in detail by Steinfeld et al. (2015) and Wu and Porté-Agel (2011). The actuator disc is divided into several segments along the radial and tangential directions to allow for a non-uniform thrust distribution over the disc. The lift and thrust force of each segment f_l and f_d is projected on the axial (f_a) and tangential (f_t) directions:

$$f_a = -f_l \cos \Phi - f_d \sin \Phi, \quad f_t = -f_l \sin \Phi - f_d \cos \Phi, \quad (4)$$

where Φ is the angle between the local wind vector and the disc. The rotor thrust F and torque M are then calculated as the sum over all N segments at radius r_i :

$$F = \sum_{i=1}^N f_{a,i}, \quad M = \sum_{i=1}^N f_{t,i} r_i. \quad (5)$$

The wind turbine power is calculated out of the rotational speed of the rotor n_{rotor} and the torque:

$$P = 2\pi n_{\text{rotor}} M. \quad (6)$$

To avoid numerical instabilities, the disc element forces are distributed to the neighboring grid points by a three-dimensional Gaussian smearing kernel, which is approximated by a computationally less expensive fourth-order polynomial. The smearing kernel has a default radius of $2\Delta x$,

reaching approximately 78 grid points. The otherwise two-dimensional actuator disc is enlarged in the axial and radial directions by the smearing, resulting in a power overestimation of 26.8%. The power overestimation can be reduced to 12.5% by setting the kernel radius to $1\Delta x$, reaching approximately 10 grid points, without any numerical instabilities. The thrust coefficient is overestimated by 2% for $2\Delta x$ and underestimated by 4% for $1\Delta x$. As a compromise, the smearing kernel radius is set to $1\Delta x$ for this study. The wind turbine power output is corrected for the power overestimation by a factor of $1/1.125$ before entering the wind farm power output analysis.

2.2 Case selection

To produce meaningful and relevant results, the simulations should represent the most common meteorological conditions in the German Bight. A climatology with frequency distributions of wind speed, wind direction, boundary layer (BL) height and stability information extracted from the COSMO-REA6 reanalysis dataset can be found in Appendix A. The analysis was provided by Thomas Spanghel (German Weather Service), and it is based on hourly data of a 24-year period (1995–2018) at $54^{\circ}30' \text{ N}$, $6^{\circ}00' \text{ E}$, which is located inside Zone 3 (see Fig. 1). Wind speed and direction are evaluated at 178 m height, which is the closest COSMO model level to the hub height of 150 m of the wind turbine used in the simulations.

Due to the high computational cost per simulation, only a limited number of simulations were carried out. This study consists of five simulations with varying stability, turbine spacing and BL height. An overview is given in Table 1. Two cases with a neutral boundary layer (NBL), two cases with a convective boundary layer (CBL) and one case with a stable boundary layer (SBL) are simulated.

In the two NBL cases, NBL-700-5D and NBL-700-7D, the turbine spacing is set to $s = 5D$ and $s = 7D$, where D is the rotor diameter of the turbine. The turbine spacing for all other cases is $s = 7D$. The NBL is capped by an inversion layer with a lapse rate of $\Gamma = +1 \text{ K km}^{-1}$ to achieve a BL height of approximately 700 m, which is a very common BL height in the German Bight, according to the COSMO-REA6 climatology (see Figs. A3 and A4). The correct term for such an inversion-capped NBL is *conventionally neutral boundary layer* (CNBL). However, the cases are named NBL-700-7D and NBL-700-5D to avoid confusion with the CBL cases.

Because CBLs are more frequent and are generally thicker than SBLs in the German Bight, two CBL cases, CBL-700-7D and CBL-1400-7D, with a BL height of $h \approx 700$ and $h \approx 1400$ m, respectively, are simulated. This represents the spread of CBL heights in the German Bight (see Fig. A3). Note that a CBL is the only BL type for which the BL height can be controlled freely by the initial temperature profile without the need to change other parameters. The (steady-state) BL height of CNBLs and SBLs can not be controlled

directly but is rather a function of friction velocity, Coriolis parameter, free atmosphere (FA) stratification and surface buoyancy flux (Zilitinkevich et al., 2007).

The BL height of the SBL case SBL-300-7D is $h \approx 300$ m so that the wind turbines with a rotor top height of 270 m are still within the BL and do not penetrate into the FA; 300 m is a small but still typical value for an SBL in the German Bight (see Fig. A4).

The wind speed at hub height is set to 10 m s^{-1} for all cases. This wind speed is less than the mean wind speed in the German Bight (10.8 m s^{-1} , see Fig. A1) to stay below the rated wind speed of $v_{\text{rated}} = 10.59 \text{ m s}^{-1}$ of the IEA 15 MW reference wind turbine (Gaertner et al., 2020). Thus the turbine operates at a high thrust coefficient, and the turbine power is a function of the wind speed. The surface roughness length in all cases is $z_0 = 1 \text{ mm}$. The wind direction at hub height is set to 225° by tuning the geostrophic wind direction α appropriately (see Table 1). Southwest wind is one of the most common wind directions in the German Bight. Because the main axis of the wind farm clusters in Zone 3 has a southwest–northeast orientation, strong wake effects can be expected for this wind direction.

2.3 Setup, boundary conditions, domain and wind farm layout

The domain and wind farm layout are shown in Fig. 2. The domain length and width are $L_x = 204.8 \text{ km}$ and $L_y = 163.84 \text{ km}$, respectively. These lengths correspond to $n_x = 10240$ and $n_y = 8192$ grid points in the x and y directions for isotropic grid spacings of $\Delta x = \Delta y = \Delta z = 20 \text{ m}$ for all cases. These spacings yield a density of 12 grid points per rotor diameter, which is enough to resolve the most relevant eddies inside the wind turbine wakes. As Steinfeld et al. (2015) showed, even eight grid points per rotor diameter are sufficient to obtain a converged result for the mean wind speed profiles 5D behind the turbine. Above the BL, where no turbulence must be resolved, the grid is stretched vertically to a maximum of $\Delta z_{\text{max}} = 50 \text{ m}$ to save computational cost. The stretch factor is $f_{\text{stretch}} = \Delta z(k+1)/\Delta z(k) = 1.08$ and the stretching starts at z_s (see Table 1). To damp gravity waves before they could be reflected at the domain top, Rayleigh damping is applied above the Rayleigh damping level z_{rd} with a Rayleigh damping factor of $f_{\text{rd}} = 0.01/\Delta t$, where Δt is the time step. The domain height L_z , number of vertical grid points n_z , the stretch level and the Rayleigh damping level are different for the five cases and are given in Table 1. The simulated time in all five cases is 10 h. The first 6 h are required to obtain a steady-state wind farm flow (6 h is approximately the time that the flow needs to pass the domain, i.e., $204.8 \text{ km}/10 \text{ m s}^{-1} \approx 5.7 \text{ h}$). The last 4 h are used for the evaluation, e.g., averaging and flux calculations.

At the crosswise lateral boundaries, cyclic boundary conditions are applied, and at the outflow plane, radiation boundary conditions are applied. Details about the radiation bound-

Table 1. Overview of simulated cases with boundary layer height h , turbine spacing s , surface heating rate $\dot{\theta}_0$ or large-scale forcing advection tendency $\dot{\theta}_{\text{lsf}}$ in the case of SBL-300-7D, surface heat flux $Q_{H,0}$, Monin–Obukhov length L , subsidence velocity w_{sub} , geostrophic wind speed G and direction α , length and width of the precursor domain $L_{x,\text{pre}}$ and $L_{y,\text{pre}}$, domain height L_z , number of vertical grid points n_z , stretch level z_s , and Rayleigh damping level z_{rd} .

Case unit	h m	s –	$\dot{\theta}_0 / \dot{\theta}_{\text{lsf}}$ K h^{-1}	$Q_{H,0}$ K m s^{-1}	L m	w_{sub} mm s^{-1}	G m s^{-1}	α $^\circ$	$L_{x,\text{pre}}$ km	$L_{y,\text{pre}}$ km	L_z m	n_z –	z_s m	z_{rd} m
NBL-700-7D	700	7 D	0	0	$\pm\infty$	0	10.77	8.9	5.76	4.80	2042	88	1500	1600
NBL-700-5D	700	5 D	0	0	$\pm\infty$	0	10.77	8.9	5.76	4.80	2042	88	1500	1600
CBL-700-7D	700	7 D	0.05	+0.007	–420	3.968	10.19	9.5	7.68	3.84	2042	88	1500	1600
CBL-1400-7D	1400	7 D	0.025	+0.008	–390	1.984	10.13	3.4	7.68	3.84	3595	128	2100	2500
SBL-300-7D	300	7 D	0.05	–0.004	+380	0	10.07	15.4	3.84	3.84	3624	96	700	2500

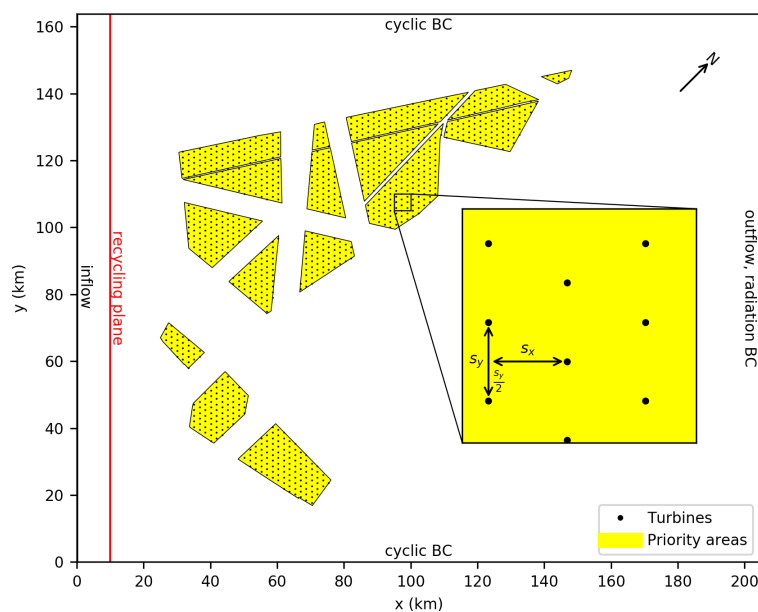


Figure 2. Domain and wind farm layout: inflow from left and turbulence recycling plane at $x = 10$ km. Priority areas for future wind farms (see Fig. 1) are filled with a regular, staggered grid of wind turbines with a streamwise and crosswise turbine spacing of $s_x = s_y = 7$ D (shown here) or 5 D.

ary condition can be found in Miller and Thorpe (1981) and Orlanski (1976). At the domain top a Neumann boundary condition is set for the perturbation pressure, and the vertical potential temperature gradient is kept constant. At the inflow plane, steady-state vertical profiles of a precursor simulation are prescribed (details about the precursor simulations are given in the next section). To have a turbulent and stationary inflow from the beginning of the main simulation, the flow field is initialized by the instantaneous flow field of the last time step of the precursor simulation. Because the precursor domain is much smaller than the main domain, the flow field is filled cyclically into the main domain. It is important to note that the width of the main domain is a non-integer multiple of the width of the precursor domain to trigger the

break-up of the unnatural periodicity in the y direction of the flow field that is introduced by the cyclic fill method.

The turbulent state of the inflow is maintained by a turbulence recycling method that maps the turbulent fluctuations from the recycling plane at $x = x_r$ onto the inflow plane at $x = 0$ (Lund et al., 1998; Kataoka and Mizuno, 2002). The turbulent fluctuation $\Psi'(y, z, t)$ at each time step is defined as the difference between the absolute value $\Psi(x_r, y, z, t)$ and the horizontal line average in the y direction $\langle \Psi(x_r, z, t) \rangle_y$ at that height:

$$\Psi'(y, z, t) = \Psi(x_r, y, z, t) - \langle \Psi(x_r, z, t) \rangle_y, \quad (7)$$

where Ψ can be a velocity component, the potential temperature or the subgrid-scale turbulent kinetic energy. The turbulent fluctuation is added to the mean inflow profile $\Psi_{\text{inflow}}(z)$

at the inflow plane. Instead of adding it at the same y location, it can be added at $y + y_{\text{shift}}$:

$$\Psi(0, y + y_{\text{shift}}, z, t) = \Psi_{\text{inflow}}(z) + \Psi'(y, z, t). \quad (8)$$

The application of the y shift effectively reduces the strength of streamwise elongated streaks in the mean wind speed of NBLs (Munters et al., 2016).¹ The otherwise inhomogeneous inflow with crosswise variations in wind speed of up to 10 % would hamper the evaluation of the wind farm power output and wake. A homogeneous inflow wind speed is of the utmost importance in wind energy studies because the wind turbine power is proportional to the third power of the wind speed. The y shift is chosen in such a way that the flow is recycled many times before reaching its initial y position, which is achieved if the least common multiple of the y shift and the domain width is a large number. The y shift is also applied to the non-NBL cases because it reduces crosswise variations in wind speed that are caused by wind-farm-induced flow blockage. The flow blockage leads to a reduced mean wind speed at some y locations of the recycling plane, which is “interpreted” as turbulent fluctuation and thus mapped onto the inflow. Test simulations without y shift showed that, due to the self-reinforcing behavior of this process, the crosswise variations in wind speed can build up to ± 2 %.

The turbulence recycling is limited to a height just above the BL height so that potential BL growth between inflow and recycling plane will not affect the inflow BL height. The recycling plane is located 10 km downstream of the inflow plane, which gives the turbulent structures enough time to interact and decorrelate before becoming recycled. For the CBL cases, the absolute value of the potential temperature is recycled instead of its turbulent fluctuation so that the inflow temperature rises according to the increasing surface temperature. This method is not needed in the SBL case because the surface temperature is constant in time (details in the next section).

The priority areas of Fig. 1 are rotated 45° clockwise so that the inflow at hub height is parallel to the x axis for a wind direction of 225°. The priority areas are filled with a regular array of the IEA 15 MW reference wind turbine that has a rotor diameter of $D = 240$ m, a hub height of

¹Elongated, streak-like structures in the instantaneous streamwise wind speed (also called superstructures or very large-scale motions) are a natural phenomenon of NBLs. However, these structures can be as large as 20 times the BL height (Fang and Porté-Agel, 2015) so that they can not be captured between inflow and recycling plane. Thus, the same structure is recycled repeatedly without breaking up or moving in the y direction. As a result, streaks of high and low wind speed appear in the averaged velocity field even for very long averaging times. A y shift does not avoid the appearance of streaks in the instantaneous velocity field, but due to the changing y location of the streaks, the strength of the streaks in the mean velocity field is reduced effectively (Munters et al., 2016).

$z_{\text{hub}} = 150$ m and a rated power of $P_{\text{rated}} = 15$ MW (Gaertner et al., 2020). The wind turbines are staggered, i.e., every second column is shifted by half a turbine spacing in the y direction (see Fig. 2). The staggered configuration represents the real-world variation in wind directions better than the very special case of an aligned configuration. Additionally, power output and wake strength are less sensitive to potential wind direction changes (that might occur further downstream inside the wind farm) for the staggered configuration, as revealed by our own test simulations with smaller wind farms. The turbine spacing in the x and y directions is the same ($s_x = s_y = s$). The total number of wind turbines is $n_{\text{wt}} = 1063$ for $s = 7D$ and $n_{\text{wt}} = 2088$ for $s = 5D$, resulting in a total installed wind farm capacity of 15.9 and 31.3 GW, respectively. With a total wind farm area of 3000 km², the resulting installed power density is $P''_{7D} = 5.3$ MW km⁻² and $P''_{5D} = 10.4$ MW km⁻². Note that $s = 7D$ and $P'' = 5$ MW km⁻² are typical values for currently existing wind farms in the German Bight but that even with $s = 5D$ the total installed wind farm capacity stays below the 2040 expansion target of 40 GW. Note also that, for the sake of simplicity, all existing wind turbines in the priority areas are replaced by the much larger 15 MW wind turbine.

2.4 Precursor simulations

Steady-state inflow profiles and a turbulent flow field for each main simulation are obtained by a precursor simulation with cyclic boundary conditions in both lateral directions. In order to save computational time, the precursor domains are much smaller than the main domain (see Table 1). The domain sizes are different for the different cases in order to ensure that the largest structures of each BL type are covered several times. The number of vertical grid points, the stretching and Rayleigh damping levels are the same as in the corresponding main simulation. It is important that the turbulence and the mean flow are stationary at the end of the precursor simulation. If the mean flow that is prescribed at the inflow plane is not in steady state, it will try to reach it during its passage through the main domain, causing streamwise changes in mean quantities such as wind speed and direction. While steady-state turbulence is reached after only a few hours, achieving a steady-state mean flow can take several days due to the slow decay of the inertial oscillation, which has a period of 14.6 h at a latitude of 55° N. Here, we declare the mean flow as steady if the oscillation amplitude of the hub height mean wind speed is less than 0.5 % and declare the turbulence as steady if the change in friction velocity is less than 2 % in 4 h. The physical simulation times of the precursor simulations are 96 h for the cases NBL-700-7D, NBL-700-5D and CBL-1400-7D, 48 h for the case CBL-700-7D, and 24 h for the case SBL-300-7D.

The initial velocity and potential temperature field is horizontally homogeneous. Horizontal velocity components u

and v are set to the geostrophic wind components u_g and v_g at all heights. The geostrophic wind is adjusted so that the final wind speed at hub height is 10.0 m s^{-1} , and the wind direction at hub height is parallel to the x axis (see Fig 3). The onset of turbulence is triggered by small random perturbations in the horizontal velocity field below a height of 150 m for the case SBL-300-7D and below 250 m for all other cases.

The subgrid-scale model of Dai et al. (2021) is used for the case SBL-300-7D. Test simulations with 10 and 20 m grid spacing showed that a grid spacing of 20 m is sufficient if this SGS model is used (less than 1 % difference in wind speed maximum and less than 5 % difference in BL height), whereas the results are more grid spacing sensitive (2 % difference in wind speed maximum and 20 % difference in BL height) if the standard SGS model of PALM is used. For the SBL precursor run the ratio of SGS-TKE (turbulence kinetic energy) to total TKE and SGS momentum flux to total momentum flux is smaller than 10 %, except for the lowest grid point. Further setup details vary significantly between the different cases and hence are described separately in the following sections.

2.4.1 NBL

The initial potential temperature profile of the NBL cases is linear and has a vertical temperature gradient (lapse rate) of $\Gamma = +1 \text{ K km}^{-1}$ from the surface to the domain top (see Fig. 3). At the surface, a Neumann condition for the potential temperature is applied and the surface heat flux is set to zero. Shear-driven turbulence production leads to the formation of a neutrally stratified BL that grows until it reaches a steady BL height of 780 m. The BL height is defined as the height at which the shear stress reaches 5 % of its surface value. The conventionally neutral boundary layer is separated from the FA by a capping inversion that has a stronger stratification than the FA.

2.4.2 CBL

The initial temperature profile of the CBL cases consists of a constant potential temperature between the surface and the desired BL height $h = 700$ or $h = 1400$ m for the cases CBL-700-7D and CBL-1400-7D, respectively. Above that height the potential temperature has a constant lapse rate of $\Gamma = +3.5 \text{ K km}^{-1}$, which corresponds to the International Standard Atmosphere. A Dirichlet condition is applied for the surface temperature, and a constant surface heating rate of $\dot{\theta}_0 = +0.050$ and $\dot{\theta}_0 = +0.025 \text{ K h}^{-1}$ is used to drive the CBL of the cases CBL-700-7D and CBL-1400-7D, respectively. The heating rates differ by a factor of 2 to achieve approximately the same surface heat flux Q_0 and Monin–Obukhov length L (see Table 1) so that only the effect of a changing BL height is seen in the results.

Boundary layer growth is avoided by applying a large-scale subsidence that acts only on the potential temperature

field. The subsidence velocity is zero at the surface and increases linearly to its maximum value w_{sub} at the height h and is constant above. The subsidence velocity is chosen in such a way that the temperature increase in the FA exactly matches the surface heating rate: $\dot{\theta}_0 = \Gamma w_{\text{sub}}$. Thus the BL height can be kept precisely constant even for very long precursor simulations. Final BL heights, according to the definition given in Sect. 2.4.1, are 690 and 1400 m.

Large-eddy simulations of CBLs are usually driven by a constant heat flux, i.e., a Neumann condition for the surface temperature. However, we decided to use a Dirichlet condition because of two reasons.

- It allows for spatial variations in the surface heat flux which may be caused by enhanced mixing inside the wind farms. In reality, the resulting change in sea surface temperature (on the scale of hours) would be very small due to the good turbulent mixing inside the ocean mixed layer during strong winds and due to the high heat capacity of water in contrast to that of air. Thus, it is more realistic to prescribe a horizontal homogeneous surface temperature than a horizontal homogeneous heat flux.
- Driving the CBL with a constant surface heating rate has the advantage that the temperature evolution inside the BL is known in advance, and thus the subsidence velocity required for obtaining a constant BL height is also known in advance and does not have to be found iteratively.

2.4.3 SBL

The initial potential temperature profile of the SBL case is linear and has a vertical temperature gradient (lapse rate) of $\Gamma = +3.5 \text{ K km}^{-1}$ from the surface up to the domain top. A Dirichlet condition is applied for the surface temperature because prescribing a surface heat flux can lead to unphysical results (Basu et al., 2008). Generating a steady-state SBL is not as simple as it is for the CBL. A straightforward method would be to use a surface cooling rate. However, due to the long simulation time required for the decay of the inertial oscillation, the elevated inversion at the top of the SBL would become unrealistically strong (Kosović and Curry, 2000). We developed a method to generate a steady-state SBL in which the potential temperature profile is constant in time and the strength of the elevated inversion can be freely adjusted.

The method uses the large-scale forcing functionality of PALM. Instead of changing the surface temperature, a positive temperature tendency of $+0.05 \text{ K h}^{-1}$ is added at every grid point and at every time step. This added tendency imitates a large-scale advection of warm air and thus forms an SBL with steady heat flux and momentum flux profiles. The heat flux divergence results in a cooling tendency that exactly balances the positive large-scale advection tendency so that the temperature inside the BL stays constant. In the overlying

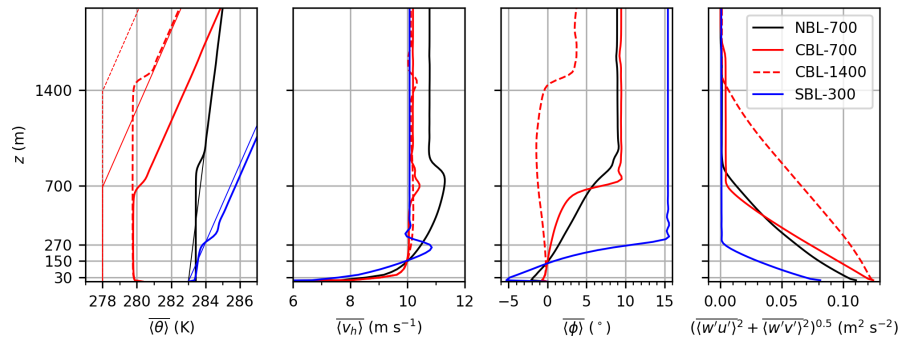


Figure 3. Vertical profiles of potential temperature (θ), horizontal wind speed (v_h), wind direction (ϕ , clockwise positive) and total (resolved + subgrid-scale) kinematic vertical momentum flux. The thin lines are initial profiles. The thick lines represent quantities that are horizontally averaged ($\langle \bullet \rangle$) over the entire precursor domain and temporal averaged ($\overline{\bullet}$) over the last hour of the precursor simulation. $\langle \theta \rangle$, $\langle v_h \rangle$ and $\langle \phi \rangle$ are used as inflow profiles for the main simulations. BL heights of 700 and 1400 m, as well as rotor top ($z = 270$ m), rotor bottom ($z = 30$ m) and hub height ($z = 150$ m), are marked on the vertical axis with horizontal grey lines.

inversion, the heat flux divergence decreases approximately linearly until it reaches zero at the transition to the FA. Consequently, the temperature in the FA increases further, and the overlying inversion becomes stronger. To prevent further strengthening of the overlying inversion, the large-scale advection tendency is set to zero in the FA at $t = 6$ h. Inside the overlying inversion, the large-scale advection tendency increases linearly to its maximum value inside the BL so that it approximately compensates for the cooling tendency caused by the heat flux divergence. From that point on the potential temperature profile is steady, and the simulation can run until the inertial oscillation has decayed. Because the potential temperature in the FA changes over time, it is excluded from the Rayleigh damping. Despite the shallow BL, a large domain height of $L_z = 3624$ m is used to capture gravity waves that are triggered by the wind farms. The final BL height, according to the definition given in Sect. 2.4.1, is 270 m.

2.5 Data analysis

Statistical data that are presented in the results section are obtained in the last 4 of the 10 h of the main simulations. Temporal averages are denoted by an overbar (e.g., $\overline{v_h}$) and horizontal averages by angled brackets (e.g., $\langle \theta \rangle$). The temporal averaged horizontal wind speed $\overline{v_h}$ is calculated as the average of the absolute values of the wind vector:

$$\overline{v_h} = \sqrt{\overline{u^2 + v^2}}. \quad (9)$$

Resolved turbulent fluxes of momentum are calculated with the eddy-correlation method. The correlation of two turbulent quantities (e.g., $u' = u - \overline{u}$ and $w' = w - \overline{w}$) can not be calculated directly during the simulation because the respective mean quantities are not known in advance. However, the resolved turbulent flux can be calculated after the simula-

tion if the correlation of the absolute quantities is calculated during the simulation:

$$\begin{aligned} \overline{w'u'} &= \overline{(w - \overline{w})(u - \overline{u})} = \overline{wu - \overline{w}u - \overline{u}w + \overline{w}\overline{u}} \\ &= \overline{wu} - \overline{w}\overline{u} - \overline{u}\overline{w} + \overline{w}\overline{u} \\ \overline{w'u'} &= \overline{wu} - \overline{w}\overline{u}. \end{aligned} \quad (10)$$

3 Results

The presentation and discussion of the results are divided into two sections: wake properties and power output. In the first section, the wake properties of very large wind farms and their effect on the BL flow is discussed. In the second section it is discussed how the power output of very large wind farms is affected by the variation in the turbine spacing and the meteorological conditions. To highlight the characteristics of very large wind farms some comparisons to small wind farms are made. However, the focus of this work lies on very large wind farms so that a systematic comparison between large and small wind farms is not conducted here but will be part of a follow-up study.

3.1 Wake properties

3.1.1 Wind speed and wind direction at hub height

The mean horizontal wind speed at hub height is shown in Fig. 4 for all cases. Streamlines indicate the wind direction.

For the NBL cases, the wind speed is reduced from 10 to 7 m s^{-1} for a turbine spacing of $s = 7D$ and 5 m s^{-1} for $s = 5D$ inside the large wind farms in Zone 3. The wake length is defined as the distance between the wind farm trailing edge and the point at which the wind speed recovers to 90% of its initial value, i.e., 9 m s^{-1} . For the small wind farms N-1, N-2 and N-3 (see Fig. 1), the wake length ranges from 1 to 20 km.

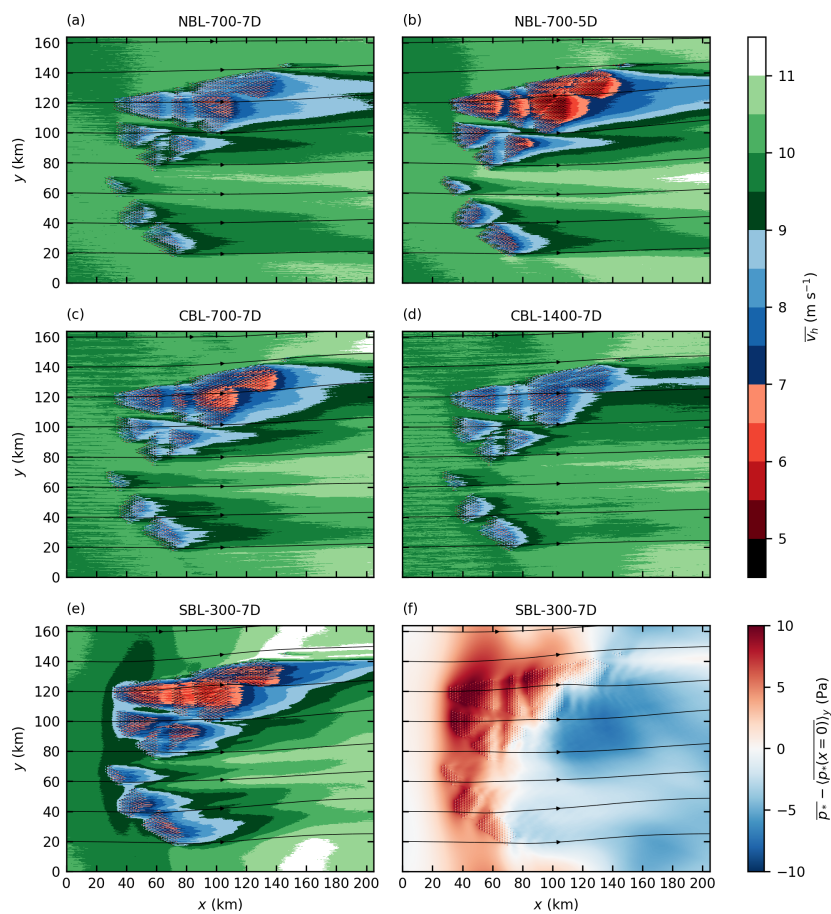


Figure 4. Mean horizontal wind speed \bar{v}_h at hub height for all five cases (a–e) and perturbation pressure p_* at hub height relative to its value at the inflow for the case SBL-300-7D (f). Streamlines indicate the wind direction.

However, the wake length of the large wind farms in Zone 3 is approximately 100 km for $s = 7D$, and the wake extends beyond the model domain for $s = 5D$.

The wake flow is deflected counterclockwise. The largest deflection angle of approximately 10° is observed for the smaller turbine spacing ($s = 5D$). The counterclockwise wake deflection is consistent with the findings of Allaerts and Meyers (2016), who observed a counterclockwise deflection of $2\text{--}3^\circ$ for a 15 km long wind farm. A counterclockwise wind direction change (higher ageostrophic wind component) has also been observed by Abkar and Porté-Agel (2014) and Johnstone and Coleman (2012), who investigated infinitely large wind farms. The wake deflection is caused by a reduced Coriolis force, as is shown in the next section. Because the Coriolis force is proportional to the wind speed, the deflection angle is higher for the case with the greater speed deficit (NBL-700-5D). The reasons for the slow speed recovery and the wake deflection are discussed in detail in the next section.

The inflow wind speed has slight variations in the crosswise direction which are caused by the wind-farm-induced flow deceleration reaching the recycling plane (see Sect. 2.3). The variations have an amplitude of approximately 0.1 m s^{-1} , which is 1% of the inflow wind speed.

For the CBL cases, the wind speed is reduced to 6.5 m s^{-1} for $h = 700 \text{ m}$ and 8 m s^{-1} for $h = 1400 \text{ m}$ inside the large wind farms in Zone 3. Also, the wake length of the large wind farms is much longer for the shallow BL than for the thick BL. This BL height dependency occurs because the turbulent vertical kinetic energy flux is greater for the case with the thicker BL (see Fig. 11c and d). The wind speed deficit and the wake length of small wind farms (e.g., N-1, N-2 and N-3) are relatively unaffected by the BL height because the wind-farm-induced internal BL does not reach the inversion layer (NBL cases) or only reaches it several tens of kilometers downstream of the wind farm trailing edge (CBL cases) (see Fig. 8). Consequently, the BL height only affects further wind speed recovery (e.g., to 9.5 m s^{-1}) in the far wake

of small wind farms. For example, the wind speed recovery from 9 to 9.5 m s^{-1} in the wake of N-2 takes longer for the case CBL-700-7D (40 km) than for the case CBL-1400-7D (15 km) (see Fig. 4c and d).

The wake is deflected counterclockwise in the CBL cases, as well. The deflection angle is approximately 5° for the case with the shallow BL and $1\text{--}2^\circ$ for the case with the thick BL. The higher deflection angle for the case with the shallow BL is caused by a greater speed deficit compared to the case with the thick BL.

A comparison between the cases NBL-700-7D and CBL-700-7D shows that the speed deficit inside Zone 3 is greater for the CBL case. Also, the wakes of the small wind farms are longer for the CBL case. This is contradictory to the well-known fact that wind turbine and wind farm wakes are generally shorter in CBLs than in NBLs and SBLs (Porté-Agel et al., 2020, their Sects. 2.3 and 3.4.2). To achieve the same hub height wind speed for both cases, the geostrophic wind speed is 6 % greater for the NBL case (see Table 1) than for the case CBL-700-7D. Additionally, the wind speed is super-geostrophic in the upper half of the NBL, and thus the mean BL wind speed is approximately 10 % greater in the NBL case than in the CBL case. Stability likely has little-to-no effect because the stratification of the CBL case is only weakly unstable ($L = -420 \text{ m}$; see Table 1).

In the stable case SBL-300-7D, the wind speed is reduced to below 7 m s^{-1} in the first 20 km of the large wind farms in Zone 3. The wind speed deficit is greater, and the wake is more than 20 km longer for the small wind farms compared to the other cases with $s = 7 \text{ D}$. The wake of the large wind farms in Zone 3, however, is not longer than in the cases NBL-700-7D and CBL-700-7D. This occurs because the speed recovery in the wake of this large wind farm is not driven by momentum flux divergence (which is stability dependent) but rather by a favorable pressure gradient (details are given in the next section). The case SBL-300-7D covers several flow features that are not as significant in the other cases. These features are namely flow blockage in front of the wind farms, flow deflection around the wind farms and flow acceleration beside the wind farms and/or wakes. These features are related to the pressure field inside and around the wind farms. The perturbation pressure $\overline{p^*}$, relative to its value at the inflow, is shown in Fig. 4f. A high-pressure region in the upstream part of the large wind farms in Zone 3 leads to an adverse pressure gradient and thus flow deceleration in front of the wind farms. This effect is known as blockage effect or flow blockage (Wu and Porté-Agel, 2017). At a distance of 2.5 D upstream of the first wind turbine row of the wind farms in Zone 3, the wind speed is reduced by approximately 10 % relative to the inflow wind speed. For all other cases the speed reduction is approximately 2 %. Wu and Porté-Agel (2017) reported 11 % speed reduction 2.5 D upstream of the first turbine row of a 20 km long wind farm in a CNBL with a FA stratification of $\Gamma = +5 \text{ K km}^{-1}$. However, for $\Gamma = +1 \text{ K km}^{-1}$ they reported a speed reduction of

only 1.2 % because the flow is supercritical (Froude number, $Fr > 1$). Using the same definition² as in Wu and Porté-Agel (2017), the Froude number in the case SBL-300-7D is $Fr = 1.47$, indicating a supercritical flow. This should, according to the reasoning of Wu and Porté-Agel (2017), result in a weak flow blockage, which does not correspond to the significant flow blockage observed in the case SBL-300-7D. The only case that is subcritical (and should thus show significant flow blockage) is CBL-1400-7D ($Fr = 0.81$), but in this case the flow blockage is only very weak. Hence, for the cases that are investigated in this study, the Froude number, as defined by Wu and Porté-Agel (2017), is not an appropriate parameter for predicting flow blockage.

In the downstream part of the large wind farms, a favorable pressure gradient tends to accelerate the flow, counteracting the wind-turbine-induced flow deceleration. Consequently, the wind speed does not decrease further but remains nearly constant at approximately 6 m s^{-1} . In the wake, the pressure is more than 5 Pa smaller than the undisturbed pressure upstream of the wind farms. This results in a relatively fast speed recovery in the wake and in wind speeds well above the inflow wind speed beside the wakes. Note that this effect might be overestimated because the wind farms block a relatively large fraction of the domain width. The pressure perturbations are induced by large-scale gravity waves that are triggered by the wind farms. The observed pressure distribution in the streamwise direction is consistent with the findings of Allaerts and Meyers (2017) and Wu and Porté-Agel (2017), who investigated semi-infinite wind farms in CNBLs. The effect can only be seen in the case SBL-300-7D because it is most extreme if the BL height approaches the total height of the wind turbines. More details about wind-farm-induced gravity waves are provided in Sect. 3.1.4.

Because the wind farms in this study have a finite size also in the crosswise direction, it can be seen that the pressure perturbation also significantly affects the wind direction. Due to the streamwise reduction in wind speed, the flow diverges in the crosswise direction inside the wind farms. In the wake, where the flow accelerates, horizontal convergence can be observed.

3.1.2 Reasons for wake deflection and slow speed recovery

What is the reason for the slow speed recovery and the wake deflection inside and behind the large wind farms? In order to answer that question, Fig. 5 shows streamwise (parallel to streamlines) and crosswise (perpendicular to streamlines) components of the pressure gradient force³, the Coriolis force F_c and the resolved vertical turbulent momentum

²For details about the calculation of the Froude number refer to Wu and Porté-Agel (2017) and Vosper et al. (2009).

³The pressure gradient force and the Coriolis force are not considered explicitly in the model but are considered implicitly by the geostrophic wind.

flux divergence, also called frictional force F_f , at $z = 150$ m and $y = 120$ km. The pressure gradient force can be divided into the geostrophic pressure gradient force F_{gp} , which is constant and is defined by the geostrophic wind, and the perturbation pressure gradient force F_{pp} , which can vary horizontally due to wind-farm-induced pressure perturbations. The forces are averaged over 1 turbine spacing along x and y in order to eliminate peaks in F_{pp} that are caused by single turbines. Thrust forces of the turbines are not included. The analysis is made from a Lagrangian frame of reference, examining the forces on an air parcel during its passage through the wind farms. From an Eulerian frame of reference, the sum of all forces, including the advection tendencies, would sum to zero because the flow is stationary.

Streamwise force components in Fig. 5a show that the accelerating geostrophic pressure gradient force and the decelerating momentum flux divergence are in balance and sum to zero at the inflow. The streamwise component of the Coriolis force is zero because this force acts always perpendicular to the flow. Inside the wind farms, the momentum flux divergence is positive and thus is an accelerating component. It is the dominant driving force because it is more than 7 times greater than the geostrophic pressure gradient force.

An increasing perturbation pressure in front of the wind farm leads to a negative perturbation pressure gradient force and thus flow deceleration (often called blockage effect). However, inside the wind farms the perturbation pressure gradient force is positive due to a favorable pressure gradient (decreasing pressure). In the near wake the momentum flux divergence is high and leads to a fast speed recovery. The momentum flux divergence decreases fast until it becomes negative in the far wake so that the speed recovers slowly in the far wake. The only force that remains for driving the flow is the geostrophic pressure gradient force. At the inflow, this force is in balance with the momentum flux divergence, but in the wake this is not the case due to two reasons: first, the negative momentum flux divergence is weaker than at the inflow due to a lower wind speed and thus a reduced near-surface momentum flux; second, the streamwise component of the geostrophic pressure gradient force has increased by 80 % because the wake flow is deflected counterclockwise (i.e., to lower pressure). These results show that the wake deflection is an elementary feature of the wake that supports the wind speed recovery. They also show that mixing of momentum from the BL to the wind turbine level is not the dominant process that drives the speed recovery in the far wake of very large wind farms.

The wake deflection can be explained by examining the crosswise force components that are shown in Fig. 5b. Positive forces result in counterclockwise flow deflection, and negative forces result in clockwise flow deflection. At the inflow, the Coriolis force, the geostrophic pressure gradient force and the momentum flux divergence are in balance. Because the Coriolis force is proportional to the wind speed, it is reduced by approximately 30 % inside the wind farms and

the wake. Consequently, the sum of all forces becomes positive and the flow is deflected counterclockwise. The momentum flux divergence and the perturbation pressure gradient force are negative inside the wind farm and inside the wake and are therefore opposing the wake deflection. The negative perturbation pressure gradient force is a result of the pressure distribution around the wind farms that is caused by the wind farm shape (see Fig. 4d).

The reason for the negative momentum flux divergence is the enhanced downward mixing of negative y momentum of the overlying flow, which veers to the right (see Fig. 3). For small wind farms this process can be dominant and may result in clockwise wake deflection (Van Der Laan and Nørmark Sørensen, 2017). However, for very large wind farms, as in this study, the effect of the reduced Coriolis force is dominant. An appropriate parameter for estimating the importance of Coriolis effects is the Rossby number. Coriolis effects become dominant for Rossby numbers close to or below 1. For the large wind farms in Zone 3 with a length of $L_{wf} \approx 100$ km at mid-latitudes (Coriolis parameter $f \approx 10^{-4}$) and a wind speed of $U \approx 10$ m s $^{-1}$, the Rossby number becomes

$$Ro = \frac{U}{L_{wf} f} \approx 1, \quad (11)$$

indicating that Coriolis effects play an important role for flows in wind farms of this size.

3.1.3 Turbulence intensity at hub height

The turbulence intensity TI is defined as in Porté-Agel et al. (2013):

$$TI = \frac{\sqrt{\frac{2}{3} \text{TKE}}}{v_h}, \quad (12)$$

where TKE is the resolved turbulence kinetic energy defined as follows:

$$\text{TKE} = \frac{1}{2} (\overline{u'^2} + \overline{v'^2} + \overline{w'^2}), \quad (13)$$

where $\overline{u'^2}$, $\overline{v'^2}$ and $\overline{w'^2}$ are the resolved-scale variances of u , v and w , respectively. The SGS-TKE is neglected because it is smaller than 10 % of the resolved TKE inside the wind turbine wakes at a distance of 3D or more.

The TI at hub height is shown in Fig. 6. Inside the wind farms, the TI reaches a fully developed state after approximately four rows and is constant farther downstream. A smaller turbine spacing leads to a greater TI inside the wind farms. For the case NBL-700-7D, a TI of 10 % is reached inside the wind farms, but more than 14 % is reached in the case NBL-700-5D. In the CBL cases, the TI inside the wind farms reaches 10 % in case CBL-700-7D and approximately 12 % in CBL-1400-7D. Although the ambient TI is only approximately 3 % for the case SBL-300-7D, the TI inside the

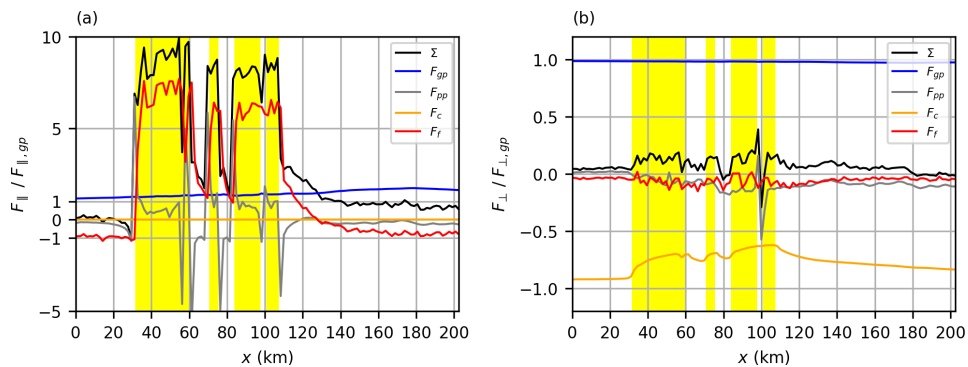


Figure 5. Streamwise and crosswise force components F_{\parallel} (a) and F_{\perp} (b) along a line at $y = 120$ km and $z = 150$ m for the case NBL-700-7D. Shown are the geostrophic pressure gradient force (F_{gp}), the perturbation pressure gradient force (F_{pp}), the Coriolis force (F_c), the frictional force (F_f , momentum flux divergence) and the sum of all forces (Σ). The forces are normalized by the respective geostrophic pressure gradient force component at the inflow and are horizontally averaged over one turbine spacing along x and y . The position of the wind farms is marked by yellow areas.

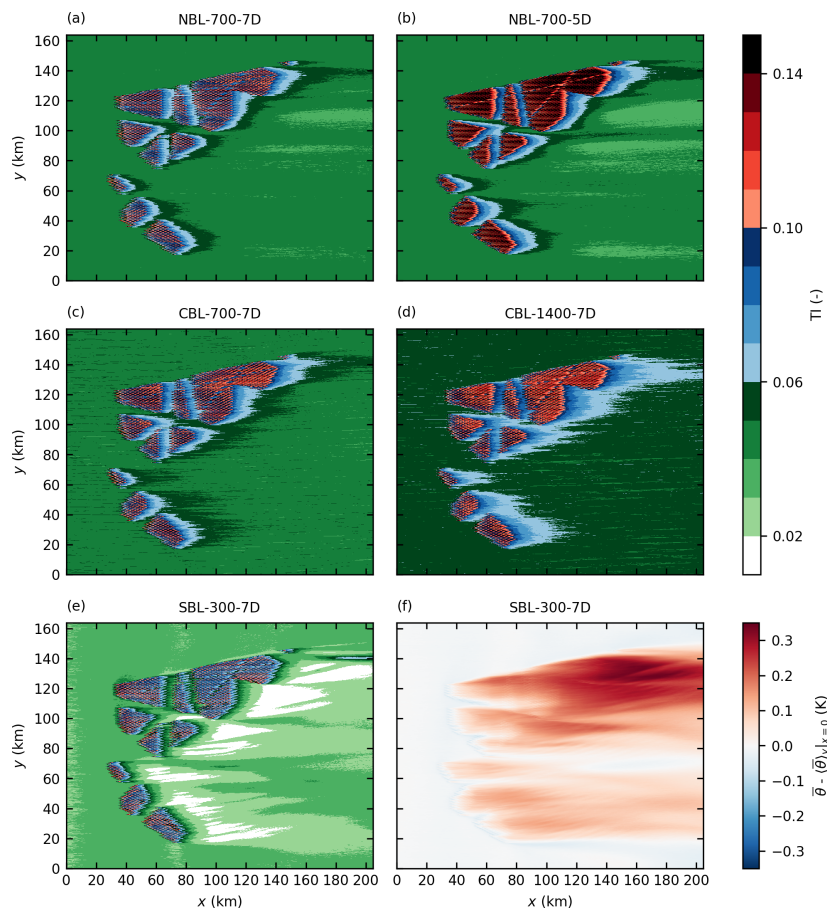


Figure 6. Turbulence intensity (TI) at hub height for all five cases (a–e) and potential temperature at hub height relative to the inflow temperature for the case SBL-300-7D (f).

wind farms reaches values similar to NBL-700-7D (approximately 10 %).

The wake in terms of TI is generally shorter than the wake in terms of wind speed (see Fig. 4). The shortest wakes occur in the shallow SBL (SBL-300-7D), and the longest wakes occur in the thick CBL (CBL-1400-7D). This is the opposite behavior than that of the wake in terms of wind speed. The wake length in terms of TI weakly depends on wind farm size with slightly longer wakes for larger wind farms. However, this effect is caused by the definition of the TI, in which the wind speed variances are normalized by the mean horizontal wind speed. The mean horizontal wind speed is smaller in the wake of the large wind farms than in the wake of the small wind farms, resulting in a higher TI in the wake of the large wind farms. The wind farm size dependency of the wake length vanishes if the TKE is used for measuring the wake length instead of the TI (not shown).

In the NBL cases and especially in the SBL case, the TI in the far wake drops below the ambient TI at the inflow. This effect is caused by the reduced wind speed in the far wake which leads to a reduction in the shear-driven turbulence production. In the CBL cases, there is also buoyancy-driven turbulence production, which is unaffected by the reduced wind speed in the wake and thus maintains the TI level. That buoyancy-driven turbulence production has a large impact on hub height TI is also verified by the fact that the ambient TI is greater in the CBL case with the thick BL (CBL-1400-7D) than in the case with the shallow BL (CBL-700-7D): the convective velocity scale $w^* = (\frac{g z_i}{\theta} (w'\theta')_0)^{1/3}$ is greater in the case CBL-1400-7D than in the case CBL-700-7D, and hence also the buoyancy-generated velocity variances are greater. Because buoyancy acts as a TKE sink in the SBL case, it can not compensate for the reduction in shear-driven turbulence production, and thus the TI in the wake drops below 2 %. This effect is amplified by the entrainment of warm air into the BL that leads to a stabilization (increased lapse rate) at hub height and therefore stronger turbulence damping (see Figs. 6f and 9). The entrainment of warm air results in a temperature increase at hub height of approximately 0.3 K for the large wind farms and approximately 0.1 K for the small wind farms.

3.1.4 Boundary layer development

Figure 7 shows vertical cross sections of the horizontal mean wind speed for all cases. The cross sections are located at $y = 120$ km and thus cross the large wind farms in Zone 3. The inversion layer height z_i is marked by lines at which the maximum vertical potential temperature gradient occurs. The wind-farm-induced internal boundary layer (IBL) is shown by a line at which the horizontal wind speed corresponds to 97 % of the inflow wind speed at that height.

The IBL is not shown for the case SBL-300-7D because the wind turbines are nearly as high as the BL. For all other cases the IBL grows up to the inversion layer (IL) within

40 km (NBL-700-7D and NBL-700-5D), 10 km (CBL-700-7D) and 20 km (CBL-1400-7D) behind the wind farm leading edge. The streamwise extent of the IBL goes beyond the model domain, indicating that the wind speed inside the entire BL does not recover to 97 % of the inflow wind speed.

The IL height is affected by the presence of the wind farms in all five cases. In the NBL cases the IL is displaced upwards by 200–300 m, whereas a larger displacement occurs for the smaller turbine spacing. The IL displacement is a result of the reduced wind speed in the bulk of the BL: to obtain a divergence-free flow inside the BL, the wind speed reduction (streamwise convergence) is compensated for by vertical divergence (IL displacement) and crosswise divergence (flow around the wind farms). The increase in IL height is not caused by entrainment of warm air into the BL (as can also be seen in the profiles of potential temperature in Fig. 9). This phenomenon has also been observed by Allaerts and Meyers (2017), who also stated that the mass flux conservation is the reason for the IL displacement. Abkar and Porté-Agel (2014) stated that a smaller turbine spacing results in a larger BL height for an infinite wind farm in a CNBL. The IL displacement causes an acceleration of the flow in the FA for the NBL and CBL cases. Details about this effect are described in the next section.

In the CBL cases, the IL height increases above the wind farms and decreases above the wake, reaching its initial value at approximately 70 km downstream of the last wind farm trailing edge. The IL displacement is larger for the shallower BL, i.e., the case CBL-700-7D.

The IL displacement is most significant for the case SBL-300-7D. The IL height increases from 300 to 500 m. Allaerts and Meyers (2016) also reported that larger IL displacements occur for shallower BLs (+60 % for $h = 250$ m). In the case SBL-300-7D, the IL height increase is caused by vertical displacement due to mass conservation and also by entrainment of warm air into the BL (see Fig. 7f). The entrainment of warm air into the BL leads to a warming of the lower part of the BL. However, the temperature at the height of the original IL is reduced because the warm air in the IL is replaced by relatively cold air from the BL.

Because the laminar flow in the FA is adiabatic, the isotherms in Fig. 7f can be interpreted as streamlines. They show that gravity waves are excited by the wind farms. There are small-scale gravity waves with a wavelength that corresponds to the turbine spacing and a large-scale gravity wave with a wavelength that approximately corresponds to the wind farm length. The negative and positive temperature deviations in the wave crest and trough, respectively, cause a positive and negative deviation in the perturbation pressure at the surface, as is shown in Fig. 4f. A detailed analysis of the wind-farm-induced gravity waves goes beyond the scope of this study. However, it is noted that the qualitative pressure and temperature distributions correspond to the findings of Allaerts and Meyers (2017) and Wu and Porté-Agel (2017).

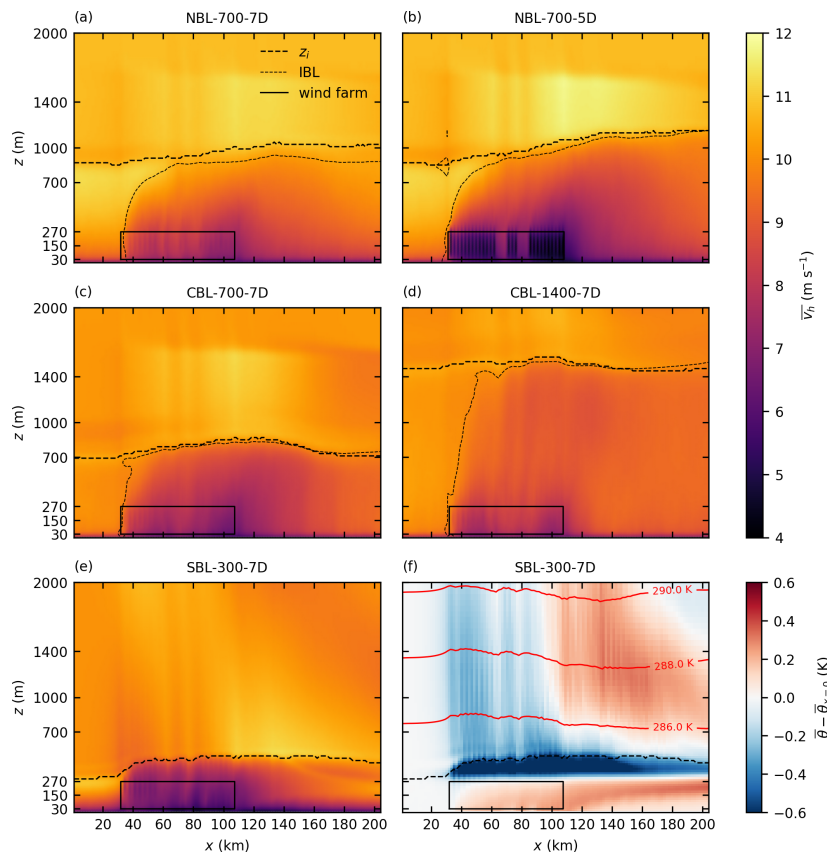


Figure 7. Vertical cross sections at $y = 120$ km of wind speed v_h for all cases (a–e) and potential temperature deviation relative to the inflow temperature for the case SBL-300-7D (f). Also shown are the inversion layer height z_i (maximum vertical temperature gradient), the internal boundary layer IBL (97 % of inflow wind speed) and the extent of the wind farms in Zone 3.

Additional test simulations have shown that the strength of the gravity waves is sensitive to the domain height. Allaerts and Meyers (2017) achieved good results (low wave reflection at the domain top) if the domain height corresponds to at least one vertical wavelength $\lambda_z = 2\pi U/N$, where U is the BL bulk wind speed, and N is the Brunt–Väisälä frequency in the FA. In the case SBL-300-7D, the domain height is set to $0.43\lambda_z$ ($\lambda_z = 5.9$ km, $L_z = 3624$ m) because larger domain heights lead to numerical instabilities at the inflow. Wu and Porté-Agel (2017) used a domain height of $L_z = 2.4$ km for a FA stratifications of $\Gamma = 1$ K km⁻¹ (resulting in $L_z = 0.22\lambda_z$) and $\Gamma = 5$ K km⁻¹ (resulting in $L_z = 0.49\lambda_z$). It is not clear whether the vertical wavelength is the only relevant parameter for choosing the correct domain height or whether the wind farm length also has to be considered. Further research is needed to find setup guidelines that ensure that wind-farm-induced gravity waves are covered as realistically as possible.

In order to compare the effects of small and large wind farms on the boundary layer, Fig. 8 shows vertical cross sec-

tions at $y = 50$ km, crossing the small wind farm N-2. The IL displacement is much smaller compared to the displacement triggered by the large wind farms (i.e., 50–100 m for the small wind farm in contrast to 200–300 m for the large wind farms). For the NBL cases the IBL grows to approximately 700 m and thus does not reach the IL. For the case CBL-700-7D the IBL reaches the IL but only 40 km behind the wind farm trailing edge. The streamwise extent of the IBL shows that the wind speed recovery at hub height to 97 % of the inflow wind speed is reached 20 km (NBL-700-7D and CBL-1400-7D) and approx. 50 km (NBL-700-5D and CBL-700-7D) behind the wind farm trailing edge. For all 7D cases, the IBL does not start at the wind farm leading edge but rather inside the wind farms. The reason for this effect is that the vertical cross section does not cross the rotor discs of the turbines, and no averaging occurs in the y direction. As Fig. 8f shows, the small wind farms also triggers gravity waves in the FA, but they are much weaker than the ones triggered by the large wind farms.

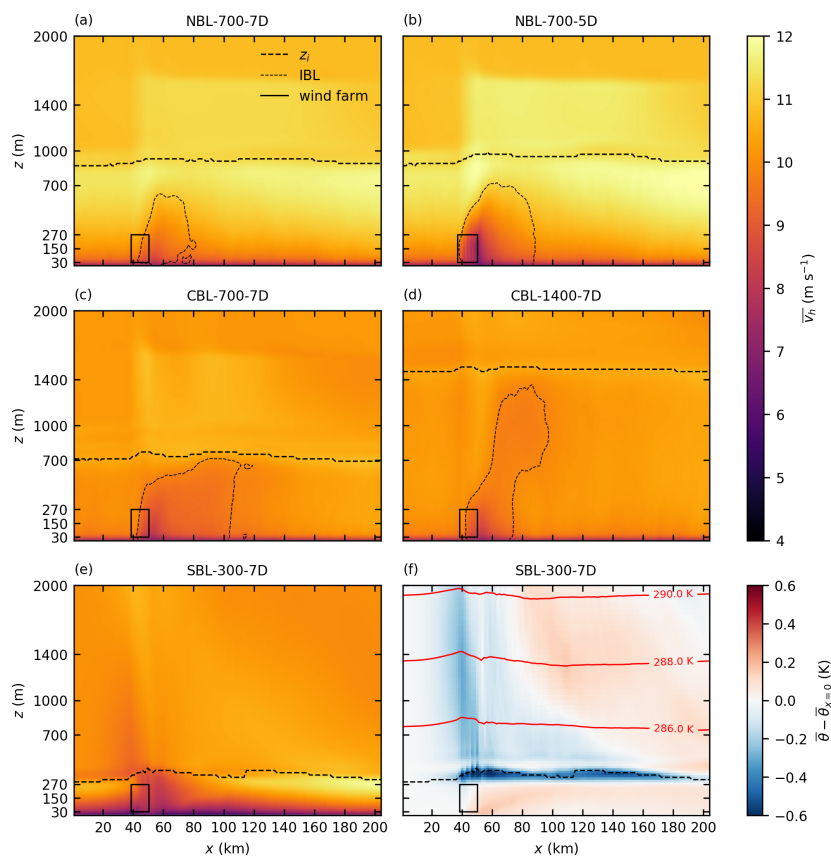


Figure 8. Vertical cross sections at $y = 50$ km of wind speed v_h for all cases (a–e) and potential temperature deviation relative to the inflow temperature for the case SBL-300-7D (f). Also shown are the inversion layer height z_i (maximum vertical temperature gradient), the internal boundary layer IBL (97 % of inflow wind speed) and the extent of the wind farm N-2.

3.1.5 Profiles of wind speed, wind direction and potential temperature in the wake

To examine the effect of the wind farms on the BL in more detail, profiles of wind speed, wind direction and potential temperature are shown in Fig. 9. The profiles are evaluated at the inflow ($x = 0$ km), in the near wake ($x = 120$ km) and in the far wake ($x = 180$ km) of the large wind farms in Zone 3 ($y = 120$ km).

The wind speed profiles show that the wind-farm-induced wind speed deficit spreads over the entire height of the BL. The effective vertical mixing in the CBL cases results in an approximately height-constant wind speed at the inflow and in the wake. In the case CBL-1400-7D, the wind speed in the upper part of the BL is even lower than in the lower part of the BL at $x = 120$ km. In the NBL cases, the vertical mixing is not as effective, and thus a significant wind shear exists over the entire BL in the wake. The wind speed profiles of the case SBL-300-7D show that the BL has grown from 300 to 500 m and that the super-geostrophic maximum is elimi-

nated completely. The IL displacement causes an increase in wind speed in the FA above the BL. The maximum increases (approximately 1 m s^{-1}) are observed for the cases with the greatest IL displacements. That suggests that the wind speed excess above the BL is also caused by the continuity constraint; i.e., the wind speed has to increase in order to maintain a constant mass flux between the IL and the domain top. For the CBL cases, in which the IL height decreases again behind the wind farms, the wind speed above the BL decreases to below-geostrophic in the far wake ($x = 180$ km). Note that these effects could be overestimated because of the artificial boundary that is introduced by the Rayleigh damping layer that starts several hundred meters above the BL. The sensitivity of this effect on the Rayleigh damping height has not been investigated because the scope of this study is on BL-internal effects.

The wake deflection shown in the horizontal cross sections can also be seen in the wind direction profiles. The wind-farm-induced wind direction change is approximately constant over the entire height of the BL. The largest deflec-

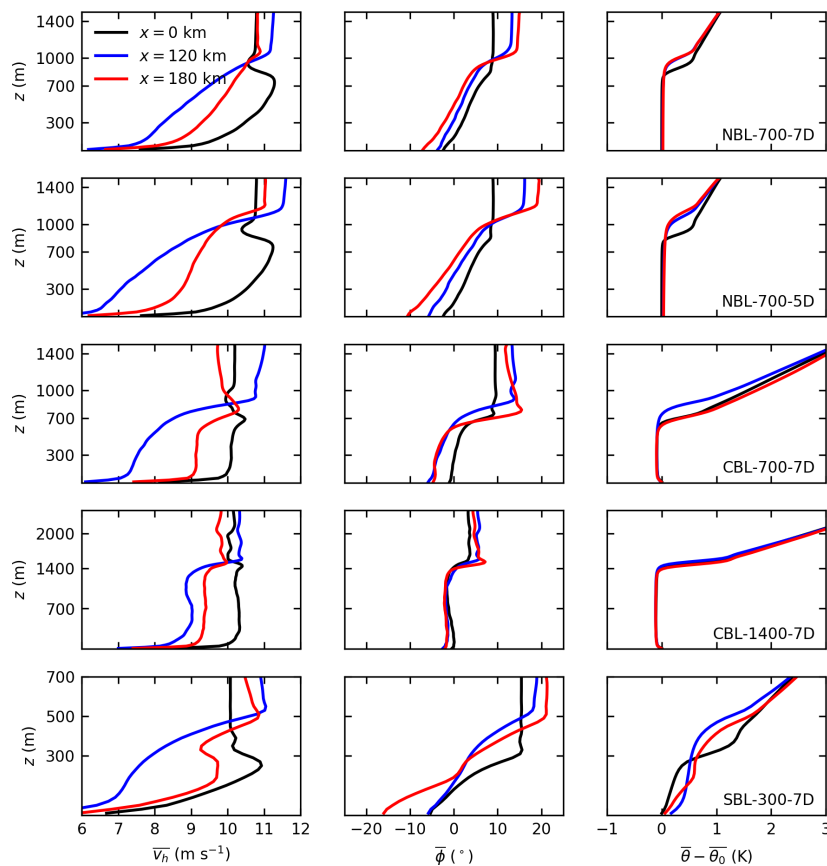


Figure 9. Vertical profiles of temporal averaged horizontal wind speed ($\overline{v_h}$), wind direction ($\overline{\phi}$, clockwise positive) and potential temperature ($\overline{\theta}$) relative to surface temperature $\overline{\theta}_0$ at the inflow ($x = 0$ km), in the near wake ($x = 120$ km) and in the far wake ($x = 180$ km) of the large wind farms in Zone 3 ($y = 120$ km) for all five cases. The wind farm trailing edge is located at $x = 108$ km.

tion angles of up to -10° are observed for the cases with the greatest speed deficit (SBL-300-7D and NBL-700-5D) because the Coriolis force reduction is greatest in these cases. The smallest deflection angle is observed in the case CBL-1400-7D with no deflection in the upper half of the BL. All cases have in common that, in contrast to the counterclockwise deflection in the BL, the flow in the FA is deflected *clockwise*. As a result, the wind veer in the inversion layer increases to approximately 10° . The flow deflection in the FA is also a Coriolis effect. Because the wind speed in the FA is supergeostrophic, the Coriolis force is greater than the geostrophic pressure gradient force, and therefore the flow is deflected clockwise. The largest deflection angle of more than 10° is observed for the case NBL-700-5D. Note that the highest wind speed excess occurs at $x = 120$ km, but the highest deflection angle occurs at $x = 180$ km. This effect can be interpreted as an inertia oscillation in space (along x), with the deflection angle being phase shifted 90° relative to the wind speed excess. Note that this effect might also

be overestimated due to the potentially overestimated wind speed excess. However, currently running investigations with much higher Rayleigh damping heights show the same behavior. In the case SBL-300-7D, the combination of clockwise deflection in the FA and counterclockwise deflection in the BL results in a total wind veer of approximately 40° between the surface and the FA.

The effect of the wind farms on the potential temperature profiles is largest for shallow BLs (SBL-300-7D) and negligibly small for thick BLs (CBL-1400-7D). The potential temperature profiles inside the well-mixed BLs of the NBL and CBL cases are nearly unaffected by the wind farms. The greatest changes take place in the inversion layer, which is displaced upwards in order to maintain a constant mass flux in the BL, as already described in the previous section. The profiles show that the potential temperature inside the BL is unchanged, and thus BL warming due to entrainment of warm air from the FA is *not* the reason for the increased IL height. On the contrary, the temperature at the height of the

original IL decreases by approximately 0.5 K because it is replaced by colder air from the underlying BL. The potential temperature profile of the SBL case is heavily modified by the wind farms. The temperature in the BL increases by approximately 0.5 K due to entrainment of warm air from the FA into the BL. The IL rises from 300 to 500 m due to the combined effect of BL warming and IL displacement. Because the surface temperature is constant, a new SBL forms in the far wake. This new SBL is shallower and more stably stratified than the original SBL at the inflow.

3.2 Power output

3.2.1 Wind turbine and wind farm efficiencies

The effect of different turbine spacings, BL heights and stabilities on the power output of very large wind farms is investigated here. This is done by comparing wind farm efficiencies of small and large wind farms for the five simulated cases. Here, the turbines in the area N-1 are defined as a small wind farm because this area has the size of a typical, currently existing wind farm in the German Bight. The turbines in Zone 3 are defined as a large wind farm because this area will be equipped with wind farms in the future (see Fig. 10f). The small wind farm consists of 27 wind turbines for $s = 7$ D and 54 wind turbines for $s = 5$ D, resulting in an installed wind farm capacity of 0.405 GW for $s = 7$ D and 0.810 GW for $s = 5$ D. The large wind farm consists of 636 wind turbines for $s = 7$ D and 1260 wind turbines for $s = 5$ D, resulting in an installed wind farm capacity of 9.54 GW for $s = 7$ D and 18.90 GW for $s = 5$ D.

The wind farm efficiency η_{wf} is defined as the total wind farm power P_{wf} normalized by the wind farm power that would be achieved if all wind turbines n_{wt} were operating in free-stream conditions, generating the reference power P_{ref} (all quantities are averaged over the last 4 h of the simulation):

$$\eta_{wf} = \frac{P_{wf}}{n_{wt}P_{ref}}. \quad (14)$$

For each of the five cases the reference power is obtained by an additional simulation of a single turbine using the same inflow profiles as for the respective main simulation. The reference powers for each case are given in Table 2. The wind farm efficiency can also be interpreted as the wind turbine efficiency averaged over all wind turbines of the wind farm. The wind turbine efficiency of a wind turbine generating P_{wt} is defined as follows:

$$\eta_{wt} = \frac{P_{wt}}{P_{ref}}. \quad (15)$$

The wind farm efficiencies of the small and the large wind farm are listed in Table 2, and the wind turbine efficiencies are shown in Fig. 10.

In general, the wind farm efficiency is significantly lower for large wind farms than for small wind farms. All 7D cases,

Table 2. Reference power of a single turbine in free-stream conditions and wind farm efficiencies for a small wind farm (N-1) and a large wind farm (Zone 3) for all five cases.

Case	P_{ref}	Wind farm efficiency	
		N-1	Zone 3
NBL-700-7D	12.56 MW	0.87	0.58
NBL-700-5D	12.56 MW	0.77	0.41
CBL-700-7D	12.51 MW	0.86	0.54
CBL-1400-7D	12.53 MW	0.88	0.64
SBL-300-7D	11.45 MW	0.66	0.46

except for the SBL case, show efficiencies of 0.86–0.88 for the small wind farm and efficiencies of 0.54–0.64 for the large wind farm. In the SBL case, the efficiency of the small wind farm is 0.66 because the wind farm is affected by the blockage effect of the sum of all wind farms. This is visible in Fig 10e, which shows that the efficiency of the wind turbines in the first row of N-1 is already below 0.8. The efficiency of the large wind farm is 30 % lower than that of the small wind farm for the SBL case. The blockage effect redistributes energy from upstream parts of the wind farm to downstream parts of the wind farm by a favorable pressure gradient, which has already been shown by Allaerts and Meyers (2017) for wind farms in shallow CNBLs. This effect can also be seen in the power distribution inside the farm: the turbine power is constant from approximately row 10 up to the trailing edge of the large wind farm in Zone 3 (see Figs. 10e and 11e). In all other cases the wind turbine power does not reach a steady state until the end of the wind farms.

A reduction of turbine spacing from $s = 7$ D to $s = 5$ D results in an efficiency reduction of 12 % (0.87 to 0.77) for the small wind farm but results in an efficiency reduction of 29 % (0.58 to 0.41) for the large wind farm. The low wind farm efficiency for the case NBL-700-5D can be explained by a fast drop in the turbine efficiencies to values below 0.4 only 20 km downstream of the leading edge. The low wind turbine efficiencies are caused by a reduction in the vertical kinetic energy flux, as shown in the next section.

A doubling of the BL height results in an efficiency increase of +2 % (from 0.86 to 0.88) for the small wind farm but in an efficiency increase of 19 % (from 0.54 to 0.64) for the large wind farm. The dependency of wind farm efficiency on the BL height has also been observed by Allaerts and Meyers (2016), who reported a 17.6 % increase in power deficit for a BL height reduction from 1000 to 250 m.

A comparison between the cases NBL-700-7D and CBL-700-7D shows that greater wind farm efficiencies are obtained for the NBL, although better efficiencies are expected for the CBL due to the better vertical mixing. Comparing the wind speed profiles of these cases (see Fig. 3) shows that the inflow wind speed in the bulk of the BL is higher for the NBL than for the CBL, which is probably the reason for the higher

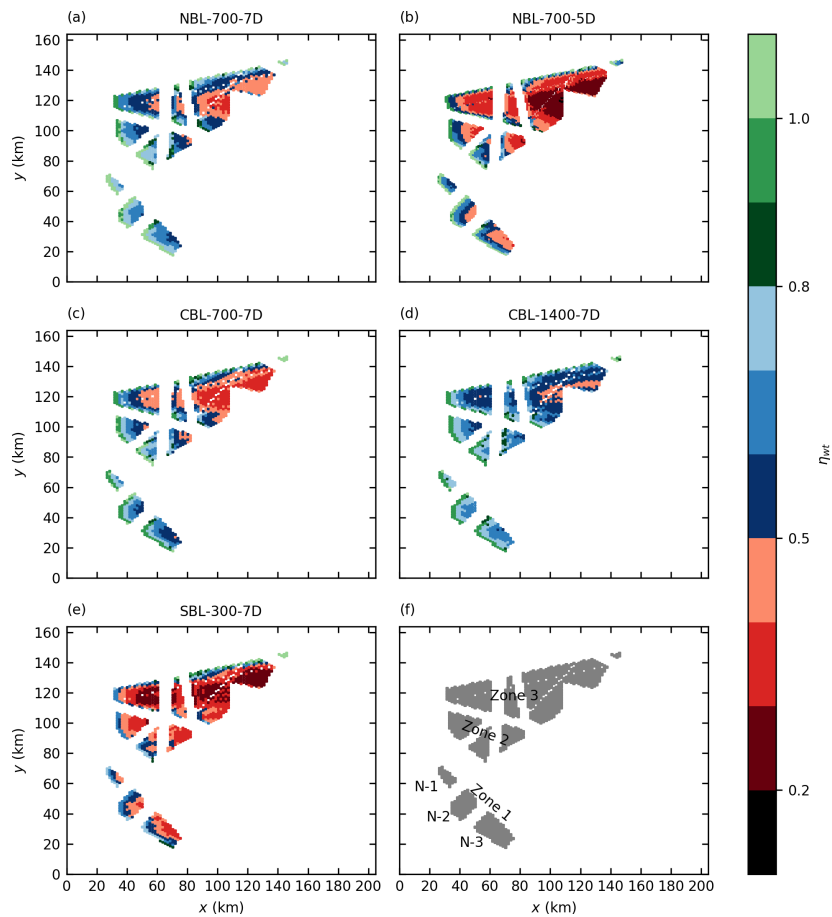


Figure 10. Wind turbine efficiencies η_{wt} for all five cases (a–e) and overview of wind farm names (f).

wind farm efficiencies. This result shows that it is important to consider not only the wind speed at hub height but also the wind profile inside the entire BL to make accurate wind farm performance predictions.

3.2.2 Energy source analysis

To examine the dependency of the wind farm efficiency on the turbine spacing and the BL height in more detail, an energy source analysis is made in this section. Here, an energy source is defined as an energy input to the flow, i.e., a process that drives the wake recovery. This can be one of the following:

1. vertical turbulent flux of kinetic energy at rotor top level, W_{vkef} ;
2. work done by the geostrophic pressure gradient on the flow below rotor top level (bottom of the BL), $W_{pgg,wt}$;

3. work done by the perturbation pressure gradient on the flow below rotor top level, $W_{ppg,wt}$.

The analysis is a simplified version of the analyses made by Abkar and Porté-Agel (2014) and Allaerts and Meyers (2017) and does not claim to be a complete energy budget analysis. The intention of this analysis is to show which processes dominate the wake recovery and thus limit the achievable power density of very large wind farms. Thus the advection of upstream kinetic energy is not considered here. The above-named sources are calculated as follows.

The resolved downward turbulent flux of mean kinetic energy at rotor top level, averaged between $y = 120\text{ km} - s_y$ and $y = 120\text{ km} + s_y$, is calculated by multiplying the shear stress by the corresponding wind velocity component at that height:

$$W_{vkef}(x_i) = \langle -\rho(\bar{u} \overline{w'u'} + \bar{v} \overline{w'v'})|_{z=z_t} \rangle_y. \quad (16)$$

The power density of the energy input by the geostrophic pressure gradient on the flow below rotor top level $z_t =$

270 m is calculated as follows:

$$W_{\text{gpg,wt}}(x_i) = \int_{z=0}^{z_i} \rho f_c(u_g \bar{v}(z) - v_g \bar{u}(z)) dz|_{y=120 \text{ km}}. \quad (17)$$

The work done by the geostrophic pressure gradient on the rest of the BL (between z_i and z_i) is calculated as follows:

$$W_{\text{gpg,BL}}(x_i) = \int_{z=z_i}^{z_i} \rho f_c(u_g \bar{v}(z) - v_g \bar{u}(z)) dz|_{y=120 \text{ km}}. \quad (18)$$

The power density of the energy input by the perturbation pressure gradient on the flow below rotor top level is calculated as follows:

$$W_{\text{ppg,wt}}(x_i) = - \int_{z=0}^{z_i} \frac{\partial p^*(z)}{\partial x} \bar{u}(z) + \frac{\partial p^*(z)}{\partial y} \bar{v}(z) dz|_{y=120 \text{ km}}. \quad (19)$$

The power densities of the wind turbines are defined as follows:

$$W_{\text{wt}} = \frac{P_{\text{wt}}}{s_x s_y}. \quad (20)$$

The power densities are shown in Fig. 11. For the case NBL-700-7D it can be seen that the first-row wind turbines operate at the reference power so that a high power density of $W_{\text{wt}} = 12.56 \text{ MW}/(7D)^2 = 4.45 \text{ W m}^{-2}$ is achieved. The dominant energy source for the first turbine rows is the advection of kinetic energy. The advection is not included in Fig. 11 because it is larger than the other terms and would make the quantification of the smaller terms difficult. The power density of downstream wind turbines is determined by the vertical kinetic energy flux. Because the vertical kinetic energy flux decays from 3 W m^{-2} at the beginning of the first wind farm to 2 W m^{-2} at the end of the last wind farm, the power density of the wind turbines also decays to below 2 W m^{-2} . The good correlation between the wind turbine power density and the vertical kinetic energy flux has also been found by Stevens et al. (2016) for the fully developed regime in a 9 km long wind farm. The work done by the geostrophic pressure gradient on the flow below the rotor top level achieves a power density of approximately 0.6 W m^{-2} . It is thus not the dominating energy source inside the wind farms, but it still contributes approximately 20% to the sum of all sources $W_{\text{total}} = W_{\text{vkef}} + W_{\text{gpg,wt}} + W_{\text{ppg,wt}}$. In the downstream half of the wind farms the ratio between the wind turbine power and W_{total} is approximately 70%.

Although the vertical kinetic energy flux does not reach a constant value until the end of the wind farms, it is likely that it approaches the power density of the work done by the pressure gradient on the BL flow above the wind turbine level $W_{\text{gpg,BL}}$. Therefore, the flow approaches the fully developed regime of an infinite wind farm flow, in which all the energy

extracted by the wind turbines is provided by the work done by the geostrophic pressure gradient on the BL flow (Johnstone and Coleman, 2012; Abkar and Porté-Agel, 2014).

The energy input by the geostrophic pressure gradient into the entire BL ($W_{\text{gpg,wt}} + W_{\text{gpg,BL}}$) achieves power densities of only $1\text{--}2 \text{ W m}^{-2}$, which is consistent with the geophysical limits to power densities of large wind farms found by Antonini and Caldeira (2021), who reported approximately 1.5 W m^{-2} for a latitude of 46° and a geostrophic wind speed of 12 m s^{-1} . This power density is much smaller than the power density achieved by the first-row wind turbines. As the case NBL-700-5D shows (Fig. 11b), a reduction of the turbine spacing from $s = 7D$ to $s = 5D$ approximately results in a doubling of the power density of the first-row wind turbines (from 4.5 to 8.5 W m^{-2}), but the power density of the last-row wind turbines is as low as for $s = 7D$. This result indicates that the turbine spacing for very large wind farms should be chosen to be much larger than for small wind farms to achieve a good wind farm efficiency. That the wind farm power output is limited by the vertical kinetic energy flux has also been found by Badger et al. (2020), who investigated potential wind farm scenarios in the German Bight using a mesoscale weather forecast model (WRF) and a simple box model (KEBA, kinetic energy budget of the atmosphere). Nishino (2013) used a simple, theoretical approach to show that the power density of very large wind farms is limited by the energy input of the pressure gradient and that the power density is proportional to $\tau_0 U_h$, where τ_0 is the shear stress near the surface, and U_h is the mean wind speed at hub height for an undisturbed flow without wind farms. However, Nishino (2013) neglects the effect of the wind farm on the flow inside the BL. According to Abkar and Porté-Agel (2014) and Eq. (18), the energy input by the pressure gradient depends on the BL height and on the ageostrophic wind speed component averaged over the BL. The BL height increases due to the presence of the wind farms, and the ageostrophic wind speed component increases due to the counterclockwise wake deflection (see Fig. 11f). Consequently, the wind-farm-induced flow effects result in a significant increase in the energy input by the pressure gradient, as can be seen in Fig. 11a and b. This effect occurs only in the wake, although the BL height and wind direction already change inside the wind farms. The reason is the decrease in the absolute wind speed that tends to reduce the ageostrophic wind speed component and thus compensates for the increasing ratio of ageostrophic to geostrophic wind speed (counterclockwise wind direction change). In the wake, the wind speed recovers, and thus the ageostrophic wind speed component becomes larger than that upstream of the wind farms. The described effect is largest for the case with the small turbine spacing, NBL-700-5D, because the BL growth and the wake deflection angle are largest for this case.

Figure 11c and d show that a doubling of the BL height has approximately no effect on the energy input by the geostrophic pressure gradient ($W_{\text{gpg,wt}} + W_{\text{gpg,BL}}$) on the

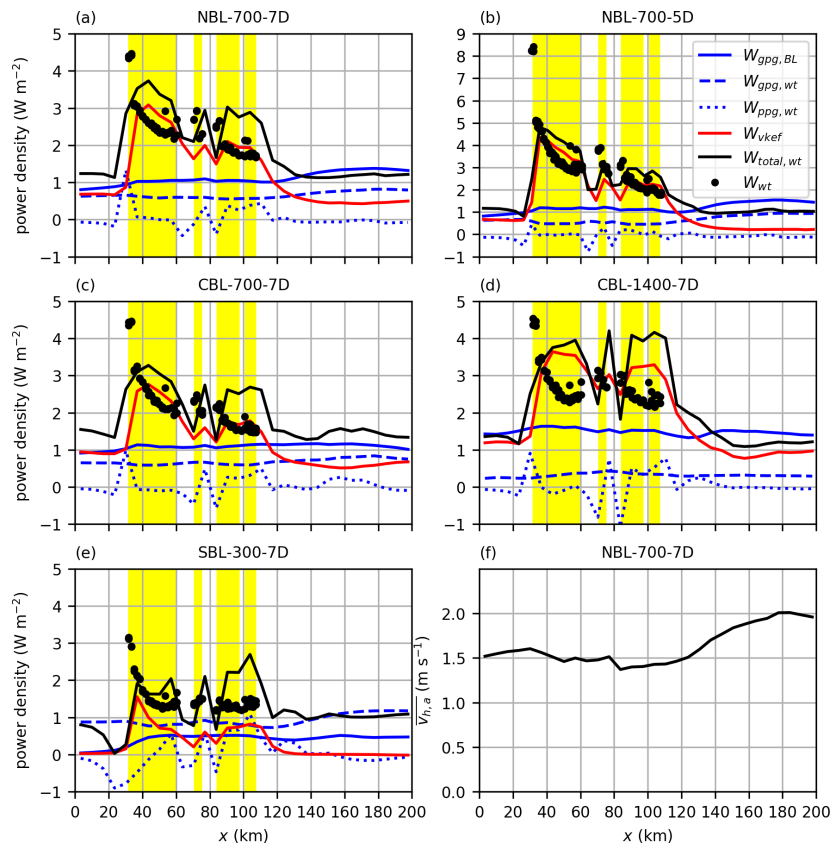


Figure 11. Comparison of power density provided by the geostrophic pressure gradient below rotor top level $W_{gpg,wt}$ and above rotor top level $W_{gpg,BL}$, the perturbation pressure gradient below rotor top level $W_{ppg,wt}$, the vertical kinetic energy flux at rotor top level W_{vkef} , and $W_{total,wt}$ as the sum of $W_{gpg,wt}$, $W_{ppg,wt}$ and W_{vkef} . The power density of the wind turbines located between $y = 120 - s_y$ and $y = 120 + s_y$ is shown for comparison. Wind farm locations are marked by yellow areas. Panel (f) shows the ageostrophic wind speed component ($\overline{v}_{h,a}$) at hub height for the case NBL-700-7D at $y = 120$ km.

undisturbed inflow. The effect of the thicker BL is compensated for by a smaller ageostrophic wind speed component inside the BL. This is indicated by a much smaller angle between hub height wind and the geostrophic wind of $\alpha = 3.4^\circ$ for the case CBL-1400-7D than $\alpha = 9.5^\circ$ for the case CBL-700-7D (see Table 1 and Fig. 3). Consequently, the ageostrophic wind speed component inside the BL of the stationary inflow adjusts in such a way that the resulting energy input by the pressure gradient balances the energy extraction by TKE production near the surface. As stated earlier, the power output of infinitely large wind farms is determined by the energy input of the geostrophic pressure gradient, which does not depend on the BL height. Hence, the power output of infinitely large wind farms is expected not to depend on the BL height, at least for this idealized setup with a stationary CBL inflow. However, for very large but finite-sized wind farms, as in this study, the power output depends significantly on the BL height, as is shown in Fig. 11c and d. The

vertical kinetic energy flux is greater and decays slower for the thicker BL (CBL-1400-7D), resulting in higher turbine power densities.

The case SBL-300-7D is very special because the rotor top level matches the BL height of the inflow. Thus, the energy input by the pressure gradient above the rotor top level, as well as the vertical kinetic energy flux at the rotor top level, is zero upstream of the wind farms. Both components become non-zero inside the wind farms due to the vertical displacement of the inversion layer (BL growth). For the first 10 km of the wind farms the vertical kinetic energy flux dominates, but further downstream, the energy input by the geostrophic pressure gradient below rotor top level is greater than or equal to the vertical kinetic energy flux. As stated earlier, the blockage effect redistributes energy from the wind farm leading edge into the wind farm, which results in a smaller power density of the first-row wind turbines compared to the other 7D cases and in a constant power density from approxi-

mately row 10. This redistribution is done by a favorable perturbation pressure gradient inside the wind farms and reaches power densities of approximately 1 W m^{-2} . In the wake, the vertical kinetic energy flux at rotor top level drops to zero again, which is consistent with the very low TI in the wake (see Fig. 6).

These results show that the power output and the wake of very large wind farms behave very differently compared to small wind farms. The main findings and their implications are summarized in the next section.

4 Conclusions

This study investigates wake properties and power output of very large wind farms with different turbine spacings in boundary layers (BLs) of different stabilities and heights. Very large wind farms do not only change wind speed and turbulence intensity (TI) at wind turbine level but rather affect several flow quantities inside the entire BL and even above the BL. BL growth, counterclockwise flow deflection inside the BL and clockwise flow deflection above the BL are the main effects that distinguish large from small wind farm flows. Wake lengths of very large wind farms are longer for shallower BLs and smaller turbine spacings, reaching values of more than 100 km. Thus, very large wind farms in the German Bight have the potential to affect the wind farm performance of neighboring states such as Denmark or the Netherlands. The wake length in terms of TI is relatively independent of the wind farm size and is in general much smaller (approximately 20 km) than the wake length in terms of speed deficit. Longer TI wakes occur for convective BLs and shorter wakes for stable BLs due to the buoyancy-driven turbulence production or destruction.

For shallow, stable BLs very large wind farms trigger large-scale gravity waves in the free atmosphere that cause significant flow blockage, affecting also smaller wind farms that are nearby. Some tuning of the domain height and the boundary conditions was necessary to obtain stable simulation results. Because shallow BLs occur quite frequently in the German Bight, it is an important task to find best practice rules for simulation setups that capture this phenomenon as realistically as possible.

The wind speed recovery inside the wind farms is mainly driven by the turbulent vertical momentum flux, but the wind speed recovery in the wake of very large wind farms is mainly driven by the geostrophic pressure gradient force. Thus, it is expected that the wake recovery of very large wind farms depends rather on the ageostrophic wind speed component than on parameters that affect the turbulent momentum flux such as stability or TI. Further investigations are needed to prove this hypothesis.

The power output of very large wind farms is limited by the available kinetic energy inside the BL and the energy input by the geostrophic pressure gradient. The achieved power

density of turbines in the upstream part of the wind farms is significantly affected by the BL height, whereas the power density of the downstream turbines approaches the power density given by the energy input of the geostrophic pressure gradient. Because this power density is only as small as 2 W m^{-2} , high wind farm efficiencies can only be achieved by large turbine spacings. BL growth and wake deflection towards lower pressure tend to increase the power input by the geostrophic pressure gradient, which could have a positive effect on the power output of downstream wind farms.

Overall, the results show that very large wind farms trigger much more complex flow effects than small wind farms do. It will be necessary to consider at least some of these effects in simple wake models in order to accurately predict the power output of very large wind farms. One of the next research tasks could be to derive empirical rules for predicting the power output of very large wind farms by performing a more systematic and idealized set of simulations.

Appendix A: COSMO-REA6 climatology

This Appendix includes histograms of wind speed (Fig. A1), wind direction (Fig. A2) and boundary layer height for convective boundary layers (Fig. A3) and stable boundary layers (Fig. A4) for a point at 178 m height at $54^{\circ}30' \text{ N}$, $6^{\circ}00' \text{ E}$, which is located inside Zone 3 in the German Bight. The histograms are obtained from the COSMO-REA6 dataset that contains hourly data from the years 1995 to 2018. The boundary layer height in COSMO-REA6 is defined as the height at which the bulk Richardson number reaches the critical Richardson number, which is 0.22 under convective conditions and 0.33 under stable conditions (personal communication with Eckhard Kadasch, German Weather Service, Offenbach, on 23 May 2019). The histograms were provided by Thomas Spanghel from the German Weather Service. Note that convective boundary layers occur 59.5 % of the time ($n = 125088$, Fig. A3) and stable boundary layers occur 40.5 % of the time ($n = 85247$, Fig. A4).

736

O. Maas and S. Raasch: Wake properties and power output of very large wind farms

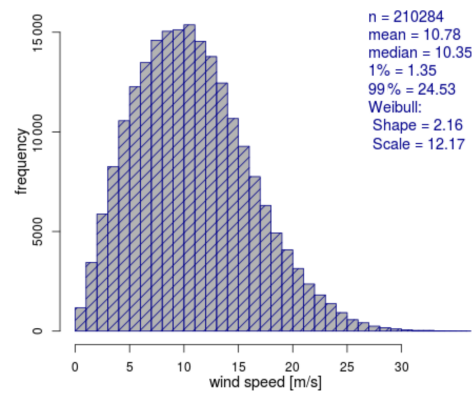


Figure A1. Wind speed histogram with total number of samples (n), mean wind speed, median wind speed, 1 % and 99 % percentiles, and Weibull shape and scale parameters.

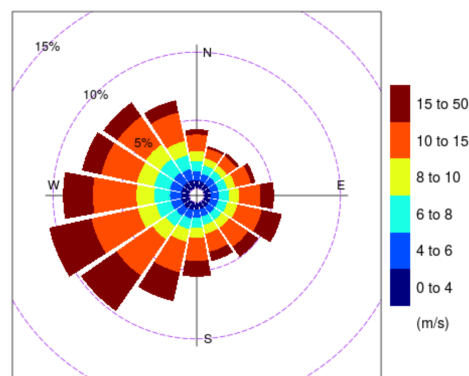


Figure A2. Wind direction histogram. Wind speed bins are indicated by different colors.

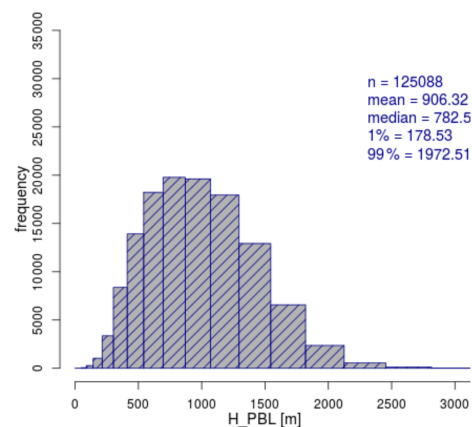


Figure A3. Boundary layer height histogram for convective boundary layers (surface temperature greater than 2 m temperature).

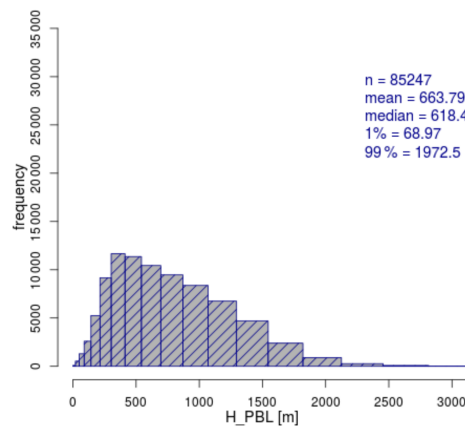


Figure A4. Boundary layer height histogram for stable boundary layers (surface temperature smaller than 2 m temperature).

Code and data availability. The PALM code, PALM input files and plot scripts are available at <https://doi.org/10.25835/0004522> (Maas and Raasch, 2021; PALM, 2022). Output data are available on request.

Author contributions. OM and SR selected and designed the simulated cases. OM performed the simulations and wrote the manuscript. Data analysis and manuscript preparation were guided by SR.

Competing interests. The contact author has declared that neither they nor their co-author has any competing interests.

Disclaimer. Publisher's note: Copernicus Publications remains neutral with regard to jurisdictional claims in published maps and institutional affiliations.

Acknowledgements. The work was supported by the North German Supercomputing Alliance (HLRN). We thank Thomas Spanghel (German Weather Service) for providing the figures in the Appendix. Special thanks goes to Christopher Mount for English proofreading and to Dries Allaerts for informative discussions about wind-farm-induced gravity waves.

Financial support. This work was funded by the Federal Maritime and Hydrographic Agency (BSH) (grant no. 10044580).

Review statement. This paper was edited by Sandrine Aubrun and reviewed by Dries Allaerts and one anonymous referee.

References

- Abkar, M. and Porté-Agel, F.: The effect of free-atmosphere stratification on boundary-layer flow and power output from very large wind farms, *Energies*, 6, 2338–2361, <https://doi.org/10.3390/en6052338>, 2013.
- Abkar, M. and Porté-Agel, F.: Mean and turbulent kinetic energy budgets inside and above very large wind farms under conventionally-neutral condition, *Renew. Energ.*, 70, 142–152, <https://doi.org/10.1016/j.renene.2014.03.050>, 2014.
- Allaerts, D. and Meyers, J.: Effect of Inversion-Layer Height and Coriolis Forces on Developing Wind-Farm Boundary Layers, in: 34th Wind Energy Symposium, Wind Energy: Wind Plant Aerodynamics and Atmospheric Inflow, San Diego, California, USA, 4–8 January 2016, 1–5, <https://doi.org/10.2514/6.2016-1989>, 2016.
- Allaerts, D. and Meyers, J.: Boundary-layer development and gravity waves in conventionally neutral wind farms, *J. Fluid Mech.*, 814, 95–130, <https://doi.org/10.1017/jfm.2017.11>, 2017.
- Antonini, E. G. and Caldeira, K.: Atmospheric pressure gradients and Coriolis forces provide geophysical limits to power density of large wind farms, *Appl. Energ.*, 281, 116048, <https://doi.org/10.1016/j.apenergy.2020.116048>, 2021.
- Badger, J., Imberger, M., Volker, P., Kleidon, A., Germer, S., and Minz, J.: Making the Most of Offshore Wind, in: *Agora Energiewende, Agora Verkehrswende*, Technical University of Denmark and Max-Planck-Institute for Biogeochemistry, 84 pp., https://pure.mpg.de/rest/items/item_3213814

- component/file_3213815/content (last access: 22 March 2022), 2020.
- Basu, S., Holtslag, A. A., Wiel, B. J., Moene, A. F., and Steeneveld, G. J.: An inconvenient “truth” about using sensible heat flux as a surface boundary condition in models under stably stratified regimes, *Acta Geophys.*, 56, 88–99, <https://doi.org/10.2478/s11600-007-0038-y>, 2008.
- Calaf, M., Meneveau, C., and Meyers, J.: Large eddy simulation study of fully developed wind-turbine array boundary layers, *Phys. Fluids*, 22, 015110, <https://doi.org/10.1063/1.3291077>, 2010.
- Calaf, M., Parlange, M. B., and Meneveau, C.: Large eddy simulation study of scalar transport in fully developed wind-turbine array boundary layers, *Phys. Fluids*, 23, 126603, <https://doi.org/10.1063/1.3663376>, 2011.
- Churchfield, M. J., Lee, S., Moriarty, P. J., Martínez, L. A., Leonardi, S., Vijayakumar, G., and Brasseur, J. G.: A large-eddy simulation of wind-plant aerodynamics, in: 50th AIAA Aerospace Sciences Meeting Including the New Horizons Forum and Aerospace Exposition, Nashville, Tennessee, USA, 9–12 January 2012, AIAA 2012-0537, <https://doi.org/10.2514/6.2012-537>, 2012.
- Dai, Y., Basu, S., Maronga, B., and de Roode, S. R.: Addressing the Grid-Size Sensitivity Issue in Large-Eddy Simulations of Stable Boundary Layers, *Bound.-Lay. Meteorol.*, 178, 63–89, <https://doi.org/10.1007/s10546-020-00558-1>, 2021.
- Deardorff, J. W.: Stratocumulus-capped mixed layers derived from a three-dimensional model, *Bound.-Lay. Meteorol.*, 18, 495–527, <https://doi.org/10.1007/BF00119502>, 1980.
- Dörenkämper, M., Witha, B., Steinfeld, G., Heinemann, D., and Kühn, M.: The impact of stable atmospheric boundary layers on wind-turbine wakes within offshore wind farms, *J. Wind Eng. Ind. Aerod.*, 144, 146–153, <https://doi.org/10.1016/j.jweia.2014.12.011>, 2015.
- Fang, J. and Porté-Agel, F.: Large-Eddy Simulation of Very-Large-Scale Motions in the Neutrally Stratified Atmospheric Boundary Layer, *Bound.-Lay. Meteorol.*, 155, 397–416, <https://doi.org/10.1007/s10546-015-0006-z>, 2015.
- Frandsen, S.: On the wind speed reduction in the center of large clusters of wind turbines, *J. Wind Eng. Ind. Aerod.*, 39, 251–265, [https://doi.org/10.1016/0167-6105\(92\)90551-K](https://doi.org/10.1016/0167-6105(92)90551-K), 1992.
- Gaertner, E., Rinker, J., Sethuraman, L., Zahle, F., Anderson, B., Barter, G., Abbas, N., Meng, F., Bortolotti, P., Skrzypinski, W., Scott, G., Feil, R., Bredmose, H., Dykes, K., Shields, M., Allen, C., and Viselli, A.: Definition of the IEA Wind 15-Megawatt Offshore Reference Wind Turbine, National Renewable Energy Laboratory, Golden, Colorado, USA, Tech. rep. NREL/TP-5000-75698, 54 pp., <https://www.nrel.gov/docs/fy20osti/75698.pdf> (last access: 22 March 2022), 2020.
- Herzig, G.: Global Offshore Wind Report 2020, Tech. Rep. February, https://wfo-global.org/wp-content/uploads/2021/02/WFO_Global-Offshore-Wind-Report-2020.pdf (last access: 22 March 2022), 2020.
- Johnstone, R. and Coleman, G. N.: The turbulent Ekman boundary layer over an infinite wind-turbine array, *J. Wind Eng. Ind. Aerod.*, 100, 46–57, <https://doi.org/10.1016/j.jweia.2011.11.002>, 2012.
- Kataoka, H. and Mizuno, M.: Numerical flow computation around aeroelastic 3D square cylinder using inflow turbulence, *Wind Struct.*, 5, 379–392, https://doi.org/10.12989/was.2002.5.2_3_4.379, 2002.
- Kosović, B. and Curry, J. A.: A large eddy simulation study of a quasi-steady, stably stratified atmospheric boundary layer, *J. Atmos. Sci.*, 57, 1052–1068, [https://doi.org/10.1175/1520-0469\(2000\)057<1052:ALESSO>2.0.CO;2](https://doi.org/10.1175/1520-0469(2000)057<1052:ALESSO>2.0.CO;2), 2000.
- Lu, H. and Porté-Agel, F.: Large-eddy simulation of a very large wind farm in a stable atmospheric boundary layer, *Phys. Fluids*, 23, 065101, <https://doi.org/10.1063/1.3589857>, 2011.
- Lund, T., Wu, X., and Squires, K. D.: Generation of turbulent inflow data for spatially-developing boundary layer simulations, *J. Comput. Phys.*, 140, 233–258, 1998.
- Maronga, B., Banzhaf, S., Burmeister, C., Esch, T., Forkel, R., Fröhlich, D., Fuka, V., Gehrke, K. F., Geletič, J., Giersch, S., Gronemeier, T., Groß, G., Heldens, W., Hellsten, A., Hoffmann, F., Inagaki, A., Kadasch, E., Kanani-Sühring, F., Ketelsen, K., Khan, B. A., Knigge, C., Knoop, H., Krč, P., Kurppa, M., Maamari, H., Matzarakis, A., Mauder, M., Pallasch, M., Pavlik, D., Pfafferoth, J., Resler, J., Rissmann, S., Russo, E., Salim, M., Schrempf, M., Schwenkel, J., Seckmeyer, G., Schubert, S., Sühring, M., von Tils, R., Vollmer, L., Ward, S., Witha, B., Wurps, H., Zeidler, J., and Raasch, S.: Overview of the PALM model system 6.0, *Geosci. Model Dev.*, 13, 1335–1372, <https://doi.org/10.5194/gmd-13-1335-2020>, 2020.
- Maas, O. and Raasch, S.: Wake properties and power output of very large wind farms in the German Bight, Leibniz Universität Hannover [data set], <https://doi.org/10.25835/0004522>, 2021.
- Miller, M. J. and Thorpe, A. J.: Radiation conditions for the lateral boundaries of limited-area numerical models, *Q. J. Roy. Meteor. Soc.*, 107, 615–628, <https://doi.org/10.1002/qj.49710745310>, 1981.
- Moeng, C.-H. and Wyngaard, J. C.: Spectral Analysis of Large-Eddy Simulations of the Convective Boundary Layer, *J. Atmos. Sci.*, 45, 3573–3587, [https://doi.org/10.1175/1520-0469\(1988\)045<3573:SAOLES>2.0.CO;2](https://doi.org/10.1175/1520-0469(1988)045<3573:SAOLES>2.0.CO;2), 1988.
- Munters, W., Meneveau, C., and Meyers, J.: Shifted periodic boundary conditions for simulations of wall-bounded turbulent flows, *Phys. Fluids*, 28, 025112, <https://doi.org/10.1063/1.4941912>, 2016.
- Nilsson, K., Ivanell, S., Hansen, K. S., Mikkelsen, R., Sørensen, J. N., Breton, S.-P., and Henningson, D.: Large-eddy simulations of the Lillgrund wind farm, *Wind Energy*, 18, 449–467, <https://doi.org/10.1002/we.1707>, 2015.
- Nishino, T.: Limits to the power density of very large wind farms, arXiv [draft], arXiv:1309.4943, 2013.
- Orlanski, I.: A simple boundary condition for unbounded hyperbolic flows, *J. Comput. Phys.*, 21, 251–269, [https://doi.org/10.1016/0021-9991\(76\)90023-1](https://doi.org/10.1016/0021-9991(76)90023-1), 1976.
- PALM Model System: Leibniz Universität Hannover [code], <https://palm.muk.uni-hannover.de/trac>, last access: 22 March 2022.
- Porté-Agel, F., Wu, Y. T., and Chen, C. H.: A numerical study of the effects of wind direction on turbine wakes and power losses in a large wind farm, *Energies*, 6, 5297–5313, <https://doi.org/10.3390/en6105297>, 2013.
- Porté-Agel, F., Bastankhah, M., and Shamsoddin, S.: Wind-Turbine and Wind-Farm Flows: A Review, *Bound.-Lay. Meteorol.*, 174, 1–59, <https://doi.org/10.1007/s10546-019-00473-0>, 2020.

- Saiki, E. M., Moeng, C.-H., and Sullivan, P. P.: Large-Eddy Simulation Of The Stably Stratified Planetary Boundary Layer, *Bound.-Lay. Meteorol.*, 95, 1–30, <https://doi.org/10.1023/A:1002428223156>, 2000.
- Steinfeld, G., Witha, B., Dörenkämper, M., and Gryschka, M.: Hochauflösende Large-Eddy-Simulationen zur Untersuchung der Strömungsverhältnisse in Offshore-Windparks, *promet – Meteorologische Fortbildung*, 39, 163–180, 2015.
- Stevens, R. J., Gayme, D. F., and Meneveau, C.: Effects of turbine spacing on the power output of extended wind-farms, *Wind Energy*, 19, 359–370, <https://doi.org/10.1002/we.1835>, 2016.
- van der Laan, M. P. and Sørensen, N. N.: Why the Coriolis force turns a wind farm wake clockwise in the Northern Hemisphere, *Wind Energ. Sci.*, 2, 285–294, <https://doi.org/10.5194/wes-2-285-2017>, 2017.
- Vosper, S. B., Wells, H., and Brown, A. R.: Accounting for non-uniform static stability in orographic drag parametrization, *Q. J. Roy. Meteor. Soc.*, 135, 815–822, <https://doi.org/10.1002/qj.407>, 2009.
- WindSeeG: Gesetz zur Entwicklung und Förderung der Windenergie auf See (Windenergie-auf-See-Gesetz – WindSeeG), Bundesministerium der Justiz, <http://www.gesetze-im-internet.de/windseeg/> (last access: 22 March 2022), 2020.
- Witha, B., Steinfeld, G., Dörenkämper, M., and Heinemann, D.: Large-eddy simulation of multiple wakes in offshore wind farms, *J. Phys. Conf. Ser.*, 555, 012108, <https://doi.org/10.1088/1742-6596/555/1/012108>, 2014.
- Wu, K. L. and Porté-Agel, F.: Flow adjustment inside and around large finite-size wind farms, *Energies*, 10, 4–9, <https://doi.org/10.3390/en10122164>, 2017.
- Wu, Y.-T. and Porté-Agel, F.: Large-Eddy Simulation of Wind-Turbine Wakes: Evaluation of Turbine Parametrisations, *Bound.-Lay. Meteorol.*, 138, 345–366, <https://doi.org/10.1007/s10546-010-9569-x>, 2011.
- Wu, Y.-T. and Porté-Agel, F.: Modeling turbine wakes and power losses within a wind farm using LES: An application to the Horns Rev offshore wind farm, *Renew. Energ.*, 75, 945–955, <https://doi.org/10.1016/j.renene.2014.06.019>, 2015.
- Zilitinkevich, S., Esau, I., and Baklanov, A.: Further comments on the equilibrium height of neutral and stable planetary boundary layers, *Q. J. Roy. Meteor. Soc.*, 133, 265–271, <https://doi.org/10.1002/qj.27>, 2007.

4 From gigawatt to multi-gigawatt wind farms: wake effects, energy budgets and inertial gravity waves investigated by large-eddy simulations

4.1 Declaration of Contributions

O. Maas performed the simulations and wrote the manuscript. The manuscript preparation was guided by S. Raasch. The paper was edited by Sara C. Pryor and reviewed by Dries Allaerts and two anonymous referees.

4.2 Research Article

Maas, O.: From gigawatt to multi-gigawatt wind farms: wake effects, energy budgets and inertial gravity waves investigated by large-eddy simulations, *Wind Energy Science*, 8, 535–556, doi: 10.5194/wes-8-535-2023, 2023a.

©The author 2023. CC BY 4.0 License

Wind Energ. Sci., 8, 535–556, 2023
<https://doi.org/10.5194/wes-8-535-2023>
© Author(s) 2023. This work is distributed under
the Creative Commons Attribution 4.0 License.



From gigawatt to multi-gigawatt wind farms: wake effects, energy budgets and inertial gravity waves investigated by large-eddy simulations

Oliver Maas

Institute of Meteorology and Climatology, Leibniz University Hannover, Hanover, Germany

Correspondence: Oliver Maas (maas@meteo.uni-hannover.de)

Received: 6 July 2022 – Discussion started: 26 July 2022

Revised: 4 January 2023 – Accepted: 12 March 2023 – Published: 13 April 2023

Abstract. The size of newly installed offshore wind farms increases rapidly. Planned offshore wind farm clusters have a rated capacity of several gigawatts and a length of up to 100 km. The flow through and around wind farms of this scale can be significantly different than the flow through and around smaller wind farms on the sub-gigawatt scale. A good understanding of the involved flow physics is vital for accurately predicting the wind farm power output as well as predicting the meteorological conditions in the wind farm wake. To date there is no study that directly compares small wind farms (sub-gigawatt) with large wind farms (super-gigawatt) in terms of flow effects or power output. The aim of this study is to fill this gap by providing this direct comparison by performing large-eddy simulations of a small wind farm (13 km length) and a large wind farm (90 km length) in a convective boundary layer, which is the most common boundary layer type in the North Sea.

The results show that there are significant differences in the flow field and the energy budgets of the small and large wind farm. The large wind farm triggers an inertial wave with a wind direction amplitude of approximately 10° and a wind speed amplitude of more than 1 m s^{-1} . In a certain region in the far wake of a large wind farm the wind speed is greater than far upstream of the wind farm, which can be beneficial for a downstream located wind farm. The inertial wave also exists for the small wind farm, but the amplitudes are approximately 4 times weaker and thus may be hardly observable in real wind farm flows that are more heterogeneous. Regarding turbulence intensity, the wake of the large wind farm has the same length as the wake of the small wind farm and is only a few kilometers long. Both wind farms trigger inertial gravity waves in the free atmosphere, whereas the amplitude is approximately twice as large for the large wind farm. The inertial gravity waves induce streamwise pressure gradients inside the boundary layer, affecting the energy budgets of the wind farms. The most dominant energy source of the small wind farm is the horizontal advection of kinetic energy, but for the large wind farm the vertical turbulent flux of kinetic energy is 5 times greater than the horizontal advection of kinetic energy. The energy input by the gravity-wave-induced pressure gradient is greater for the small wind farm because the pressure gradient is greater. For the large wind farm, the energy input by the geostrophic forcing (synoptic-scale pressure gradient) is significantly enhanced by the wind direction change that is related to the inertial oscillation. For both wind farms approximately 75 % of the total available energy is extracted by the wind turbines and 25 % is dissipated.

1 Introduction

The size of newly installed offshore wind farms increases rapidly. The largest wind farm in operation Moray East (United Kingdom) has a rated capacity of 950 MW and consists of 100 wind turbines (Herzig, 2022). The largest wind farm under construction is Hollandse Kust Zuid (Netherlands), with a rated capacity of 1540 MW. It consists of 140 wind turbines and has a length of approximately 15 km (Herzig, 2022). Offshore wind farms are often arranged in clusters, so that the cluster capacity can already be in the multi-gigawatt scale. One example is the planned wind farm cluster in Zone 3 in the German Bight with a planned capacity of 20 GW and a length of approximately 100 km (BSH, 2021).

The flow through and around wind farms of this scale can be significantly different than the flow through and around smaller wind farms on the sub-gigawatt scale, as recently published results show. For example, large wind farms can cause a significant counterclockwise wind direction change in the wake and a vertical displacement of the inversion layer above the wind farm (Allaerts and Meyers, 2016; Lanzilao and Meyers, 2022; Maas and Raasch, 2022). A good understanding of the involved flow physics is vital for accurately predicting the wind farm power output as well as predicting the meteorological conditions in the wind farm wake. The “improved understanding of atmospheric and wind power plant flow physics” is stated as one of the grand challenges in the science of wind energy by Veers et al. (2019) because the involved scales range from microscale to mesoscale and interactions can be complex. The best numerical method for the investigation of these interactions that considers all relevant physical processes but is still computationally feasible is large-eddy simulation (LES).

In recent years many LES studies investigated wind farm flows. The studies can be subdivided into three categories. The first category investigates infinitely large wind farms by using cyclic boundary conditions in both lateral directions, e.g., Abkar and Porté-Agel (2013), Abkar and Porté-Agel (2014), Calaf et al. (2010), Calaf et al. (2011), Johnstone and Coleman (2012), Lu and Porté-Agel (2011), Lu and Porté-Agel (2015), Meyers and Meneveau (2013), Porté-Agel et al. (2014) and VerHulst and Meneveau (2014). The second category investigates semi-infinite wind farms by using cyclic boundary conditions only in the crosswise direction, e.g., Allaerts and Meyers (2016), Allaerts and Meyers (2017), Allaerts and Meyers (2018), Andersen et al. (2015), Centurelli et al. (2021), Segalini and Chericoni (2021), Stevens et al. (2016), Wu and Porté-Agel (2017) and Zhang et al. (2019). The third category investigates wind farms that have a finite size in both lateral directions which also include real wind farms, e.g., Dörenkämper et al. (2015), Ghaisas et al. (2017), Lanzilao and Meyers (2022), Maas and Raasch (2022), Nilsson et al. (2015), Porté-Agel et al. (2013), Witha et al. (2014) and Wu and Porté-Agel (2015).

Typical wind farm lengths in the semi-infinite wind farm studies range from 5 km (Centurelli et al., 2021) over 15 km (Allaerts and Meyers, 2017) to 24 km (Andersen et al., 2015). Typical wind farm lengths in the finite-size wind farm studies range from 2 km (Witha et al., 2014) over 15 km (Lanzilao and Meyers, 2022) to approximately 100 km (Maas and Raasch, 2022). Thus, most of the studies are representative for existing, state-of-the-art wind farms and do not represent the spatial scales that future wind farm clusters will have. Specifically, there is no study that directly compares small wind farms (10 km scale) with large wind farms (100 km scale) in terms of flow effects or power output, neither with LESs nor with simpler models.

The aim of this study is to provide this direct, systematic comparison by performing LESs of a small wind farm (13 km length) and a large wind farm (90 km length) with a semi-infinite wind farm setup. The comparison focuses on the boundary layer flow inside the wind farm but also in the far wake and the overlying free atmosphere. A detailed energy budget analysis is made to identify the dominant energy sources and sinks for small and large wind farms. The domain is more than 400 km long to cover the far wake and has a height of 14 km to cover wind-farm-induced gravity waves. The boundary layer is filled with a turbine-wake-resolving grid resulting in more than 2 billion grid points in total.

The paper is structured as follows. The numerical model and the main and precursor simulations are described in Sect. 2. The simulation results are presented in Sect. 3, and Sect. 4 concludes and discusses the results of the study.

2 Methods

2.1 Numerical model

The simulations are carried out with the Parallelized Large-eddy Simulation Model (PALM; Maronga et al., 2020). PALM is developed at the Institute of Meteorology and Climatology of Leibniz Universität Hannover, Germany. Several wind farm flow investigations have been successfully conducted with this code in the past (e.g., Witha et al., 2014; Dörenkämper et al., 2015; Maas and Raasch, 2022). PALM solves the non-hydrostatic, incompressible Navier–Stokes equations in Boussinesq-approximated form. The equations for the conservation of mass, momentum and internal energy then read as

$$\frac{\partial \tilde{u}_j}{\partial x_j} = 0, \quad (1)$$

$$\frac{\partial \tilde{u}_i}{\partial t} = -\frac{\partial \tilde{u}_i \tilde{u}_j}{\partial x_j} - \epsilon_{ijk} f_j \tilde{u}_k + \epsilon_{i3j} f_j u_{g,j} - \frac{1}{\rho_0} \frac{\partial \pi^*}{\partial x_i} + g \frac{\tilde{\theta} - \langle \tilde{\theta} \rangle}{\langle \tilde{\theta} \rangle} \delta_{i3} - \frac{\partial}{\partial x_j} (\widetilde{u_i' u_j'} - \frac{2}{3} e \delta_{ij}) + d_i, \quad (2)$$

$$\frac{\partial \tilde{\theta}}{\partial t} = -\frac{\partial \tilde{u}_j \tilde{\theta}}{\partial x_j} - \frac{\partial}{\partial x_j} (\widetilde{u_j' \theta''}), \quad (3)$$

where angular brackets indicate horizontal averaging and a double prime indicates subgrid-scale (SGS) quantities; a tilde denotes filtering over a grid volume; $i, j, k \in \{1, 2, 3\}$, u_i, u_j, u_k are the velocity components in the respective directions (x_i, x_j, x_k) ; θ is potential temperature; t is time; and $f_i = (0, 2\Omega \cos(\phi), 2\Omega \sin(\phi))$ is the Coriolis parameter with the Earth's angular velocity $\Omega = 0.729 \times 10^{-4} \text{ rad s}^{-1}$ and the geographical latitude ϕ . The geostrophic wind speed components are $u_{g,j}$, and the basic state density of dry air is ρ_0 . The modified perturbation pressure is $\pi^* = p + \frac{2}{3}\rho_0 e$, where p is the perturbation pressure and $e = \frac{1}{2}\widetilde{u_i''u_i''}$ is the SGS turbulence kinetic energy. The gravitational acceleration is $g = 9.81 \text{ m s}^{-2}$, δ is the Kronecker delta and d_i represents the forces of the wind turbine actuator discs.

The SGS model uses a 1.5-order closure according to Deardorff (1980), modified by Moeng and Wyngaard (1988) and Saiki et al. (2000). The wind turbines are represented by an advanced actuator disc model with rotation (ADM-R) that acts as an axial momentum sink and an angular momentum source (inducing wake rotation). The ADM-R is described in detail by Wu and Porté-Agel (2011) and was implemented in PALM by Steinfeld et al. (2015). Additional information is also given by Maas and Raasch (2022). The wind turbines have a yaw controller that aligns the rotor axis with the wind direction.

2.2 Main simulations

The study consists of two simulations. The first simulation contains a small wind farm with $N_x \times N_y = 8 \times 8 = 64$ wind turbines resulting in a length of 13.44 km. The second simulation contains a large wind farm with $N_x \times N_y = 48 \times 8 = 384$ wind turbines resulting in a length of 90.24 km (see Fig. 1). The wind farms extend over the entire domain width, and cyclic boundary conditions are applied in the y direction, so that the wind farms are effectively infinitely large in this direction. This idealized setup has been used in many other LES wind farm studies, e.g., Stevens et al. (2016), Allaerts and Meyers (2017) and Wu and Porté-Agel (2017). It simplifies the data analysis and allows us to focus only on streamwise variations in the wind farm and the wake. The validity of the results for finite-size, real wind farms is discussed in Sect. 4.

The IEA 15 MW wind turbine with a rotor diameter of $D = 240 \text{ m}$ and a rated power of 15 MW is used (Gaertner et al., 2020). The hub height is set to 180 m instead of 150 m, so that the turbulent fluxes at the rotor bottom are better resolved by the numerical grid. The wind turbines are arranged in a staggered configuration and have a streamwise and crosswise spacing of $s = 8D$, resulting in an installed capacity density of 4.07 W m^{-2} . The small wind farm has a length of 13.44 km, which corresponds approximately to the length of the currently largest wind farm under construction, Hollandse Kust Zuid. The large wind farm has a length

of 90.24 km, which corresponds approximately to the length of the planned wind farm cluster in Zone 3 in the German Bight. Note that the small wind farm is already as long as the largest wind farms of most other LES studies, e.g., Wu and Porté-Agel (2017) (19.6 km) and Allaerts and Meyers (2017) (15 km).

The domain has a length of $L_x = 409.6 \text{ km}$ to cover the far wake of the wind farms. The wind farms have a distance of 100 km to the inflow boundary, so that the wind-farm-induced flow blockage is covered. The domain width is $L_y = 15.36 \text{ km}$ for the small and large wind farm case. A domain height of $L_z = 14.0 \text{ km}$ is required to cover wind-farm-induced gravity waves. That the Boussinesq approximation is still valid for such a large domain height is shown in Appendix A. To avoid reflection of the waves at the domain top, there is a Rayleigh damping layer above $z_{\text{rd}} = 5 \text{ km}$. The Rayleigh damping factor increases from zero at the bottom of the damping layer to its maximum value of $f_{\text{rdm}} = 0.025(\Delta t)^{-1} \approx 0.017 \text{ s}^{-1}$ at the domain top according to this function (see Fig. 1):

$$f_{\text{rd}}(z) = f_{\text{rdm}} \sin^2 \left(0.5\pi \frac{z - z_{\text{rd}}}{L_z - z_{\text{rd}}} \right). \quad (4)$$

This sine wave profile leads to fewer reflections compared to a linear profile (Klemp and Lilly, 1978). The choice of these parameters is based on a set of test simulations with a larger grid spacing that are performed to find parameters that result in a low reflectivity. The reflectivity is obtained by the method described by Allaerts and Meyers (2017), which is a modified version of the method described by Taylor and Sarkar (2007). With the chosen parameters, less than 6 % of the upwards propagating wave energy is reflected.

The domain is filled with an equidistant regular grid with a grid spacing of 20 m, yielding a density of 12 grid points per rotor diameter. This is enough to resolve the most relevant eddies inside the wind turbine wakes. Steinfeld et al. (2015) showed that even eight grid points per rotor diameter are sufficient to obtain a converged result for the mean wind speed profiles at a downstream distance of $5D$. Above 900 m the grid is vertically stretched by 8 % per grid point up to a maximum vertical grid spacing of 200 m, which is enough for resolving the gravity waves with a vertical wavelength of approximately 5 km (see Table 1 in Sect. 3.4). The numerical grid has the same structure in both cases and contains $n_x \times n_y \times n_z = 20480 \times 768 \times 128 \approx 2.01 \times 10^9$ grid points.

The flow field is initialized by the instantaneous flow field of the last time step of a precursor simulation. Details about the precursor simulation and the meteorological parameters are given in the next section. The flow field is filled cyclically into the main domain because it is larger than the precursor domain. At the inflow, vertical velocity and temperature profiles averaged over the last 2 h of the precursor simulation are prescribed. The turbulent state of the inflow is maintained by a turbulence recycling method that maps the turbulent fluctuations from the recycling plane at

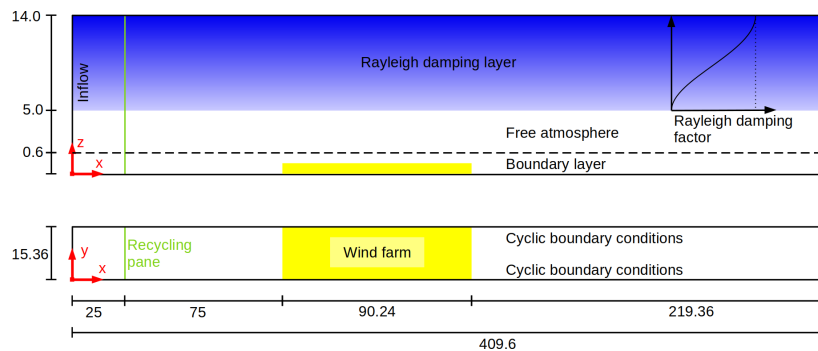


Figure 1. Side view and plan view of the domain and wind farm layout for the large wind farm case. Dimensions in kilometers.

$x = 25$ km onto the inflow plane at $x = 0$. Details of the recycling method are given in Maas and Raasch (2022). The large distance between inflow and recycling plane is chosen to cover elongated convection rolls that appear in the convective boundary layer (CBL) and to cover at least twice the advection distance of the convective timescale $U_g z_i / w_* = 9.011 \text{ m s}^{-1} 600 \text{ m} / 0.49 \text{ m s}^{-1} \approx 11 \text{ km}$, with the convective velocity scale $w_* = \left[\frac{g z_i}{\bar{\theta}} \langle w' \theta' \rangle_s \right]^{1/3}$, where $\bar{\theta} = 280 \text{ K}$ and $\langle w' \theta' \rangle_s$ is the horizontally averaged kinematic surface heat flux averaged over the last 4 h of the precursor simulation. For the potential temperature, the absolute value is recycled instead of the turbulent fluctuation, so that the inflow temperature increases according to the surface temperature. The otherwise constant inflow temperature profile would cause a streamwise temperature gradient that triggers a thermal circulation inside the entire domain. The turbulent fluctuations are shifted in the y direction by $+6.4 \text{ km}$ to avoid streamwise streaks in the averaged velocity fields; for further details please refer to Maas and Raasch (2022) and Munters et al. (2016). Radiation boundary conditions as described by Miller and Thorpe (1981) and Orlanski (1976) are used at the outflow plane. Hereby, the flow quantity q at the outflow boundary b is determined with the phase velocity \hat{c} and the upstream derivative of the flow quantity:

$$q_b^{t+\Delta t} = q_b^t - (\hat{c} \Delta t / \Delta x) (q_b^t - q_{b-1}^t). \quad (5)$$

The phase velocity \hat{c} is set to the maximum possible phase velocity of $\Delta x / \Delta t$. The surface boundary conditions and other parameters are the same as in the precursor simulation and are thus described in the next section. The physical simulation time of the main simulations is 20 h, and the presented data are averaged over the last 4 h.

2.3 Precursor simulation

Initial and inflow profiles of both simulations are obtained by a precursor simulation without a wind farm. It has cyclic boundary conditions in both lateral directions and a domain size of $L_{x,\text{pre}} \times L_{y,\text{pre}} \times L_{z,\text{pre}} = 15.36 \times 9.6 \times 14.0 \text{ km}^3$.

The number of vertical grid points, the vertical grid stretching and Rayleigh damping levels are the same as in the main simulation. The initial horizontal velocity is set to the geostrophic wind $(U_g, V_g) = (9.011, -1.527) \text{ m s}^{-1}$, resulting in a steady-state hub height wind speed of $9.0 \pm 0.02 \text{ m s}^{-1}$ that is aligned with the x axis ($\pm 0.01^\circ$). The values for the geostrophic wind are obtained by iterative adjustments between preliminary precursor simulations, of which two are needed to obtain the given accuracy. The latitude is $\phi = 55^\circ \text{ N}$. The initial potential temperature is set to 280 K up to a height of 600 m and has a lapse rate of $\Gamma = +3.5 \text{ K km}^{-1}$ above. This lapse rate corresponds to the international standard atmosphere. The onset of turbulence is triggered by small random perturbations in the horizontal velocity field below a height of 300 m . A Dirichlet boundary condition is set for the surface temperature. Why a Dirichlet boundary condition is a good choice is explained in Maas and Raasch (2022). A constant surface heating rate of $\dot{\theta}_0 = +0.05 \text{ K h}^{-1}$ is applied, resulting in a Monin–Obukhov length of $L \approx -400 \text{ m}$, which is common value for convective boundary layers in the North Sea (Muñoz-Esparza et al., 2012). The resulting boundary layer height (height of maximum vertical potential temperature gradient) of $z_i = 600 \text{ m}$ is a small but still typical value for convective boundary layers over the North Sea (Maas and Raasch, 2022). Boundary layer growth is avoided by applying a large-scale subsidence that acts only on the potential temperature field. The subsidence velocity is zero at the surface and increases linearly to its maximum value at $z = 600 \text{ m}$ and is constant above. The maximum subsidence velocity is chosen in such a way that the temperature increase in the free atmosphere (FA) exactly matches the surface heating rate: $w_{\text{sub}} = \dot{\theta}_0 / \Gamma \approx 14.3 \text{ m h}^{-1}$. The roughness length for momentum and heat is $z_0 = z_{0,h} = 1 \text{ mm}$, and a constant flux layer is assumed between the surface and the lowest atmospheric grid level. At the domain top and bottom, a Neumann boundary condition for the perturbation pressure and Dirichlet boundary conditions for the velocity components are used. For the potential temperature, a constant lapse rate is assumed at the domain top.

The physical simulation time of the precursor simulation is 48 h, to obtain a steady-state mean flow; i.e., the hourly-averaged hub height wind speed changes less than 0.05 m s^{-1} within 8 h. This long simulation time is needed for the decay of an inertial oscillation in time that has a period of 14.6 h. The inertial oscillation occurs because there is no equilibrium of forces in the boundary layer (BL) at the beginning of the simulation.

3 Results

3.1 Mean flow at hub height

To make a first qualitative comparison between the small and the large wind farm case, the mean horizontal wind speed and streamlines of the mean flow at hub height are shown in Fig. 2 for both cases. The most striking difference is the large modification of the wind direction that occurs for the large wind farm case. Inside the large wind farm the flow is deflected counterclockwise, but in the wake the flow is deflected clockwise so that the wind direction reaches the inflow wind direction and even turns further clockwise. But also for the wind speed both cases show significant differences. The wind speed reduction inside the large wind farm is significantly greater than inside the small wind farm, which is an expected result. Remarkable, however, is the fact that the wind speed in the far wake of the large wind farm is significantly greater than the inflow wind speed.

To make a more quantitative comparison between the two cases, Fig. 3 shows the mean horizontal wind speed, wind direction and perturbation pressure at hub height along x for the small and large wind farm. The quantities are averaged along y and a moving average with a window size of one turbine spacing is applied along x to smooth out turbine-related sharp gradients. It can be seen that upstream of the wind farms the wind speed is reduced due to the blockage effect. The speed reduction $2.5 D$ upstream of the first turbine row is 4.8 % for the small wind farm and 7.9 % for the large wind farm. These values lie in the range of 1 %–11 %, reported by Wu and Porté-Agel (2017) for a 20 km long wind farm under different FA stratifications. The blockage effect is caused by an increase in the perturbation pressure of 4.8 and 8.5 Pa relative to the pressure at the inflow for the small and large wind farm, respectively (see Fig. 3c). The perturbation pressure distribution is related to gravity waves that form in the free atmosphere, as will be shown in Sect. 3.4. Inside the wind farm, the wind speed is further reduced due to momentum extraction by the wind turbines. For the small wind farm, the wind speed decreases to 7.6 m s^{-1} at the wind farm trailing edge (TE). For the large wind farm, however, the wind speed reaches a minimum of 6.8 m s^{-1} approximately 40 km downstream of the leading edge (LE) and then increases again to 7.4 m s^{-1} at the wind farm TE. This acceleration is mainly caused by the large drop in the perturbation pressure of 30 Pa from the wind farm LE to TE. For the small wind farm this

pressure drop is only approximately 7 Pa. The acceleration is also caused by the wind direction change and thus a greater ageostrophic wind speed component that results in a larger energy input by the geostrophic pressure gradient (Abkar and Porté-Agel, 2014). This will be shown in Sect. 3.5. In the wake of the large wind farm the wind speed increases further and reaches a maximum of 10.1 m s^{-1} , which is 12 % more than the free-stream wind speed at the inflow. The maximum wind speed in the wake of the small wind farm exceeds the inflow wind speed by only 2 %. Further downstream the wind speed decreases again, indicating that it oscillates.

As shown in Fig. 3b, the wind direction is also significantly affected by the wind farms. Inside the wind farms the wind direction turns counterclockwise, reaching $+2.3$ and $+10.1^\circ$ at the TE of the small and large wind farm, respectively. Note that the wind direction already changes upstream of the wind farms, reaching $+0.7$ and $+1.4^\circ$ at the LE of the small and large wind farm, respectively. This wind direction change is caused by a reduction of the Coriolis force, which is a result of the reduced wind speed in and around the wind farms. For the large wind farm, the maximum deflection angle of 10.4° is reached inside the wind farm, at $x \approx 180 \text{ km}$. Further downstream the wind turns clockwise, reaches $\Psi = 0^\circ$ at $x \approx 330 \text{ km}$ and turns further clockwise afterwards. For the small wind farm the maximum deflection angle of 2.8° is reached in the wake, at $x \approx 140 \text{ km}$. The wind direction is zero at $x \approx 290 \text{ km}$ and reaches a minimum at $x \approx 400 \text{ km}$. Similar maximum deflection values of 2–3° have been reported in an LES study of Allaerts and Meyers (2016) for a 15 km long wind farm in conventionally neutral boundary layers.

The sinusoidal shape of the wind speed and wind direction evolution suggests that it is related to an inertial oscillation or an inertial wave along x . The wind direction has a $+90^\circ$ phase shift relative to the wind speed; i.e., the wind direction is zero where the wind speed has a maximum. The inertial wave has a wavelength of

$$\lambda_I \approx GT = 9.14 \text{ m s}^{-1} 14.6 \text{ h} \approx 480 \text{ km}, \quad (6)$$

where G is the geostrophic wind speed and $T = 12 \text{ h} / \sin(\phi) = 2\pi / f_3$ is the inertial period (Stull, 1988, p. 639). Consequently, the distance between wind direction maximum and minimum should be half a wavelength ($\lambda_I/2 = 240 \text{ km}$), which corresponds well to the distance of 260 km that can be measured in the wake of the small wind farm. To add further confidence to this result, an additional simulation with a latitude of 80° N instead of 55° N is performed. The results are given in Appendix B and show that the wavelength decreases to $\lambda_I = 400 \text{ km}$ due to the shorter inertial period at that latitude ($T = 12 \text{ h} / \sin(80^\circ) = 12.1 \text{ h}$).

The inertial wave can also be seen in the hodograph of the hub height wind velocity components u and v along x , which is shown in Fig. 4. The figure shows that the oscillation is triggered by a reduction in u , followed by an increase

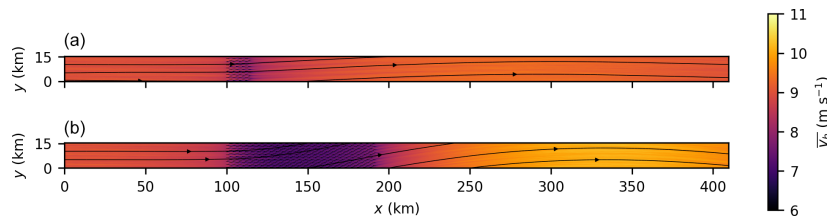


Figure 2. Mean horizontal wind speed at hub height for the small wind farm (a) and large wind farm (b). Wind direction is indicated by streamlines.

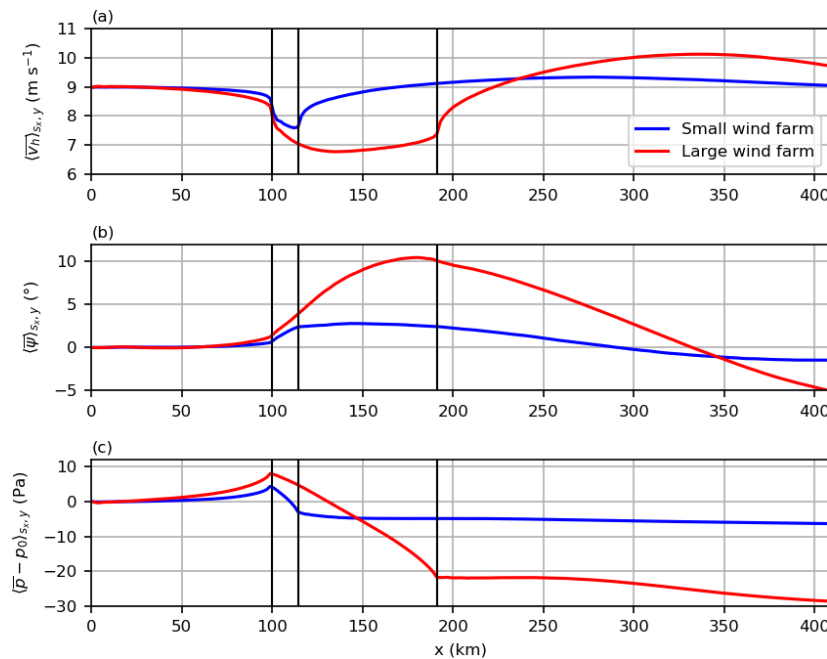


Figure 3. Horizontal wind speed (a), wind direction (b) and perturbation pressure (c) along x . All quantities are averaged along y and one turbine spacing along x . Vertical black lines indicate LE and TE of the small and large wind farm.

in v . After the large perturbation by the wind farms, the hodograph approaches a circular path with clockwise direction. The center of these circular paths is the steady-state velocity of the inflow and not the geostrophic wind velocity. This is consistent with the findings of Baas et al. (2012), who investigated inertial oscillations in the nocturnal BL using the analytical model of van de Wiel et al. (2010) that accounts for frictional effects within the BL. The amplitude of the oscillations is 0.3 m s^{-1} for the small wind farm and 1.1 m s^{-1} for the large wind farm at $\lambda_l/4$ downstream of the respective wind farm trailing edge.

To investigate this effect in more detail, Fig. 5 shows the crosswise (perpendicular to streamlines) force components that act on the flow at hub height along x , averaged along y . Shown are the vertical turbulent momentum flux divergence, the perturbation pressure gradient force and the geostrophic

forcing (difference between geostrophic pressure gradient force and Coriolis force). Positive values indicate a counterclockwise deflection, and negative values indicate a clockwise deflection. The analysis is made from a Lagrangian frame of reference; thus, advection terms are not included. At the inflow all forces sum to zero and the mean flow is in a steady state. Due to the wind speed reduction upstream and inside the wind farms, the Coriolis force is reduced, so that the geostrophic pressure gradient force predominates and tends to deflect the flow counterclockwise. The vertical momentum flux divergence, however, tends to deflect the flow clockwise, but this force is weaker, so that the sum of these forces is still positive. Because the wind farms are infinite in the y direction, the gravity waves are uniform in the y direction, and thus the perturbation pressure gradient force is parallel to the x axis and has no effect on the wind direc-

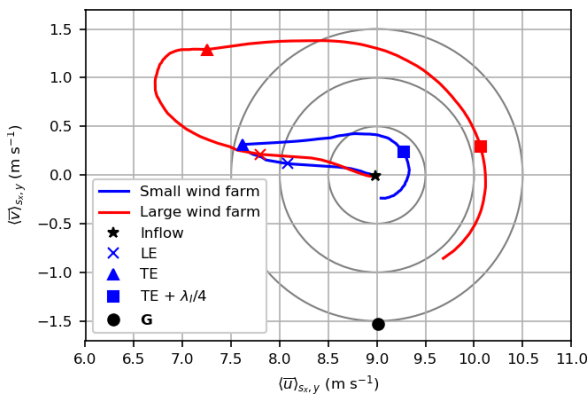


Figure 4. Hodographs of wind speed components u and v along x at hub height. Special streamwise positions are marked: inflow, wind farm leading edge (LE), wind farm trailing edge (TE), one-quarter inertial wavelength downstream of the TE and the geostrophic wind velocity.

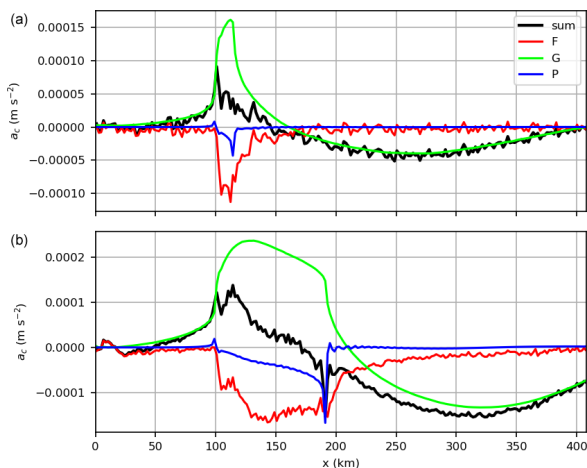


Figure 5. Crosswise forces (perpendicular to streamlines) at hub height along x , averaged along y for the small wind farm (a) and large wind farm (b). Shown are the divergence of the vertical turbulent momentum flux (resolved + SGS) F , the geostrophic forcing G (difference between geostrophic pressure gradient force and Coriolis force) and the perturbation pressure gradient force P .

tion at first. However, due to the change in wind direction further downstream inside the large wind farm, the perturbation pressure gradient force has a component perpendicular to the streamlines that tends to deflect the flow clockwise. At the end of the large wind farm the sum of all forces becomes negative, so that the flow begins to turn clockwise. Because the wind speed increases to super-geostrophic values in the wake, the Coriolis force becomes greater than the geostrophic pressure gradient force so that the flow is deflected clockwise. The most significant difference between

the small and the large wind farm is that the speed deficit in the large wind farm is greater and lasts longer. This results in a greater wind direction change and thus a greater inertial wave amplitude compared to the small wind farm. Whether a wind farm can trigger a significant inertial wave can be predicted by the Rossby number that relates inertia to Coriolis forces:

$$Ro = \frac{G}{L_{wf} f_3}, \quad (7)$$

where L_{wf} is the length of the wind farm. An inertial wave occurs if the Rossby number has the order of magnitude of 1 or smaller. Coriolis effects become more dominant for smaller Rossby numbers so that the amplitude of the inertial wave is larger for the large wind farm ($Ro = 0.8$) than for the small wind farm ($Ro = 5.0$). That wind farms can trigger an inertial wave has not been reported by any other study, although there are studies that investigate wind farms with a similar size compared to the small wind farm in this study, e.g., Allaerts and Meyers (2016) or Wu and Porté-Agel (2017). The reason is that the inertial wave is more than 20 times longer than the small wind farm and is thus usually not covered by the numerical domain of other studies.

3.2 Turbulence at hub height

Figure 6 shows the total turbulence kinetic energy (TKE) and the turbulence intensity (TI) at hub height along x for the small and large wind farm case. Both quantities are averaged along y and piecewise averaged along x , where the averaging windows have a size of one turbine spacing and are centered between the turbine rows. The TKE and TI are calculated as follows:

$$TKE = \frac{1}{2}(\overline{u'^2} + \overline{v'^2} + \overline{w'^2}) + \bar{e}, \quad (8)$$

$$TI = \frac{\sqrt{\frac{2}{3}TKE}}{\bar{v}_h}, \quad (9)$$

where an overbar indicates a temporal average; a prime indicates the deviation from this average; $\overline{u'^2}$, $\overline{v'^2}$ and $\overline{w'^2}$ are resolved-scale variances; and \bar{e} is the SGS TKE. Upstream of the wind farms the ambient TKE is $0.22 \text{ m}^2 \text{ s}^{-2}$. Within four turbine rows the TKE reaches a plateau value of $0.85 \text{ m}^2 \text{ s}^{-2}$ for the small wind farm and $0.80 \text{ m}^2 \text{ s}^{-2}$ for the large wind farm. The TKE is greater in the small wind farm because the wind speed is greater, and thus the turbines generate more TKE (see Fig. 3a). In the large wind farm the TKE decreases slightly to $0.76 \text{ m}^2 \text{ s}^{-2}$ at the point where the minimum wind speed occurs. Further downstream the TKE increases to its maximum value of $0.85 \text{ m}^2 \text{ s}^{-2}$ at the TE.

The TI shows a slightly different behavior than the TKE. Due to the normalization by the wind speed, which decreases upstream of the wind farms, the TI increases upstream of the wind farms. It increases from the ambient TI of 4.4 %

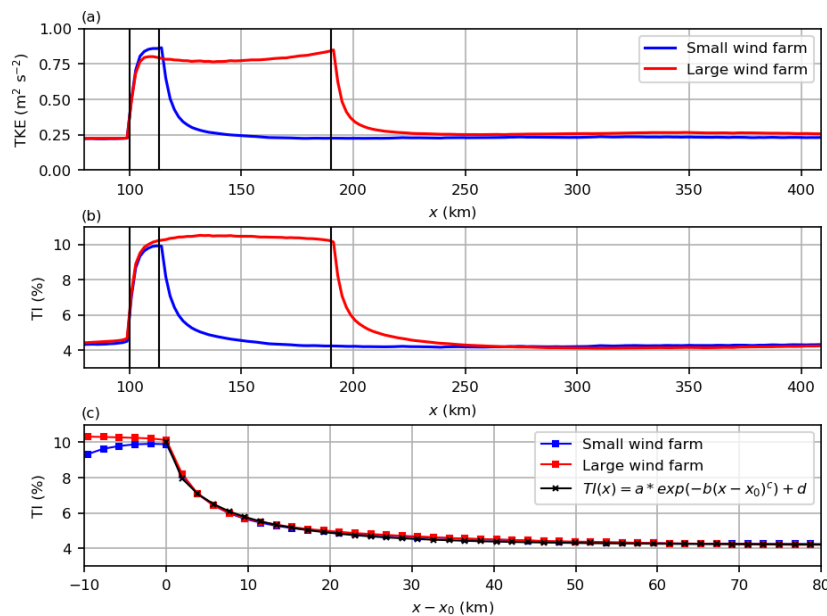


Figure 6. (a) Turbulence kinetic energy (TKE) and (b, c) turbulence intensity (TI) for the small and large wind farm case. The quantities are averaged along y and piecewise along x , with averaging windows centered between the turbine rows. Vertical black lines indicate the wind farm LE and TE of the small and large wind farm. In panel (c) the graphs are shifted by x_0 so that the TE of the small and the large wind farm coincide, where $x_0 = x_{TE} + 0.5$ s. Parameters of the fitted curve are $a = 5.8\%$, $b = 0.28 \text{ km}^{-c}$, $c = 0.68$ and $d = 4.2\%$.

to 4.6% half a turbine spacing upstream of the LE. In the small wind farm, the TI reaches a plateau value of 9.9%. In the large wind farm the TI is greater due to the smaller wind speed and reaches a maximum value of 10.5% at the point where the minimum wind speed occurs. Further downstream, the TI decreases and reaches 10.1% at the TE.

To compare the decay of the TI in the wake of the wind farms, the graphs in Fig. 6c are shifted so that the TEs of both wind farms coincide. It is remarkable that the decay of the TI in the wake of the small and the large wind farm follows exactly the same curve. This curve can be approximated by the following exponential function:

$$TI(x) = a \exp(-b(x - x_0)^c) + d, \quad (10)$$

with coefficients $a = 5.8\%$, $b = 0.28 \text{ km}^{-c}$, $c = 0.68$ and $d = 4.2\%$. Consequently, the wind farm size has no effect on the decay of the TI in wind farm wakes.

Further downstream, the TKE and the TI also show a slight oscillation as the wind speed and direction show (see Fig. 6a and b). However, the amplitude is much smaller than the TKE and TI levels that occur inside the wind farms, and thus the oscillations are hardly visible.

3.3 Boundary layer modification

The previous two sections focused on the flow at hub height. In this section it is shown how the wind farms modify the height and the internal structure of the BL.

The CBL is capped by an inversion layer (IL), which is displaced upwards due to the presence of the wind farms. The IL displacement δ is defined as the IL height z_i relative to the IL height at the inflow:

$$\delta(x) = z_i(x) - z_i(x = 0), \quad (11)$$

where z_i is defined as the height where the maximum vertical potential temperature gradient occurs. The IL displacement along x is shown in Fig. 7 for the small and large wind farm case. The IL displacement begins already upstream of the wind farms and reaches +30 and +50 m at the LE of the small and large wind farm, respectively. Note that these changes in IL height (+5% and +8%) correspond well to the change in hub height wind speed (−5% and −8%; see Fig. 3) at the LE. This confirms that the IL displacement is a reaction of the flow to the speed reduction inside the boundary layer that ensures a constant mass flux inside the boundary layer. This has also been stated by other studies (Allaerts and Meyers, 2017; Maas and Raasch, 2022).

The maximum displacement is +55 m for the small wind farm and occurs near its TE. For the large wind farm the maximum displacement is +110 m and occurs approximately

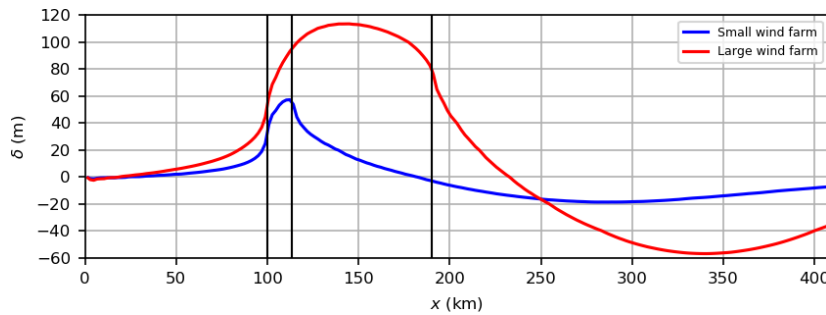


Figure 7. Inversion layer displacement δ . Vertical black lines indicate LE and TE of the small and large wind farm.

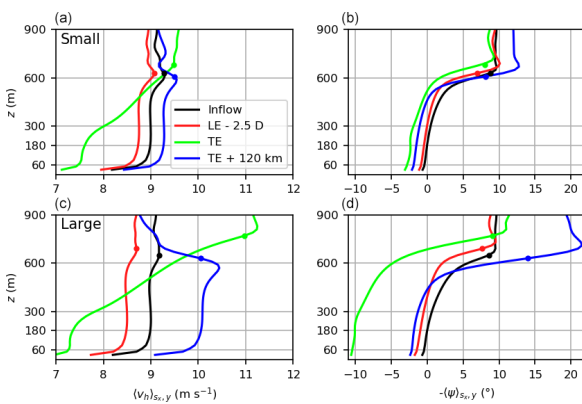


Figure 8. Vertical profiles of the horizontal wind speed (a, c) and the wind direction (b, d) for the small wind farm (a, b) and the large wind farm (c, d). The profiles are averaged in time, along y and over one turbine spacing along x . Horizontal lines are shown at $z = 60$ m (rotor bottom), $z = 180$ m (hub height), $z = 300$ m (rotor top) and $z = z_j = 600$ m (BL height at the inflow). Dots mark the BL height at the respective x location.

40 km downstream of the LE. Thus, the maximum displacements occur at the location of the minimum wind speed (see Fig. 3). In the wake of the wind farms the IL displacement becomes negative, due to the increasing wind speed inside the boundary layer. For the small wind farm, the minimum displacement is $\delta \approx -20$ m and occurs at $x \approx 290$ km, corresponding to the location at which the hub height wind speed has a maximum and the wind direction is zero. The same holds for the large wind farm, except that the minimum displacement is $\delta \approx -55$ m and occurs at $x \approx 330$ km.

Besides the top of the BL, the internal structure of the BL is also significantly modified by the wind farms. Figure 8 shows vertical profiles of the wind speed and direction at several streamwise positions to demonstrate the development of the BL. As a reference, the inflow profiles are also shown. The second profile is located $2.5 D$ upstream of the wind farm LEs. It shows that the speed deficit, caused by the block-

age effect, does not only occur at hub height but is rather constant over the entire BL. This is plausible because the speed reduction is caused by a positive streamwise pressure gradient, which is approximately constant over the entire height of the BL. At the wind farm TE, the wind speed at hub height is significantly reduced. At the BL top, however, the wind speed has increased from 9.0 to 9.6 m s^{-1} for the small wind farm and from 8.6 to 11.0 m s^{-1} for the large wind farm. Because turbulent momentum exchange is negligible at that height, these speed differences are solely caused by a drop in the perturbation pressure. The drop in the perturbation pressure between these points is 7 Pa for the small wind farm and 28 Pa for the large wind farm (see Fig. 3). Based on these pressure differences, Bernoulli's equation predicts these wind speed changes:

$$\begin{aligned}
 v_2 &= \sqrt{\frac{2}{\rho}(p_1 - p_2) + u_1^2} \\
 &= \sqrt{\frac{2}{1.17 \text{ kg m}^{-3}} 7 \text{ Pa} + (9.0 \text{ m s}^{-1})^2} = 9.6 \text{ m s}^{-1} \\
 &\text{(small wind farm)} \\
 &= \sqrt{\frac{2}{1.17 \text{ kg m}^{-3}} 28 \text{ Pa} + (8.6 \text{ m s}^{-1})^2} = 11.0 \text{ m s}^{-1} \\
 &\text{(large wind farm),} \tag{12}
 \end{aligned}$$

which correspond to the observed wind speed changes. The pressure distribution in the BL is determined by gravity waves in the free atmosphere that are described in the next section. In the far wake, one-quarter of the inertial wavelength ($\lambda_I/4 = 120$ km) downstream of the wind farm TEs, the wind speed in the bulk of the BL is supergeostrophic. At 300 m height the wind speed has increased to 9.2 and 10.1 m s^{-1} for the small and large wind farm, respectively.

The wind direction profiles of the small wind farm case show only small deviations of maximum $\pm 3^\circ$ relative to the inflow profile. For the large wind farm case, however, the deviations can be as large as $\pm 10^\circ$. Because the profiles of the

small and large wind farm case are qualitatively the same, only the large wind farm case is described in the following. At a distance of $2.5 D$ upstream of the large wind farm, the wind direction has turned to the left by 1.4° at hub height and by 3.2° near the BL top. At the TE the wind direction has turned to the left by 10.0° up to a height of ≈ 600 m. At the BL top the wind direction change is zero. One-quarter inertial wavelength downstream of the TE, the shape of the wind direction profile is nearly unchanged, but the wind direction has turned back to the right by approximately 8° relative to the profile at the TE. This also holds for the wind direction above the BL, indicating that there is also an inertial wave in the free atmosphere. This effect will be investigated in the next section.

3.4 Gravity waves

The displacement of the IL represents an obstacle for the flow in the overlying stably stratified free atmosphere and thus triggers atmospheric gravity waves. The gravity waves are investigated in more detail in this section because they induce streamwise pressure gradients at the surface and thus also affect the flow inside the BL and the energy budgets in the wind farms. Due to the large horizontal scales involved, Coriolis effects also affect the flow, so that the triggered gravity waves are not pure gravity waves but rather inertial gravity waves.

Figure 9 shows vertical cross sections of the horizontal wind speed and direction, the vertical wind speed, the perturbation pressure, and the potential temperature. The respective inflow profile is subtracted from each quantity, so that only the deviations from the steady-state mean flow remain. All quantities are averaged in time and along y . The different quantities show the expected pattern for stationary inertial gravity waves with upwards propagating energy; i.e., the phase lines are inclined upstream relative to the vertical. The phase relations between the quantities also correspond to the expected relations for gravity waves; e.g., p and w are in phase and w and θ are 90° out of phase (Durrant, 1990, Fig. 4.1).

The shown wave fields are a superposition of waves with three different inclination angles α (see Table 1). The first type of waves occurs above the wind farm LE and TE and is only visible in the vertical velocity field (see Fig. 9e and f). The phase lines are inclined by $\alpha_1 = 60^\circ$ relative to the vertical. They are only visible in the vertical velocity field because the oscillation direction is much more vertical than that of the other wave types. The second type of waves appears above the wind farm with phase lines inclined by $\alpha_{2s} = 83.7^\circ$ and $\alpha_{2l} = 88.3^\circ$ for the small and large wind farm, respectively. The third type of waves occurs above the wake and has phase lines that are inclined by $\alpha_3 = 89.3^\circ$ (see dashed lines in Fig. 9a and b). The occurrence of these three different wave types can be explained by the shape of the topography, which is in this case the inversion layer. The wave

type one is triggered by the sharp increase and decrease in IL height at the wind farm LE and TE (see Fig. 7). Wave types two and three, however, are triggered by the entire hill-like-shaped IL above the wind farm and the valley-like-shaped IL above the wake. The phase lines of wave type two are not perfectly straight but have a slightly positive curvature. The reason might be that the shape of the IL above the wind farm is not sinusoidal but is rather flat. The curved phase lines may also explain why the pressure distribution in the wind farm is not sinusoidal (as one could expect) but nearly linear (which is also true in the FA above the wind farm).

The amplitude of wave type one is approximately the same for the small and large wind farm case, while the amplitudes of wave types two and three are approximately 2 times greater for the large wind farm case relative to the small wind farm case (see Fig. 9 and note the different color scale ranges). The reason is that the IL displacement is twice as large for the large wind farm than for the small wind farm (see Fig. 7).

The wavelengths of the three different wave types are significantly different. For stationary waves, the horizontal wavelength can be calculated as the distance that an air parcel moves with the background velocity $U = U_g$ during one oscillation period with oscillation frequency ω :

$$\lambda_x = \frac{2\pi U}{\omega}. \quad (13)$$

The oscillation frequency ω of an inertial gravity wave is given by the dispersion relation (Pedlosky, 2003, Eq. 11.33):

$$\omega = \sqrt{f^2 \sin^2 \alpha + N^2 \cos^2 \alpha}, \quad (14)$$

where $N = \sqrt{\frac{g}{\theta_0}} \Gamma = 10.7 \times 10^{-3} \text{ s}^{-1}$ is the Brunt-Väisälä frequency. Note that the oscillation frequency is higher than for pure gravity waves because the Coriolis force acts as an additional restoring force. Equation (14) reduces to $\omega = N$ for pure vertical oscillating gravity waves (vertical phase lines) and to $\omega = f$ for pure horizontal oscillating inertial waves (horizontal phase lines). The absolute wavelength λ , i.e., the wavelength in the direction of phase propagation, is then given by

$$\lambda = \frac{2\pi c}{\omega} = \frac{2\pi U \cos \alpha}{\sqrt{f^2 \sin^2 \alpha + N^2 \cos^2 \alpha}} = \frac{1}{\sqrt{1 + \frac{f^2 \sin^2 \alpha}{N^2 \cos^2 \alpha}}} \frac{2\pi U}{N}, \quad (15)$$

so that the absolute wavelength becomes smaller for a larger α . Note that for pure gravity waves, where the effect of f can be neglected, the absolute wavelength is independent of α and corresponds to the Scorer length $L_s = 2\pi U/N = 5.3$ km. The vertical wavelength is given by

$$\lambda_z = \frac{\lambda}{\sin \alpha}. \quad (16)$$

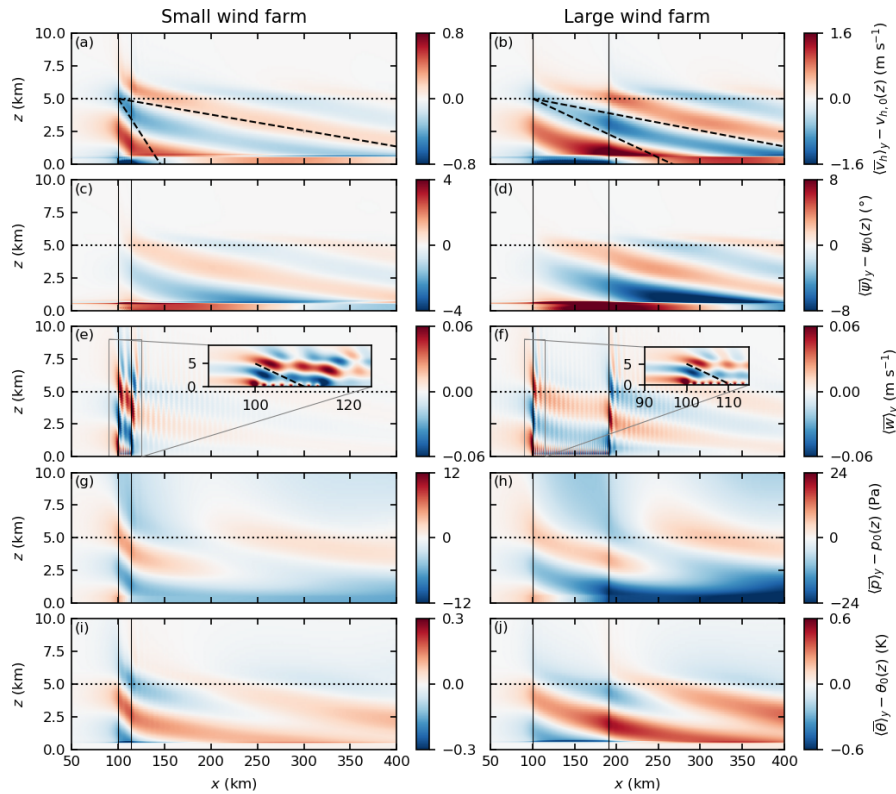


Figure 9. Vertical cross sections of the horizontal wind speed (a, b), wind direction (c, d), vertical wind speed (e, f), perturbation pressure (g, h) and potential temperature (i, j). The quantities are averaged in time and along y and the respective mean inflow is subtracted. Vertical lines mark the leading and trailing edge of the small (left) and large (right) wind farm. The bottom of the Rayleigh-damping layer is marked by a dotted line. Dashed lines indicate the inclination angles of the phase lines. The gravity waves at the leading edges are shown in detail in panels (e) and (f). Note that the range of the color scale is only half as large for the small wind farm than for the large wind farm except for w.

Table 1. Inclination angle of phase lines α and corresponding wavelengths for the different wave types present in Fig. 9.

Wave type	α °	λ km	λ_x km	λ_z km	λ_x/L_{wf} –	L_{wf}/L_S –
1 (LE + TE)	60	5.29	10.6	6.11	–	–
2 (small wind farm)	83.7	5.27	48.0	5.30	3.6	2.5
2 (large wind farm)	88.3	4.96	167.1	4.96	1.85	17.0
3 (wake)	89.3	3.91	320.3	3.91	–	–

The inclination angles of each wave type are measured in a figure that is similar to Fig. 9 but uses equal scales for both axes (not shown). The calculated oscillation frequencies and wavelengths of the three wave types are listed in Table 1.

The waves of type one have the smallest wavelength (10.6 km). Their effect on the pressure and horizontal velocity field is negligible. The horizontal wavelengths of wave type two are 48 and 167 km for the small and large wind farm, respectively. Why do these wavelengths occur? The ra-

tio of horizontal wavelength to the wind farm length is 3.6 for the small wind farm and 1.85 for the large wind farm, so that the wind farm length is not a good measure to explain the wavelength. But the wavelength can be explained by the shape of the IL. The horizontal distance between the largest slope of the IL (at the LE) and the location of the maximum displacement is 12 and 42 km for the small and large wind farm, respectively (see Fig. 7). These distances correspond very well to $\lambda_{x,2}/4$ of the waves above the wind farm.

546

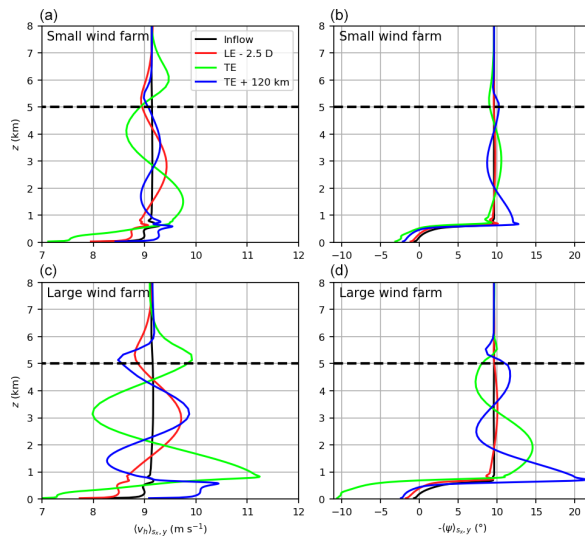


Figure 10. Vertical profiles of the horizontal wind speed (a, c) and the wind direction (b, d) for the small wind farm (a, b) and the large wind farm (c, d). The profiles are averaged in time, along y and over one turbine spacing along x . Horizontal dashed line indicates the bottom of the Rayleigh damping layer.

The presented results generally correspond very well to the results of Allaerts and Meyers (2017), who investigated gravity waves above a 15 km long wind farm, which approximately corresponds to the length of the small wind farm in this study. One significant difference between the studies is the larger extent of the large wind farm in this study, causing inertial gravity waves due to Coriolis effects that become dominant at that scale. The second significant difference is the weaker stratification of $+1.0 \text{ K km}^{-1}$ in their study compared to $+3.5 \text{ K km}^{-1}$ in this study. This leads to a different Brunt–Väisälä frequency and thus a different Scorer length (which corresponds to the absolute wavelength of stationary pure gravity waves). Consequently, the wind farm in Allaerts and Meyers (2017) has approximately the length of the Scorer length ($L_{\text{wf}}/L_s = 15 \text{ km}/12.8 \text{ km} \approx 1.2$), whereas the small wind farm and large wind farm in this study are $L_{\text{wf},s}/L_s = 13.44 \text{ km}/5.3 \text{ km} \approx 2.5$ and $L_{\text{wf},l}/L_s = 90.24 \text{ km}/5.3 \text{ km} \approx 17.0$ times longer than the Scorer length, respectively. Due to the large ratio of L_{wf}/L_s in the large wind farm case, the waves at the wind farm LE and TE (type one) are separated by several wavelengths and can thus be clearly distinguished from wave type two in this study. However, the less orderly shape of the w field in Allaerts and Meyers (2017) (their Fig. 12b) suggests that wave type one is also present there.

The vertical structure of the gravity waves is shown by profiles of the wind speed and wind direction at different streamwise positions in Fig. 10. It can be seen that the amplitude of the waves is approximately twice as large in the large wind

O. Maas: From gigawatt to multi-gigawatt wind farms

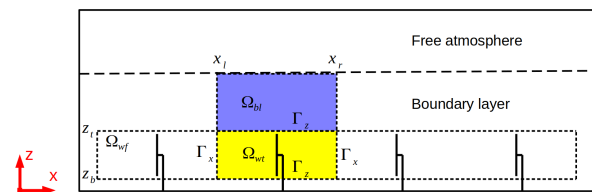


Figure 11. Sketch of wind turbine control volumes Ω_{wt} , BL control volumes Ω_{bl} and the wind farm control volume Ω_{wf} . In the x direction the control volumes are bounded by the surfaces Γ_x at $x = x_l$ and $x = x_r$. In the vertical direction, the control volumes are bounded by Γ_z at $z = z_b$ and $z = z_t$. In the y direction the control volumes are bounded by the cyclic domain boundaries. The control volumes are centered on the respective turbine hub.

farm case than in the small wind farm case, as already mentioned above. There is a phase shift of approximately 90° between the wind speed and wind direction. Inside the Rayleigh damping layer the wind speed variations decay within 3 km, and the wind direction variations decay within 1 km.

3.5 Energy budget analysis

Wind turbines extract kinetic energy from the BL flow and convert it into electrical energy. Consequently, there is less energy available for wind turbines located in the wake of upstream wind turbines. The energy extraction is considered by a velocity deficit zone in the wind turbine wake in classical wake models such as Jensen (1983). However, there are also sources of energy that add new kinetic energy into the BL. As will be shown in this section, these sources depend on the above-discussed flow effects and significantly affect the wind turbine power, especially for the large wind farm.

To analyze the different energy sources and sinks in the BL, an extensive energy budget analysis is presented in this section. The analysis is very similar to the energy budget analysis made by Allaerts and Meyers (2017) for a 15 km long wind farm. The energy budgets are calculated for three different control volumes. The control volume Ω_{wt} envelops the wind turbine rotor, the control volume Ω_{bl} envelops the rest of the BL above Ω_{wt} and the entire wind farm is enveloped by control volume Ω_{wf} , which is the sum of all Ω_{wt} (see Fig. 11). The control volumes have a streamwise length of one turbine spacing and are centered at the respective wind turbine hub. The bottom and top boundaries of Ω_{wt} are $(z_b, z_t) = (50, 310) \text{ m}$, which is $1d_z$ larger than the rotor diameter to cover the smeared forces of the wind turbine model. The bottom and top boundaries of Ω_{bl} are $(z_b, z_t) = (310 \text{ m}, z_i(x))$. In the y direction the control volumes are bounded by the cyclic domain boundaries.

The equation for the conservation of the resolved-scale kinetic energy can be obtained by multiplying PALM's momentum equation (Eq. 2) with u_i , averaging in time, assum-

ing stationarity and integrating over the control volume Ω :

$$\begin{aligned}
 0 = & - \underbrace{\int_{\Omega} \frac{\partial \bar{u}_j}{\partial x_j} \bar{E}_k}_{\mathcal{A}} d\Omega - \underbrace{\int_{\Omega} \frac{\bar{u}_i}{\rho_0} \frac{\partial \pi^*}{\partial x_i}}_{\mathcal{P}} d\Omega \\
 & - \int_{\Omega} \frac{\partial}{\partial x_j} \bar{u}_i \bar{u}'_i \bar{u}'_j d\Omega + \int_{\Omega} \frac{\partial}{\partial x_j} \bar{u}_i \tau_{ij} d\Omega \\
 & - \underbrace{\int_{\Omega} \frac{\partial}{\partial x_j} \frac{1}{2} \bar{u}'_j \bar{u}'_i \bar{u}'_i}_{\mathcal{F}} d\Omega - \int_{\Omega} \frac{\bar{u}'_i}{\rho_0} \frac{\partial \pi^*}{\partial x_i} d\Omega \\
 & + \underbrace{\int_{\Omega} (\bar{u}_2 f_3 u_{g,1} - \bar{u}_1 f_3 u_{g,2})}_{\mathcal{G}} d\Omega \\
 & + \underbrace{\int_{\Omega} \frac{g}{\theta_0} (\bar{\theta} - \theta_0) \bar{u}_3}_{\mathcal{B}} d\Omega \\
 & - \underbrace{\int_{\Omega} \tau_{ij} \frac{\partial \bar{u}_i}{\partial x_j}}_{\mathcal{D}} d\Omega - \mathcal{R} + \underbrace{\int_{\Omega} \bar{u}_i d_i}_{\mathcal{W}} d\Omega. \tag{17}
 \end{aligned}$$

Note that the mean kinetic energy (KE, \bar{E}_k) contains the kinetic energy of the mean flow (KEM) and the turbulence kinetic energy (TKE) of the resolved flow:

$$\bar{E}_k = \frac{1}{2} \overline{\bar{u}_i \bar{u}_i} = \frac{1}{2} \overline{\bar{u}_i} \bar{u}_i + \frac{1}{2} \overline{\bar{u}'_i \bar{u}'_i}. \tag{18}$$

The terms of Eq. (17) are categorized as follows:

- \mathcal{A} is the divergence of KE advection;
- \mathcal{P} is the energy input by mean perturbation pressure gradients;
- \mathcal{F} is the transport of KEM by resolved turbulent stresses (term 1), transport of KEM and TKE by SGS stresses (term 2), turbulent transport of resolved-scale TKE by velocity fluctuations (term 3), and turbulent transport of KE by perturbation pressure fluctuations (term 4);
- \mathcal{G} is the energy input by geostrophic forcing;
- \mathcal{B} is the energy input by buoyancy forces;
- \mathcal{D} is the dissipation by SGS model and residual \mathcal{R} ; and
- \mathcal{W} is the energy extraction by wind turbines.

Equation (17) has a positive residual \mathcal{R} because the magnitude of the calculated dissipation is underestimated, which has two reasons. First, the local velocity gradients are underestimated because they are calculated with central differences. Second, the fifth-order upwind advection scheme

of Wicker and Skamarock (2002) has numerical dissipation, suppressing the magnitude of the smallest eddies, for which the gradients and the dissipation are highest (Maronga et al., 2013). The residual is subtracted from the (negative) dissipation term \mathcal{D} to compensate for the underestimated magnitude of the calculated dissipation.

Instead of calculating terms \mathcal{A} and \mathcal{F} as a volume integral, they can also be calculated as a surface integral over the control volume surfaces (Gauss's theorem):

$$\begin{aligned}
 \mathcal{A} = & \left[\int_{\Gamma_x} (-\bar{u}_1 \bar{E}_k) d\Gamma_x \right]_{x_l}^{x_r} + \left[\int_{\Gamma_z} (-\bar{u}_3 \bar{E}_k) d\Gamma_z \right]_{z_b}^{z_t}, \tag{19} \\
 \mathcal{F} = & \left[\int_{\Gamma_x} \left(-\bar{u}_i \bar{u}'_i \bar{u}'_j + \bar{u}_i \tau_{ij} - \frac{1}{2} \bar{u}'_i \bar{u}'_i \bar{u}'_i - \frac{\bar{u}'_i \pi^*}{\rho_0} \right) d\Gamma_x \right]_{x_l}^{x_r} \\
 & + \left[\int_{\Gamma_z} \left(-\bar{u}_i \bar{u}'_i \bar{u}'_3 + \bar{u}_i \tau_{i3} - \frac{1}{2} \bar{u}'_3 \bar{u}'_i \bar{u}'_i - \frac{\bar{u}'_3 \pi^*}{\rho_0} \right) d\Gamma_z \right]_{z_b}^{z_t}, \tag{20}
 \end{aligned}$$

where \mathcal{A}_x and \mathcal{A}_z are the advection of KE through the left/right and bottom/top surfaces, respectively, and \mathcal{F}_x and \mathcal{F}_z are turbulent fluxes through the left/right and bottom/top surfaces, respectively.

3.5.1 Energy budgets for the entire small and large wind farm

The energy budgets for a control volume that envelops the entire small/large wind farm are shown in Fig. 12. The budget terms of Eq. (17) are converted from $\text{W}\rho^{-1}$ to MW per turbine to make them more meaningful. The air density is $\rho = 1.17 \text{ kg m}^{-3}$.

With 5.6 MW per turbine, the horizontal advection of kinetic energy (\mathcal{A}_x) is the greatest energy source for the small wind farm. For the large wind farm, however, this source is only as large as 0.9 MW per turbine. This large difference is mainly the result of the fact that the large wind farm is 6 times longer than the small one, so that the influx of KE at the wind farm LE is distributed over 6 times more turbine rows. Additionally, the wind speed at the TE of the large wind farm is larger than at the TE of the small wind farm, so that more KE leaves the wind farm control volume (see Figs. 3 and 13).

For both wind farms, approximately 40 % of \mathcal{A}_x leaves the wind farm control volume again through vertical advection \mathcal{A}_z . KE is leaving the top of the control volume by a mean positive w , which is the result of the turbine-induced flow deceleration and the requirement for mass flow conservation. This effect has also been described by Allaerts and Meyers (2017).

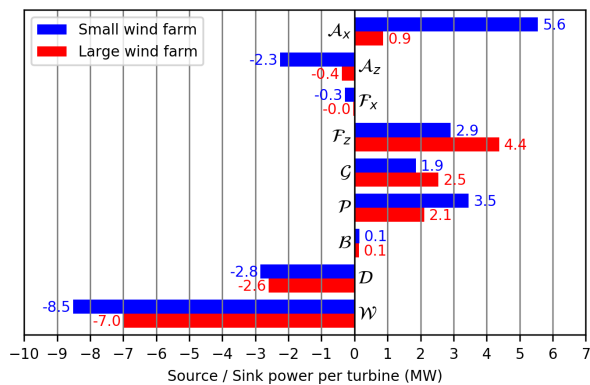


Figure 12. Energy budgets inside control volume Ω_{wf} that envelops the entire small/large wind farm. The budget terms are horizontal advection of KE (A_x), vertical advection of KE (A_z), turbulent fluxes through left/right (F_x) and bottom/top (F_z) surfaces, geostrophic forcing (G), perturbation pressure gradients (P), buoyancy (B), dissipation (D), and wind turbines (W).

The horizontal turbulent fluxes F_x are a small energy sink of -0.3 MW per turbine for the small wind farm. This sink is mainly caused by a net outflow of TKE in the first three turbine rows, where the incoming flow contains less TKE than the outgoing flow (see Figs. 6a and 13). For the large wind farm F_x is negligible because the described effect spreads over 6 times more turbine rows.

The vertical turbulent flux of KE (F_z) is the greatest energy source for the large wind farm, contributing 4.4 MW per turbine. For the small wind farm it is the third largest energy source with 2.9 MW per turbine. These results show that for large wind farms the vertical turbulent flux of KE is much more important than the horizontal advection ($F_z \approx 5 \times A_x$), whereas for small wind farms the horizontal advection of KE is more important ($A_x \approx 2 \times F_z$).

The energy input by the geostrophic forcing (G) is the fourth largest energy source for the small wind farm (1.9 MW per turbine) but the second largest energy source for the large wind farm (2.5 MW per turbine). The 32% higher value for the large wind farm is the result of the wind direction change that is triggered by the wind farm itself (see Fig. 3). It causes the ageostrophic wind velocity component to rise and thus leads to a higher energy input (see also Figs. 13 and 14). This effect has also been shown for infinitely large wind farms by Abkar and Porté-Agel (2014) and finite, large wind farms by Maas and Raasch (2022).

The energy input by the mean perturbation pressure gradient (P) is the second largest energy source for the small wind farm (3.5 MW per turbine) and the third largest energy source for the large wind farm (2.1 MW per turbine). For the large wind farm P is approximately 60% of P for the small wind farm, although the difference in perturbation pressure between the LE and TE of the large wind farm is approx-

imately 4.3 times larger than that of the small wind farm (30 Pa/7 Pa; see Fig. 3). However, this difference spreads over a 6 times longer wind farm, so that the resulting pressure gradient is only 70% as large. The term P also depends on the mean wind speed, which is generally smaller in the large wind farm, resulting in a further reduction of P .

The production of KE by buoyancy (B) is negligibly small for the small and large wind farm case. This is an expected result for the offshore-typical weakly unstable CBL with $L \approx -400$ m. However, this term might be much larger for strong CBLs.

The total of all above named sources ($A + F + G + P + B$) is 11.3 MW per turbine for the small wind farm and 9.6 MW per turbine for the large wind farm. For the small wind farm 75% of this available power is used by the wind turbines ($W = -8.5$ MW per turbine), and for the large wind farm it is 73% ($W = -7.0$ MW per turbine). The rest of the available energy is lost by dissipation (D).

3.5.2 Energy budgets in the turbine control volumes

The energy budgets inside the wind turbine control volumes Ω_{wt} are shown in Fig. 13. In the first two turbine rows the horizontal advection of KE (A_x) is the dominant energy source. A large amount of this KE, however, is lost by vertical advection of KE through the control volume top. This effect is caused by the fact that any horizontal convergence (flow deceleration with positive A_x) requires a vertical divergence (negative A_z) so that the mass flux is conserved. Consequently, the shape of A_z is qualitatively the vertically mirrored shape of A_x . At row 21 of the large wind farm the terms change sign because from there on the flow accelerates again (see Fig. 3). For the small wind farm this happens between the last two rows. From there on, more KE leaves the control volume than KE enters the control volume in the streamwise direction. But A_z is then positive, indicating that KE is transported into the wind farm from above by a negative mean vertical velocity. The flow acceleration at the end of the wind farms is mainly caused by the negative perturbation pressure gradient that has the highest magnitude at the wind farm TE (see Fig. 3). The energy input by the pressure gradient P thus increases towards the TE of the large wind farm and reaches 5 MW per turbine at the TE. The pressure distribution inside the wind farm is determined by wave type two of the gravity waves (see Sect. 3.4 and Fig. 9). The flow acceleration near the TE of the wind farm and the related negative net advection of KE have also been reported by Al-laerts and Meyers (2017) for a 15 km long wind farm in a conventionally neutral BL.

The horizontal turbulent fluxes are a weak energy sink (≈ -1 MW per turbine) in the first two rows because the outgoing flow contains more TKE than the incoming flow.

For both wind farms the vertical turbulent fluxes are zero at the first row. For the small wind farm they rise from 3 MW in the middle of the wind farm to 4 MW at the TE. For the

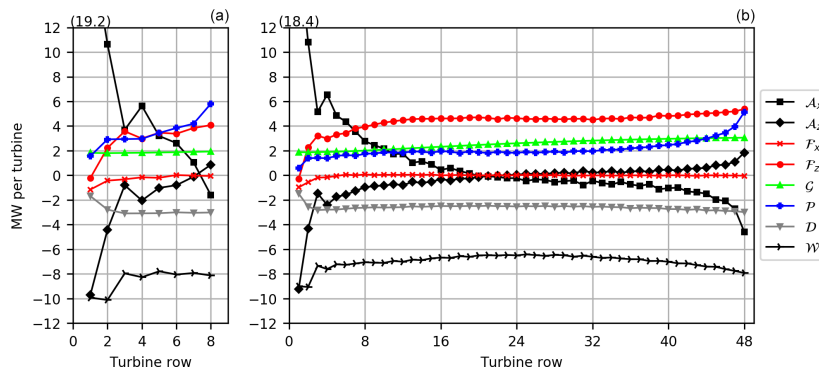


Figure 13. Energy budgets inside the wind turbine control volumes Ω_{wt} for the small wind farm (a) and the large wind farm (b). The budget terms are horizontal advection of KE (\mathcal{A}_x), vertical advection of KE (\mathcal{A}_z), turbulent fluxes through left/right (\mathcal{F}_x) and bottom/top (\mathcal{F}_z) surfaces, geostrophic forcing (\mathcal{G}), perturbation pressure gradients (\mathcal{P}), dissipation (\mathcal{D}), and wind turbines (\mathcal{W}). The buoyancy term (\mathcal{B}) is not shown because it is very small.

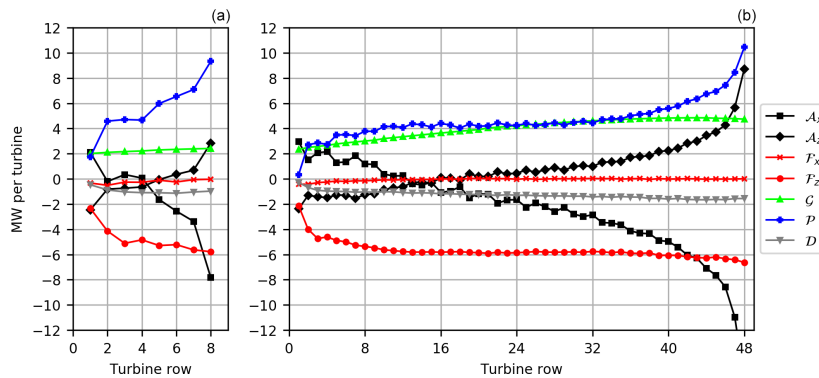


Figure 14. Energy budgets inside the BL control volumes Ω_{bl} for the small wind farm (a) and the large wind farm (b). The budget terms are horizontal advection of KE (\mathcal{A}_x), vertical advection of KE (\mathcal{A}_z), turbulent fluxes through left/right (\mathcal{F}_x) and bottom/top (\mathcal{F}_z) surfaces, geostrophic forcing (\mathcal{G}), perturbation pressure gradients (\mathcal{P}), and dissipation (\mathcal{D}). The buoyancy term (\mathcal{B}) is not shown because it is very small. There is no energy extraction by wind turbines (\mathcal{W}) in the BL control volume.

large wind farm they stay constantly at 4.5 MW per turbine from approximately row 14, but from row 32 they start to rise again, reaching 5.5 MW per turbine at the TE. The values of \mathcal{F}_z are generally greater for the large wind farm because there is more energy available in the upper part of the BL, which is mainly the result of the higher energy input by the geostrophic forcing for the large wind farm (see Fig. 14). From row 7 to the TE of the large wind farm the vertical turbulent fluxes are the greatest energy source of all terms.

For the small wind farm, the energy input by the geostrophic forcing is approximately constant at 2 MW per turbine. For the large wind farm, however, it steadily rises from 2 MW per turbine at the LE to 3 MW per turbine at the TE. As described in the last section, this effect is caused by the wind direction change along the wind farm that leads to a higher ageostrophic wind velocity component.

The wind turbines in the first two rows of the small and large wind farm extract approximately 10.0 and 9.0 MW, respectively (remember the staggered turbine configuration). The wind turbine power is constant at 8.0 MW in the rest of the small wind farm. In the large wind farm, however, the turbine power slowly decreases to 6.5 MW at row 24 and then increases to nearly 8.0 MW at the last turbine row. This power increase is the result of the wind speed increase in the second half of the wind farm that is related to the wind direction change and increase in \mathcal{G} .

The energy dissipation is approximately constant at $\mathcal{D} = -3$ MW per turbine in the small wind farm and at $\mathcal{D} = -2.5$ MW in the large wind farm, except for the first 3 rows, where it is smaller. At the TE of the large wind farm \mathcal{D} is slightly higher than in the middle, which can be related to the higher TKE at that location (see Fig. 6).

3.5.3 Energy budgets in the boundary layer control volumes

In the BL control volumes above the wind turbines the flow begins to accelerate earlier than inside the wind farm (row 4 of the small wind farm and row 14 of the large wind farm), as indicated by the evolution of \mathcal{A}_x (see Fig. 14). The energy for this acceleration is provided by \mathcal{G} and \mathcal{P} in approximately equal parts (4 MW per turbine) in the large wind farm, except towards the TE, where \mathcal{P} increases steeply due to a significant drop on perturbation pressure (see Fig. 3). For the small wind farm \mathcal{P} is 2 to 4 times larger than \mathcal{G} , except at the first row, where they are equal.

In the small wind farm \mathcal{G} increases by only 10 % from LE to TE, but in the large wind farm it increases by more than 100 % (from 2.2 to 4.8 MW per turbine). This is a much larger increase than in the wind turbine control volume, although the wind direction change is the same at all heights (see Fig. 8). However, the wind speed is much greater above the wind farm, resulting in a higher ageostrophic wind velocity component and thus a higher \mathcal{G} .

The vertical turbulent fluxes \mathcal{F}_z have the same shape as but opposite sign to the turbine control volumes (see Fig. 13) because they transfer energy from the BL down into the wind farm. Their magnitude is approximately 25 % smaller in the turbine control volume than in the BL control volume because there is also a KE loss through the bottom of the turbine control volumes.

4 Conclusions

The aim of this LES study is to provide a systematic comparison between small and large wind farms, focusing on the flow effects and the energy budgets in and around the wind farms. The size of the wind farms is chosen to be representative for current wind farm clusters (length of approximately 15 km) and future wind farm clusters (length of approximately 90 km).

The results show that there are significant differences in the flow field and the energy budgets of the small and large wind farm. The large wind farm triggers an inertial wave with a wind direction amplitude of approximately 10° and a wind speed amplitude of more than 1 m s^{-1} . In a certain region in the far wake of a large wind farm the wind speed is greater than far upstream of the wind farm. The inertial wave also exists for the small wind farm, but the amplitudes are approximately 4 times weaker and thus may be hardly observable in real wind farm flows that are more heterogeneous. The decay of turbulence intensity in the wind farm wakes follows an exponential function and does not depend on the wind farm length. Thus, regarding turbulence, the wake of large wind farms has the same length as that of small wind farms. The wind-farm-induced speed deficit causes an upward displacement of the IL, triggering inertial gravity waves above the small and large wind farm. Because the inertial gravity waves

have a substantial effect on the energy budgets in the wind farm, their existence should be proven by measurements in the future. However, this might be a difficult task because the amplitudes in the vertical wind speed and pressure are very small (0.05 m s^{-1} and 20 Pa).

The energy budget analysis shows that the dominant energy source in small wind farms is the advection of kinetic energy. For large wind farms, however, the advection is much less important and the energy input by vertical turbulent fluxes becomes dominant. Due to the wind-farm-induced wind direction change and the related increase in the ageostrophic wind speed, the energy input by the geostrophic forcing (synoptic-scale pressure gradient) can increase by more than 100 %. This result shows that the presence of large offshore wind farm clusters will modify the offshore, low-roughness BL towards a more onshore-typical, high-roughness BL. This leads to a faster wake recovery and allows for smaller turbine spacings. The energy budget analysis shows that the power output of large wind farms depends on several different energy sources that are determined by the flow state inside and above the BL. Simple wake models do not take these different sources into account and are expected to be inappropriate for accurate power predictions of large wind farms. Proving this hypothesis is an open research task.

The results in this study are based on very idealized simulation setups, assuming a homogeneous surface and a barotropic flow with constant geostrophic wind over a horizontal distance of 400 km and a constant lapse rate over a vertical distance of 5 km. These idealized conditions rarely occur in reality. A deviation from these idealized conditions could distort and weaken the described effects. Additionally, only one meteorological setup is used in this study. A change in BL height, stability or wind speed may affect the results significantly. Consequently, the presented results are a first qualitative guess of what is different in large wind farms compared to small wind farms. Further research is needed to find out how sensitive the results are to the named assumptions and to changes in the meteorological conditions and the turbine spacing. The largest deviation from reality is probably introduced by the assumption of an infinitely wide wind farm. The investigation of a multi-gigawatt wind farm with a finite size in both lateral directions will be the subject of a follow-up study.

Appendix A: Validity of the Boussinesq approximation

The domain height in this study is much larger than in most large-eddy simulation studies that mainly cover the boundary layer. The incompressibility assumption requires the involved vertical length scales to be much smaller than $c^2/g \approx 12 \text{ km}$, where c is the speed of sound (Stull, 1988, p. 77). Therefore, the question of whether the Boussinesq approxi-

mation that assumes a constant density is still valid for these simulations arises. To clarify this question, two additional test simulations were performed. One using the Boussinesq approximation and the other using the anelastic approximation, for which the density can vary with height. The results are shown in Figs. A1–A3. The gravity waves are qualitatively the same in both cases (wavelength, angles of the phase lines). But there are some quantitative differences at greater heights (e.g., 8 km). At that height, the velocity and temperature amplitudes are greater and the pressure amplitudes are smaller for the anelastic approximation. But these differences do not affect the results at hub height (wind speed, direction and perturbation pressure). Therefore, it is appropriate to use the Boussinesq approximation for the simulations in this study.

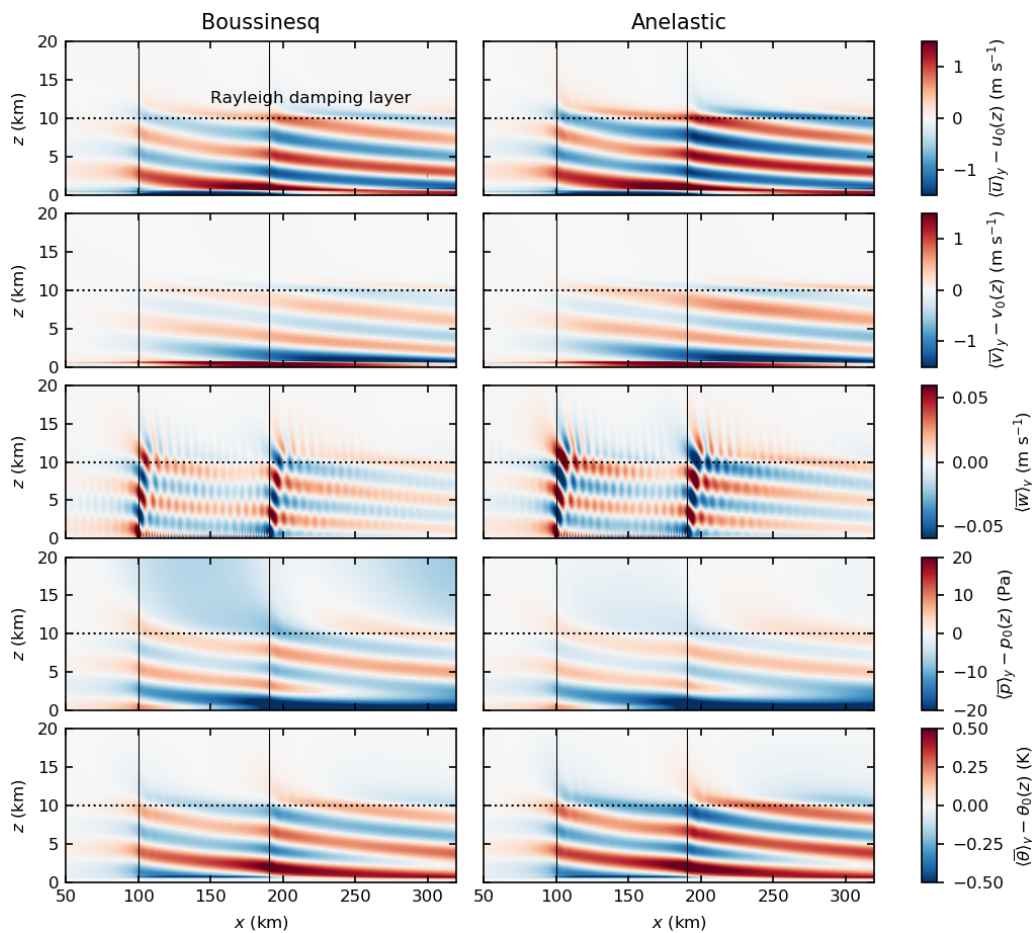


Figure A1. Wave fields for the test simulation with Boussinesq approximation (left) and anelastic approximation (right). All quantities are averaged in time and along y and are given as deviations to the inflow profile.

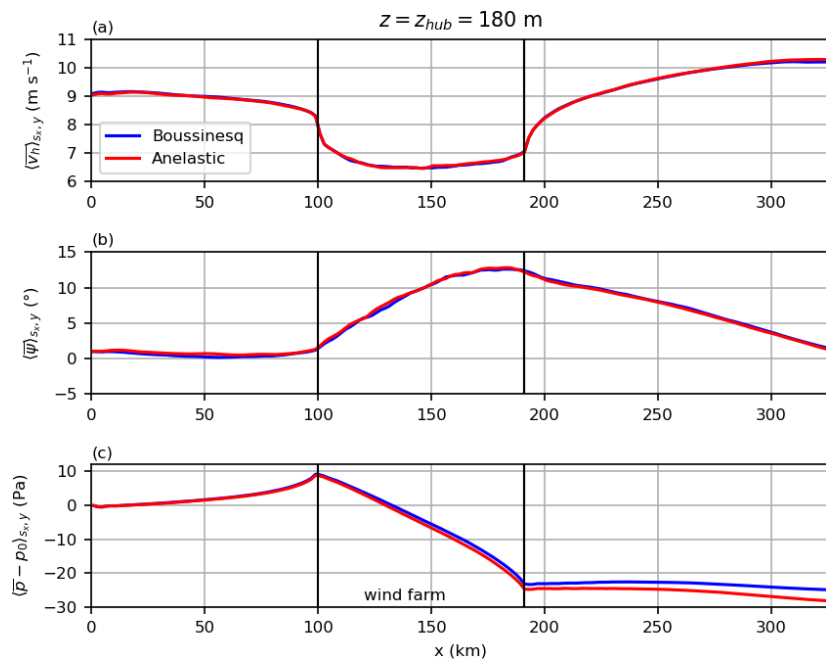


Figure A2. Horizontal wind speed, wind direction and relative perturbation pressure at hub height for both approximation types.

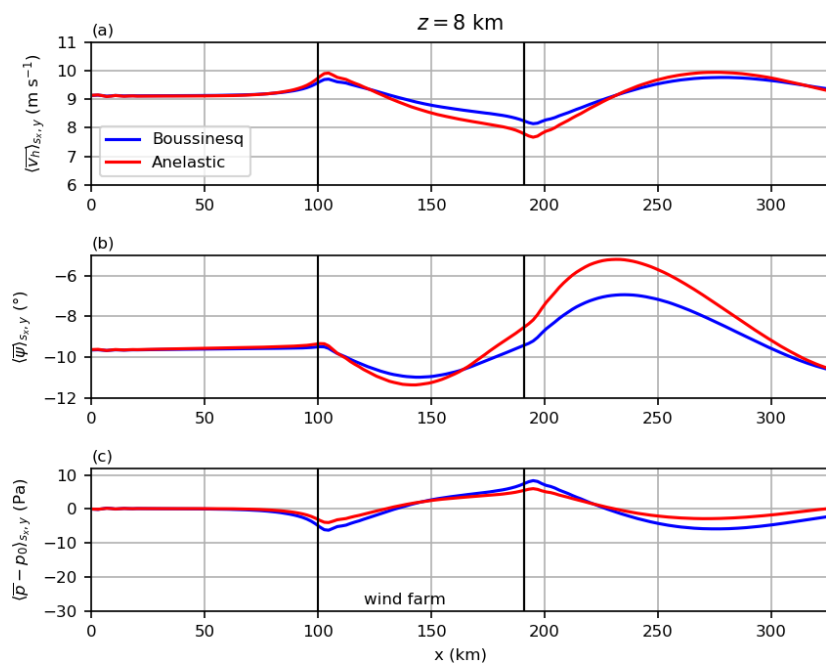


Figure A3. Horizontal wind speed, wind direction and relative perturbation pressure at 8 km height for both approximation types.

Appendix B: Simulation with different latitude

Two additional large wind farm simulations with two different latitudes are performed to prove that the observed wave in the wake is an inertial wave. The domain length is increased further to 655.36 km to capture approximately one wavelength. The latitudes $\phi_1 = 55^\circ$ (original simulation) and $\phi_2 = 80^\circ$ (additional simulation) are used. The larger latitude should result in a shorter inertial period ($T = 12 \text{ h} / \sin(80^\circ) = 12.1 \text{ h}$) and thus a shorter wavelength ($\lambda_I \approx GT \approx 400 \text{ km}$). This shorter wavelength can be observed in Fig. B1, confirming that the wind speed and direction oscillations in the wind farm wake are related to an inertial oscillation.

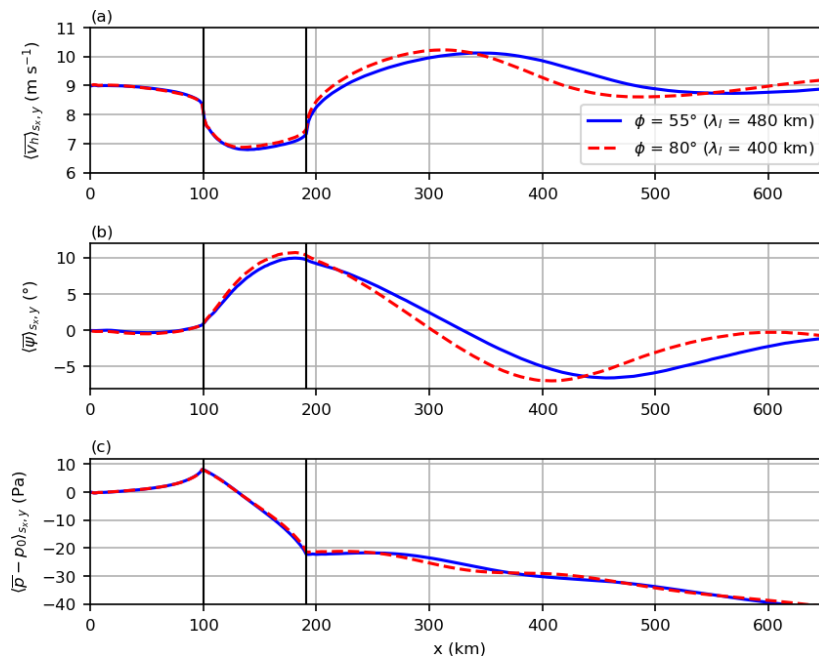


Figure B1. Horizontal wind speed, wind direction and relative perturbation pressure at hub height for the large wind farm case and a latitude of $\phi = 55^\circ$ and $\phi = 80^\circ$.

Code and data availability. The PALM code is available at https://gitlab.palm-model.org/releases/palm_model_system (last access: 31 March 2023). The PALM input files, additional user code and plot scripts are available at <https://doi.org/10.25835/z5zxagiz> (Maas, 2022). Output data are available on request.

Competing interests. The author has declared that there are no competing interests.

Disclaimer. Publisher's note: Copernicus Publications remains neutral with regard to jurisdictional claims in published maps and institutional affiliations.

Acknowledgements. This work was funded by the Federal Maritime and Hydrographic Agency (BSH) (grant no. 10044580) and supported by the North German Supercomputing Alliance (HLRN). Special thanks go to Siegfried Raasch for guiding the manuscript preparation. I thank Dries Allaerts and Dieter Etling for informative discussions about gravity waves and Sukanta Basu for discussions about the validity of the Boussinesq approximation.

Financial support. This work was funded by the Federal Maritime and Hydrographic Agency (BSH) (grant no. 10044580). The publication of this article was funded by the open-access fund of Leibniz Universität Hannover.

Review statement. This paper was edited by Sara C. Pryor and reviewed by Dries Allaerts and two anonymous referees.

References

- Abkar, M. and Porté-Agel, F.: The effect of free-atmosphere stratification on boundary-layer flow and power output from very large wind farms, *Energies*, 6, 2338–2361, <https://doi.org/10.3390/en6052338>, 2013.
- Abkar, M. and Porté-Agel, F.: Mean and turbulent kinetic energy budgets inside and above very large wind farms under conventionally-neutral condition, *Renew. Energ.*, 70, 142–152, <https://doi.org/10.1016/j.renene.2014.03.050>, 2014.
- Allaerts, D. and Meyers, J.: Effect of Inversion-Layer Height and Coriolis Forces on Developing Wind-Farm Boundary Layers, in: 34th Wind Energy Symposium, American Institute of Aeronautics and Astronautics, Reston, Virginia, 1–5, <https://doi.org/10.2514/6.2016-1989>, 2016.
- Allaerts, D. and Meyers, J.: Boundary-layer development and gravity waves in conventionally neutral wind farms, *J. Fluid Mech.*, 814, 95–130, <https://doi.org/10.1017/jfm.2017.11>, 2017.
- Allaerts, D. and Meyers, J.: Gravity Waves and Wind-Farm Efficiency in Neutral and Stable Conditions, *Bound.-Lay. Meteorol.*, 166, 269–299, <https://doi.org/10.1007/s10546-017-0307-5>, 2018.
- Andersen, S. J., Witha, B., Breton, S. P., Sørensen, J. N., Mikkelsen, R. F., and Ivanell, S.: Quantifying variability of Large Eddy Simulations of very large wind farms, *J. Phys.-Conf. Ser.*, 625, 0–12, <https://doi.org/10.1088/1742-6596/625/1/012027>, 2015.
- Baas, P., Van de Wiel, B. J., Van den Brink, L., and Holtlag, A. A.: Composite hodographs and inertial oscillations in the nocturnal boundary layer, *Q. J. Roy. Meteor. Soc.*, 138, 528–535, <https://doi.org/10.1002/qj.941>, 2012.
- BSH: Vorentwurf Flächenentwicklungsplan, Tech. rep., Bundesamt für Seeschifffahrt und Hydrographie, Hamburg, https://www.bsh.de/DE/THEMEN/Offshore/Meeresfachplanung/Flaechenentwicklungsplan/_Anlagen/Downloads/FEP_2022/Vorentwurf_FEP.pdf;jsessionid=E10149D8E4E444564919AD4D2F8F279D.live21301?__blob=publicationFile&v=2 (last access: 28 November 2022), 2021.
- Calaf, M., Meneveau, C., and Meyers, J.: Large eddy simulation study of fully developed wind-turbine array boundary layers, *Phys. Fluids*, 22, 015110, <https://doi.org/10.1063/1.3291077>, 2010.
- Calaf, M., Parlange, M. B., and Meneveau, C.: Large eddy simulation study of scalar transport in fully developed wind-turbine array boundary layers, *Phys. Fluids*, 23, <https://doi.org/10.1063/1.3663376>, 2011.
- Centurelli, G., Vollmer, L., Schmidt, J., Dörenkämper, M., Schröder, M., Lukassen, L. J., Peinke, J., Dörenkämper, M., Schröder, M., Lukassen, L. J., and Peinke, J.: Evaluating Global Blockage engineering parametrizations with LES, *J. Phys.-Conf. Ser.*, 1934, 012021, <https://doi.org/10.1088/1742-6596/1934/1/012021>, 2021.
- Deardorff, J. W.: Stratocumulus-capped mixed layers derived from a three-dimensional model, *Bound.-Lay. Meteorol.*, 18, 495–527, <https://doi.org/10.1007/BF00119502>, 1980.
- Dörenkämper, M., Witha, B., Steinfeld, G., Heinemann, D., and Kühn, M.: The impact of stable atmospheric boundary layers on wind-turbine wakes within offshore wind farms, *J. Wind Eng. Ind. Aerod.*, 144, 146–153, <https://doi.org/10.1016/j.jweia.2014.12.011>, 2015.
- Durran, D. R.: Mountain Waves and Downslope Winds, in: Atmospheric Processes over Complex Terrain, American Meteorological Society, Boston, MA, 59–81, https://doi.org/10.1007/978-1-935704-25-6_4, 1990.
- Gaertner, E., Rinker, J., Sethuraman, L., Zahle, F., Anderson, B., Barter, G., Abbas, N., Meng, F., Bortolotti, P., Skrzypinski, W., Scott, G., Feil, R., Bredmose, H., Dykes, K., Shields, M., Allen, C., and Viselli, A.: Definition of the IEA Wind 15-Megawatt Offshore Reference Wind Turbine, Tech. rep., National Renewable Energy Laboratory, Golden, CO, <https://www.nrel.gov/docs/fy20osti/75698.pdf> (last access: 4 April 2023), 2020.
- Ghaisas, N. S., Archer, C. L., Xie, S., Wu, S., and Maguire, E.: Evaluation of layout and atmospheric stability effects in wind farms using large-eddy simulation, *Wind Energy*, 20, 1227–1240, <https://doi.org/10.1002/we.2091>, 2017.
- Herzig, G.: Global Offshore Wind Report 2021, Tech. Rep. February, World Forum Offshore Wind e.V., <https://gwec.net/wp-content/uploads/2021/03/GWEC-Global-Wind-Report-2021.pdf> (last access: 4 April 2023), 2022.
- Jensen, N. O.: A note on wind generator interaction, *Risø-M-2411 Risø National Laboratory Roskilde*, 1–16, <https://orbit.dtu.dk/en/publications/a-note-on-wind-generator-interaction> (last access: 4 April 2023), 1983.
- Johnstone, R. and Coleman, G. N.: The turbulent Ekman boundary layer over an infinite wind-turbine array, *J. Wind Eng. Ind. Aerod.*, 100, 46–57, <https://doi.org/10.1016/j.jweia.2011.11.002>, 2012.
- Klemp, J. B. and Lilly, D. K.: Numerical Simulation of Hydrostatic Mountain Waves, *J. Atmos. Sci.*, 35, 78–107, [https://doi.org/10.1175/1520-0469\(1978\)035<0078:NSOHMW>2.0.CO;2](https://doi.org/10.1175/1520-0469(1978)035<0078:NSOHMW>2.0.CO;2), 1978.
- Lanzilao, L. and Meyers, J.: Effects of self-induced gravity waves on finite wind-farm operations using a large-eddy simulation framework, *J. Phys.-Conf. Ser.*, 2265, 022043, <https://doi.org/10.1088/1742-6596/2265/2/022043>, 2022.
- Lu, H. and Porté-Agel, F.: Large-eddy simulation of a very large wind farm in a stable atmospheric boundary layer, *Phys. Fluids*, 23, 065101, <https://doi.org/10.1063/1.3589857>, 2011.
- Lu, H. and Porté-Agel, F.: On the Impact of Wind Farms on a Convective Atmospheric Boundary Layer, *Bound.-Lay. Meteorol.*, 157, 81–96, <https://doi.org/10.1007/s10546-015-0049-1>, 2015.
- Maas, O.: LES of small and large wind farm, Leibniz Universität Hannover [data set], <https://doi.org/10.25835/z5zxagiz>, 2022.
- Maas, O. and Raasch, S.: Wake properties and power output of very large wind farms for different meteorological conditions and turbine spacings: a large-eddy simulation case

- study for the German Bight, *Wind Energ. Sci.*, 7, 715–739, <https://doi.org/10.5194/wes-7-715-2022>, 2022.
- Maronga, B., Moene, A. F., van Dinter, D., Raasch, S., Bosveld, F. C., and Gioli, B.: Derivation of Structure Parameters of Temperature and Humidity in the Convective Boundary Layer from Large-Eddy Simulations and Implications for the Interpretation of Scintillometer Observations, *Bound.-Lay. Meteorol.*, 148, 1–30, <https://doi.org/10.1007/s10546-013-9801-6>, 2013.
- Maronga, B., Banzhaf, S., Burmeister, C., Esch, T., Forkel, R., Fröhlich, D., Fuka, V., Gehrke, K. F., Geletič, J., Giersch, S., Gronemeier, T., Groß, G., Heldens, W., Hellsten, A., Hoffmann, F., Inagaki, A., Kadasch, E., Kanani-Sühring, F., Ketelsen, K., Khan, B. A., Knigge, C., Knoop, H., Krč, P., Kurppa, M., Maamari, H., Matzarakis, A., Mauder, M., Pallasch, M., Pavlik, D., Pfafferoth, J., Resler, J., Rissmann, S., Russo, E., Salim, M., Schrempf, M., Schwenkel, J., Seckmeyer, G., Schubert, S., Sühring, M., von Tils, R., Vollmer, L., Ward, S., Witha, B., Wurps, H., Zeidler, J., and Raasch, S.: Overview of the PALM model system 6.0, *Geosci. Model Dev.*, 13, 1335–1372, <https://doi.org/10.5194/gmd-13-1335-2020>, 2020.
- Meyers, J. and Meneveau, C.: Flow visualization using momentum and energy transport tubes and applications to turbulent flow in wind farms, *J. Fluid Mech.*, 715, 335–358, <https://doi.org/10.1017/jfm.2012.523>, 2013.
- Miller, M. J. and Thorpe, A. J.: Radiation conditions for the lateral boundaries of limited-area numerical models, *Q. J. Roy. Meteor. Soc.*, 107, 615–628, <https://doi.org/10.1002/qj.49710745310>, 1981.
- Moeng, C.-H. and Wyngaard, J. C.: Spectral Analysis of Large-Eddy Simulations of the Convective Boundary Layer, *J. Atmos. Sci.*, 45, 3573–3587, [https://doi.org/10.1175/1520-0469\(1988\)045<3573:SAOLES>2.0.CO;2](https://doi.org/10.1175/1520-0469(1988)045<3573:SAOLES>2.0.CO;2), 1988.
- Muñoz-Esparza, D., Cañadillas, B., Neumann, T., and van Beeck, J.: Turbulent fluxes, stability and shear in the offshore environment: Mesoscale modelling and field observations at FINO1, *J. Renew. Sustain. Ener.*, 4, 063136, <https://doi.org/10.1063/1.4769201>, 2012.
- Munters, W., Meneveau, C., and Meyers, J.: Shifted periodic boundary conditions for simulations of wall-bounded turbulent flows, *Phys. Fluids*, 28, 025112, <https://doi.org/10.1063/1.4941912>, 2016.
- Nilsson, K., Ivanell, S., Hansen, K. S., Mikkelsen, R., Sørensen, J. N., Breton, S.-P., and Henningson, D.: Large-eddy simulations of the Lillgrund wind farm, *Wind Energy*, 18, 449–467, <https://doi.org/10.1002/we.1707>, 2015.
- Orlanski, I.: A simple boundary condition for unbounded hyperbolic flows, *J. Comput. Phys.*, 21, 251–269, [https://doi.org/10.1016/0021-9991\(76\)90023-1](https://doi.org/10.1016/0021-9991(76)90023-1), 1976.
- Pedlosky, J.: *Waves in the Ocean and Atmosphere*, Springer Berlin Heidelberg, Berlin, Heidelberg, <https://doi.org/10.1007/978-3-662-05131-3>, 2003.
- Porté-Agel, F., Wu, Y. T., and Chen, C. H.: A numerical study of the effects of wind direction on turbine wakes and power losses in a large wind farm, *Energies*, 6, 5297–5313, <https://doi.org/10.3390/en6105297>, 2013.
- Porté-Agel, F., Lu, H., and Wu, Y. T.: Interaction between large wind farms and the atmospheric boundary layer, *Proc. IUTAM*, 10, 307–318, <https://doi.org/10.1016/j.piutam.2014.01.026>, 2014.
- Saiki, E. M., Moeng, C.-H., and Sullivan, P. P.: Large-Eddy Simulation Of The Stably Stratified Planetary Boundary Layer, *Bound.-Lay. Meteorol.*, 95, 1–30, <https://doi.org/10.1023/A:1002428223156>, 2000.
- Segalini, A. and Chericoni, M.: Boundary-layer evolution over long wind farms, *J. Fluid Mech.*, 925, 1–29, <https://doi.org/10.1017/jfm.2021.629>, 2021.
- Steinfeld, G., Witha, B., Dörenkämper, M., and Gryschka, M.: Hochauflösende Large-Eddy-Simulationen zur Untersuchung der Strömungsverhältnisse in Offshore-Windparks, *promet – Meteorologische Fortbildung*, 39, 163–180, https://www.dwd.de/DE/leistungen/pbfb_verlag_promet/pdf_promethefte/39_3_4_pdf.pdf?__blob=publicationFile&v=2 (last access: 31 March 2023), 2015.
- Stevens, R. J., Gayme, D. F., and Meneveau, C.: Effects of turbine spacing on the power output of extended wind-farms, *Wind Energy*, 19, 359–370, <https://doi.org/10.1002/we.1835>, 2016.
- Stull, R. B.: *An Introduction to Boundary Layer Meteorology*, Springer, 13 edn., <https://doi.org/10.1007/978-94-009-3027-8>, 1988.
- Taylor, J. R. and Sarkar, S.: Internal gravity waves generated by a turbulent bottom Ekman layer, *J. Fluid Mech.*, 590, 331–354, <https://doi.org/10.1017/S0022112007008087>, 2007.
- van de Wiel, B. J., Moene, A. F., Steeneveld, G. J., Baas, P., Bosveld, F. C., and Holtslag, A. A.: A conceptual view on inertial oscillations and nocturnal low-level jets, *J. Atmos. Sci.*, 67, 2679–2689, <https://doi.org/10.1175/2010JAS3289.1>, 2010.
- Veers, P., Dykes, K., Lantz, E., Barth, S., Bottasso, C. L., Carlson, O., Clifton, A., Green, J., Green, P., Holttinen, H., Laird, D., Lehtomäki, V., Lundquist, J. K., Manwell, J., Marquis, M., Meneveau, C., Moriarty, P., Munduate, X., Muskulus, M., Naughton, J., Pao, L., Paquette, J., Peinke, J., Robertson, A., Rodrigo, J. S., Sempreviva, A. M., Smith, J. C., Tuohy, A., and Wiser, R.: Grand challenges in the science of wind energy, *Science*, 366, eaau2027, <https://doi.org/10.1126/science.aau2027>, 2019.
- VerHulst, C. and Meneveau, C.: Large eddy simulation study of the kinetic energy entrainment by energetic turbulent flow structures in large wind farms, *Phys. Fluids*, 26, 025113, <https://doi.org/10.1063/1.4865755>, 2014.
- Wicker, L. J. and Skamarock, W. C.: Time-splitting methods for elastic models using forward time schemes, *Mon. Weather Rev.*, 130, 2088–2097, [https://doi.org/10.1175/1520-0493\(2002\)130<2088:TSMFEM>2.0.CO;2](https://doi.org/10.1175/1520-0493(2002)130<2088:TSMFEM>2.0.CO;2), 2002.
- Witha, B., Steinfeld, G., Dörenkämper, M., and Heinemann, D.: Large-eddy simulation of multiple wakes in offshore wind farms, *J. Phys.-Conf. Ser.*, 555, 12108, <https://doi.org/10.1088/1742-6596/555/1/012108>, 2014.
- Wu, K. L. and Porté-Agel, F.: Flow adjustment inside and around large finite-size wind farms, *Energies*, 10, 4–9, <https://doi.org/10.3390/en10122164>, 2017.
- Wu, Y.-T. and Porté-Agel, F.: Large-Eddy Simulation of Wind-Turbine Wakes: Evaluation of Turbine Parametrisations, *Bound.-Lay. Meteorol.*, 138, 345–366, <https://doi.org/10.1007/s10546-010-9569-x>, 2011.
- Wu, Y.-T. and Porté-Agel, F.: Modeling turbine wakes and power losses within a wind farm using LES: An application to the Horns Rev offshore wind farm, *Renew. Energ.*, 75, 945–955, <https://doi.org/10.1016/j.renene.2014.06.019>, 2015.

556

O. Maas: From gigawatt to multi-gigawatt wind farms

Zhang, M., Arendshorst, M. G., and Stevens, R. J.: Large eddy simulations of the effect of vertical staggering in large wind farms, *Wind Energy*, 22, 189–204, <https://doi.org/10.1002/we.2278>, 2019.

5 Large-eddy simulation of a 15 GW wind farm: flow effects, energy budgets and comparison with wake models

5.1 Declaration of Contributions

O. Maas performed the simulations and wrote the manuscript. The manuscript preparation was guided by S. Raasch. The paper was edited by Joseph Lee and reviewed by Alessandro Corsini and Akshoy Ranjan Paul.

5.2 Research Article

Maas, O.: Large-eddy simulation of a 15 GW wind farm: Flow effects, energy budgets and comparison with wake models, *Frontiers in Mechanical Engineering*, 9, 1–23, doi: 10.3389/fmech.2023.1108180, 2023b.

©The author 2023. CC BY 4.0 License



OPEN ACCESS

EDITED BY
 Joseph Lee,
 Pacific Northwest National Laboratory
 (DOE), United States

REVIEWED BY
 Alessandro Corsini,
 Sapienza University of Rome, Italy
 Akshoy Ranjan Paul,
 Motilal Nehru National Institute of
 Technology Allahabad, India

*CORRESPONDENCE
 Oliver Maas,
 ✉ maas@meteo.uni-hannover.de

SPECIALTY SECTION
 This article was submitted to
 Turbomachinery,
 a section of the journal
 Frontiers in Mechanical Engineering

RECEIVED 25 November 2022
 ACCEPTED 14 March 2023
 PUBLISHED 27 March 2023

CITATION
 Maas O (2023), Large-eddy simulation of
 a 15 GW wind farm: Flow effects, energy
 budgets and comparison with
 wake models.
Front. Mech. Eng 9:1108180.
 doi: 10.3389/fmech.2023.1108180

COPYRIGHT
 © 2023 Maas. This is an open-access
 article distributed under the terms of the
[Creative Commons Attribution License
 \(CC BY\)](https://creativecommons.org/licenses/by/4.0/). The use, distribution or
 reproduction in other forums is
 permitted, provided the original author(s)
 and the copyright owner(s) are credited
 and that the original publication in this
 journal is cited, in accordance with
 accepted academic practice. No use,
 distribution or reproduction is permitted
 which does not comply with these terms.

Large-eddy simulation of a 15 GW wind farm: Flow effects, energy budgets and comparison with wake models

Oliver Maas*

Institute of Meteorology and Climatology, Leibniz University Hannover, Hannover, Germany

Planned offshore wind farm clusters have a rated capacity of more than 10 GW. The layout optimization and yield estimation of wind farms is often performed with computationally inexpensive, analytical wake models. As recent research results show, the flow physics in large (multi-gigawatt) offshore wind farms are more complex than in small (sub-gigawatt) wind farms. Since analytical wake models are tuned with data of existing, sub-gigawatt wind farms they might not produce accurate results for large wind farm clusters. In this study the results of a large-eddy simulation of a 15 GW wind farm are compared with two analytical wake models to demonstrate potential discrepancies. The TurbOPark model and the Niayifar and Porté-Agel model are chosen because they use a Gaussian wake profile and a turbulence model. The wind farm has a finite size in the crosswise direction, unlike as in many other large-eddy simulation wind farm studies, in which the wind farm is effectively infinitely wide due to the cyclic boundary conditions. The results show that new effects like crosswise divergence and convergence occur in such a finite-size multi-gigawatt wind farm. The comparison with the wake models shows that there are large discrepancies of up to 40% between the predicted wind farm power output of the wake models and the large-eddy simulation. An energy budget analysis is made to explain the discrepancies. It shows that the wake models neglect relevant kinetic energy sources and sinks like the geostrophic forcing, the energy input by pressure gradients and energy dissipation. Taking some of these sources and sinks into account could improve the accuracy of the wake models.

KEYWORDS

large-eddy simulation, large wind farms, wake model, energy budget analysis, global blockage effect, gravity waves, TurbOPark, PALM

1 Introduction

The installed offshore wind power in Europe is expected to grow significantly in the next three decades due to high offshore wind targets of several countries. For example, the four countries Belgium, Denmark, Germany and the Netherlands defined an offshore wind target of 150 GW for the year 2050 in the Esbjerg declaration (Frederiksen et al., 2022). The wind farm clusters that are required to achieve this target will have a rated power on the order of 10 GW as the offshore wind plans for Germany show (BSH, 2022).

An efficient wind farm cluster design can only be achieved if the layout optimization and yield estimation is done with simulation tools that deliver accurate results. Due to the large number of possible combinations between wind speed, wind direction, farm layout and other

parameters, these simulations can only be performed with computationally inexpensive analytical wake models. However, analytical wake models are tuned with data of existing wind farms that are much smaller than the planned wind farm clusters. The wake models might thus not be suitable for predicting the power output of large wind farm clusters. A sound method to investigate the wake flow and power output of large potential wind farms is large-eddy simulation (LES). With LES all relevant processes such as turbulent entrainment of energy or Coriolis effects are modeled. Many wind farm LES studies have been performed in recent years, e.g., [Allaerts and Meyers \(2017\)](#), [Wu and Porté-Agel \(2017\)](#), [Zhang et al. \(2019\)](#), [Centurelli et al. \(2021\)](#), [Lanzilao and Meyers \(2022\)](#) and [Maas and Raasch \(2022\)](#). They show that complex flow phenomenon like inversion layer displacement, gravity wave induced pressure gradients, flow blockage and Coriolis force related wind direction changes can occur for large wind farms. Analytical wake models do not account for these effects which might result in large errors in the power prediction. Currently there is no LES study of a multi-gigawatt wind farm that compares the results with analytical wake models.

The aim of this study is to fill this research gap by comparing two analytical wake models with a large-eddy simulation of a 15 GW wind farm. The NP model ([Niayifar and Porté-Agel, 2016](#)) and the TurbOPark model ([Pedersen et al., 2022](#)) are chosen because they use a Gaussian wake profile and a turbulence model. Potential discrepancies in the power output are identified and explained by an energy budget analysis. The LES model domain has a size of 245 km × 138 km × 8 km and is filled with a turbine wake resolving grid resulting in 6.8 billion grid points in total. The wind farm has a finite size in both lateral directions unlike in many other studies in which the wind farm is effectively infinitely wide in the crosswise direction (e.g., [Stevens et al., 2016](#); [Allaerts and Meyers, 2017](#); [Maas, 2022b](#)). The LES results are compared with the infinitely wide wind farm case of [Maas \(2022b\)](#) to show which new flow effects occur if the more realistic finite size wind farm setup is used.

The paper is structured as follows: The LES model and simulation setup are described in [Section 2](#). The results are presented in [Section 3](#), and [Section 4](#) concludes and discusses the results of the study.

2 Materials and methods

2.1 Numerical model

The large-eddy simulation is carried out with the Parallelized Large-eddy Simulation Model PALM ([Maronga et al., 2020](#)). PALM is developed at the Institute of Meteorology and Climatology of the Leibniz Universität Hannover, Germany. Several wind farm flow investigations have been successfully conducted with this code in the past (e.g., [Witha et al., 2014](#); [Dörenkämper et al., 2015](#); [Krüger et al., 2022](#); [Maas and Raasch, 2022](#)). PALM solves the non-hydrostatic, incompressible Navier-Stokes equations in Boussinesq-approximated form. The equations for the conservation of mass, momentum and internal energy are:

$$\frac{\partial \tilde{u}_j}{\partial x_j} = 0, \quad (1)$$

$$\frac{\partial \tilde{u}_i}{\partial t} = -\frac{\partial \tilde{u}_i \tilde{u}_j}{\partial x_j} - \epsilon_{ijk} f_j \tilde{u}_k + \epsilon_{i3j} f_3 u_{g,j} - \frac{1}{\rho_0} \frac{\partial \pi^*}{\partial x_i} + g \frac{\tilde{\theta} - \langle \tilde{\theta} \rangle}{\langle \tilde{\theta} \rangle} \delta_{i3} - \frac{\partial}{\partial x_j} \left(\overline{u_i' u_j'} - \frac{2}{3} e \delta_{ij} \right) + d_i, \quad (2)$$

$$\frac{\partial \tilde{\theta}}{\partial t} = -\frac{\partial \tilde{u}_j \tilde{\theta}}{\partial x_j} - \frac{\partial}{\partial x_j} \left(\overline{u_j' \theta'} \right), \quad (3)$$

where angular brackets indicate horizontal averaging, a double prime indicates subgrid-scale (SGS) quantities, a tilde denotes filtering over a grid volume, $i, j, k \in \{1, 2, 3\}$, u_i, u_j, u_k are the velocity components in the respective directions (x_i, x_j, x_k), θ is potential temperature, t is time, $f_i = (0, 2\Omega \cos(\phi), 2\Omega \sin(\phi))$ is the Coriolis parameter with the Earth's angular velocity $\Omega = 0.729 \times 10^{-4} \text{ rad}\cdot\text{s}^{-1}$ and the geographical latitude ϕ . The geostrophic wind speed components are $u_{g,j}$ and the basic state density of dry air is ρ_0 . The modified perturbation pressure is $\pi^* = p + \frac{2}{3} \rho_0 e$, where p is the perturbation pressure and $e = \frac{1}{2} \overline{u_i' u_i'}$ is the SGS turbulence kinetic energy. The gravitational acceleration is $g = 9.81 \text{ m}\cdot\text{s}^{-2}$, δ is the Kronecker delta and d_i are the forces of the wind turbine actuator discs.

The SGS model uses a 1.5-order closure according to [Deardorff \(1980\)](#), modified by [Moeng and Wyngaard \(1988\)](#) and [Saiki et al. \(2000\)](#). The numerical grid is a structured, equidistant, staggered Arakawa C-grid that can be vertically stretched above a certain height.

The wind turbines are represented by an advanced actuator disc model with rotation (ADM-R) that acts as an axial momentum sink and an angular momentum source (inducing wake rotation). The ADM-R is described in detail by [Wu and Porté-Agel \(2011\)](#) and was implemented in PALM by [Steinfeld et al. \(2015\)](#). Additional information is also given by [Maas and Raasch \(2022\)](#). The wind turbines have a yaw controller, that aligns the rotor axis with the wind direction.

2.2 Main simulation

The wind farm consists of $32 \times 32 = 1,024$ wind turbines. The IEA 15 MW wind turbine with a rotor diameter of $D = 240 \text{ m}$ and a rated power of 15 MW is used ([Gaertner et al., 2020](#)). The hub height is set to 180 m instead of 150 m, so that the turbulent fluxes at the rotor bottom are better resolved by the numerical grid. The turbine spacing in the streamwise and crosswise direction is $s_x = s_y = 6 D$, resulting in an installed power density of $7.23 \text{ W}\cdot\text{m}^{-2}$, which is a typical value for currently planned offshore wind farms in the German Bight ([BSH, 2022](#)). The wind turbines are arranged in a staggered configuration, i.e., every second row is shifted by $s_y/2$ in the y -direction. The wind farm has a size of $l_x \times l_y = 44.64 \text{ km} \times 45.36 \text{ km}$.

The numerical grid has a size of $N_x \times N_y \times N_z = 12,288 \times 6,912 \times 80 \approx 6.8 \times 10^9$ grid points. The grid spacing is $\Delta x = \Delta y = \Delta z = 20 \text{ m}$, corresponding to 12 grid points per rotor diameter. With this grid spacing the ratio of SGS-TKE to total TKE (SGS and resolved TKE) is below 20% in the wind turbine wakes, except for the first two columns, where it reaches values of approximately 30%. Above $z = 700 \text{ m}$, in the non-turbulent free atmosphere, the grid is stretched vertically by 8% every grid level up to $\Delta z_{\text{max}} =$

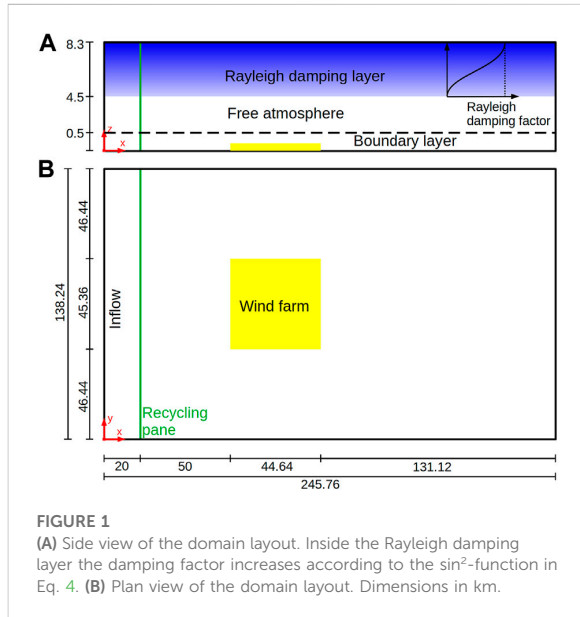


FIGURE 1 (A) Side view of the domain layout. Inside the Rayleigh damping layer the damping factor increases according to the \sin^2 -function in Eq. 4. (B) Plan view of the domain layout. Dimensions in km.

400 m. This results in a domain size of $L_x \times L_y \times L_z = 245.76 \text{ km} \times 138.24 \text{ km} \times 8.28 \text{ km}$ (see Figure 1). The large domain height is needed to cover at least one vertical wavelength of the stationary gravity waves (5.3 km) that form in the free atmosphere above the wind farm (refer to Allaerts and Meyers (2017) for details). To avoid the reflection of gravity waves at the domain top, there is a Rayleigh damping layer above $z_{rd} = 4.5 \text{ km}$. In this damping layer the velocity components are damped towards their respective inflow value by subtracting a tendency that is proportional to the deviation from the inflow value. The magnitude of the damping is given by the Rayleigh damping factor that increases from zero at the bottom of the damping layer to its maximum value of $f_{rdm} = 0.025(\Delta t)^{-1} \approx 0.017 \text{ s}^{-1}$ at the domain top according to this function (see Figure 1):

$$f_{rd}(z) = f_{rdm} \sin^2\left(0.5\pi \frac{z - z_{rd}}{L_z - z_{rd}}\right). \quad (4)$$

This sine wave profile leads to less reflections compared to a linear profile (Klemp and Lilly, 1978).

The flow field is initialized by the instantaneous flow field of the last time step of a precursor simulation. Details about the precursor simulation and the meteorological parameters are given in the next section. The flow field is filled cyclically into the main domain, because it is larger than the precursor domain. At the inflow, vertical profiles of the potential temperature and the velocity components averaged over the last 4 h of the precursor simulation are prescribed (see Figure 2). The turbulent state of the inflow is maintained by a turbulence recycling method that maps the turbulent fluctuations from the recycling plane at $x = 20 \text{ km}$ onto the inflow plane at $x = 0$. The turbulent fluctuations are shifted in the y -direction by $+53.76 \text{ km}$ to avoid streamwise streaks in the averaged velocity fields, for further details please refer to Munter et al. (2016). More details of the recycling method are provided in Maas and Raasch (2022). The wind farm has a distance of 50 km to the recycling plane to reduce the influence of the wind farm flow blockage on the flow at the recycling plane. To avoid an artificial formation of gravity waves at the inflow boundary, there is a second Rayleigh damping zone between $x = 0$ and $x = 10 \text{ km}$. The damping mechanism is the same as in the Rayleigh damping layer except that it only acts on the potential temperature field. The damping factor has a magnitude of $f_{ptm} = 0.025(\Delta t)^{-1} \approx 0.017 \text{ s}^{-1}$ at the inflow boundary and decreases to zero at $x = 10 \text{ km}$ according to the sine wave profile in Eq. 4.

Cyclic boundary conditions are applied at the northern and southern domain boundaries (y -direction). Radiation boundary conditions as described by Miller and Thorpe (1981) and Orlanski (1976) are applied at the outflow (right) domain boundary. At the domain top and bottom a Neumann boundary condition for the perturbation pressure and Dirichlet boundary conditions for the velocity components are applied. For the potential temperature, a constant lapse rate is assumed at the domain top. The physical simulation time of the main simulation

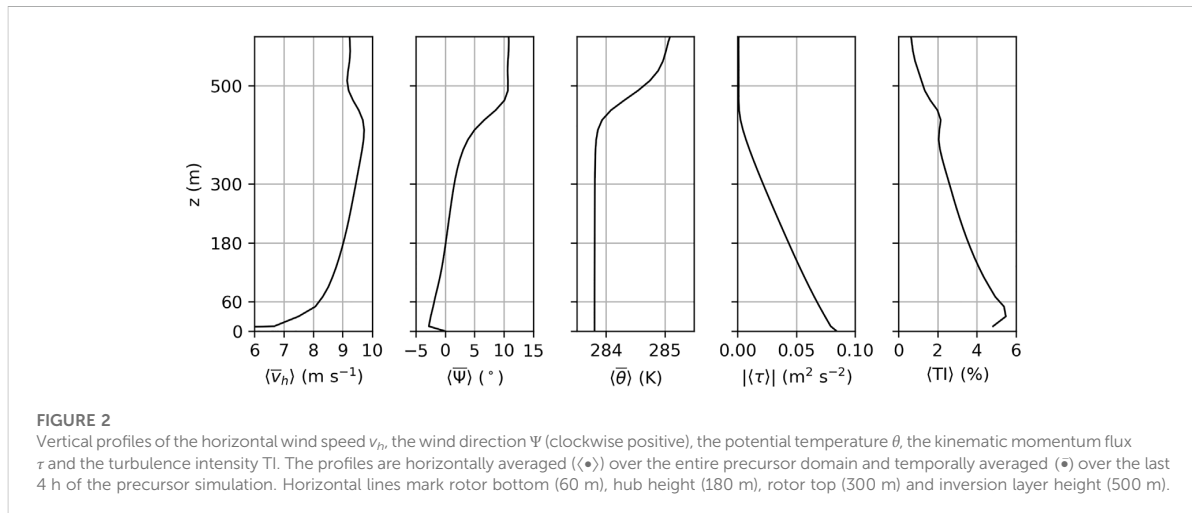
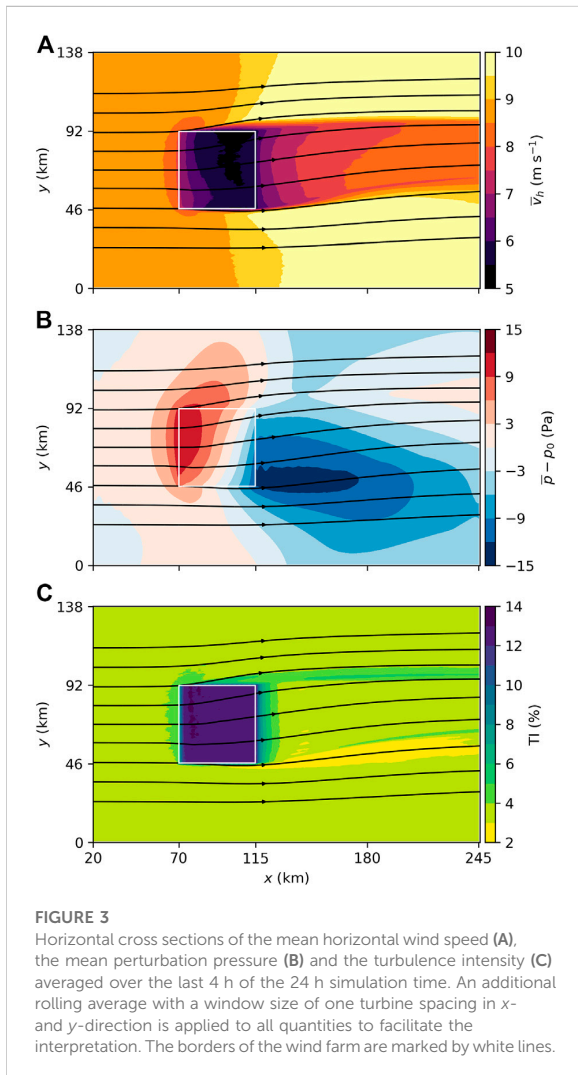


FIGURE 2 Vertical profiles of the horizontal wind speed v_h , the wind direction Ψ (clockwise positive), the potential temperature θ , the kinematic momentum flux τ and the turbulence intensity TI . The profiles are horizontally averaged ($\langle \bullet \rangle$) over the entire precursor domain and temporally averaged ($\bar{\bullet}$) over the last 4 h of the precursor simulation. Horizontal lines mark rotor bottom (60 m), hub height (180 m), rotor top (300 m) and inversion layer height (500 m).



is 24 h and the presented data are averaged over the last 4 h. The simulation ran on 5,184 cores for a wall-clock time of 50 h.

2.3 Precursor simulation

Initial conditions and inflow profiles are obtained by a precursor simulation that does not contain a wind farm. It has cyclic boundary conditions in both lateral directions and a domain size of $L_{x,pre} \times L_{y,pre} \times L_{z,pre} = 3.84 \text{ km} \times 2.24 \text{ km} \times 8.3 \text{ km}$. The number of vertical grid points, the vertical grid stretching and Rayleigh damping levels are the same as in the main simulation. The initial horizontal velocity is set to the geostrophic wind $(U_g, V_g) = (9.064, -1.722) \text{ m}\cdot\text{s}^{-1}$, resulting in a steady-state hub height mean wind speed of $9.0 \text{ m}\cdot\text{s}^{-1}$ that is aligned with the x -axis. The latitude is $\phi = 55^\circ\text{N}$. The initial potential temperature is set to 283 K at the surface and has a lapse rate of $\Gamma = +3.5 \text{ K}\cdot\text{km}^{-1}$ above. The onset of turbulence is triggered by small random perturbations in the horizontal velocity

field below a height of 250 m in the entire precursor domain at the first time step. The amplitude of the perturbations is set to $0.25 \text{ m}\cdot\text{s}^{-1}$. The roughness length is $z_0 = 1 \text{ mm}$ and a constant flux layer is assumed between the surface and the lowest computational grid level. The heat flux at the surface is set to zero so that a conventionally neutral boundary layer with a final boundary layer height of $h \approx 500 \text{ m}$ develops. The physical simulation time of the precursor simulation is 48 h. Figure 2 shows temporally and horizontally averaged profiles of the horizontal wind speed v_h , the wind direction Ψ , the potential temperature θ , the total turbulent vertical kinematic momentum flux τ and the turbulence intensity (TI):

$$TI = \frac{\sqrt{\frac{2}{3} \text{TKE}}}{v_h}, \quad (5)$$

with the turbulence kinetic energy (TKE) defined as the sum of the resolved and the SGS-TKE:

$$\text{TKE} = \frac{1}{2} (\overline{u'^2} + \overline{v'^2} + \overline{w'^2}) + \bar{\epsilon}, \quad (6)$$

where u' , v' and w' are the deviations from the temporal mean quantity of the resolved flow, e.g., $u' = u - \bar{u}$. The temporal mean is used instead of the horizontal mean so that the TKE can be computed at every grid point.

3 Results

3.1 Mean flow at hub height

Figure 3A shows the mean horizontal wind speed at hub height. In general, the flow field shows the typical wind farm flow features such as flow blockage in front of the wind farm, a significant speed deficit inside the wind farm and a slow wind speed recovery in the wake. The flow is decelerated from $9 \text{ m}\cdot\text{s}^{-1}$ to below $8 \text{ m}\cdot\text{s}^{-1}$ upstream of the wind farm, is further reduced to below $5.5 \text{ m}\cdot\text{s}^{-1}$ inside the wind farm and recovers to more than $8 \text{ m}\cdot\text{s}^{-1}$ in the wake. However, there are also some remarkable features such as horizontal divergence, flow deflection and wake narrowing.

The flow diverges in the crosswise direction, resulting in a wind direction change of -4° at the northwestern and $+2^\circ$ at the southwestern wind farm corner. The divergence is caused by a high pressure region of approximately $+12 \text{ Pa}$ near the wind farm leading edge (see Figure 3B).

The second remarkable feature is the narrowing of the wake. Using a wind speed threshold of $8.5 \text{ m}\cdot\text{s}^{-1}$, the initial wake width at $x = 120 \text{ km}$ (5.36 km behind the last turbine) is $\delta_w = 51 \text{ km}$. This is wider than the wind farm itself (45.36 km) because the wake flow also leaves the northern wind farm edge. Further downstream the wake narrows to $\delta_w = 43 \text{ km}$ and $\delta_w = 38 \text{ km}$ at $x = 180 \text{ km}$ and $x = 240 \text{ km}$, respectively. The wake narrowing (crosswise convergence) is caused by the flow acceleration (streamwise divergence) in the wake. The vertical divergence/convergence has no significant contribution to the wake narrowing (analysis not shown).

The flow divergence and wake narrowing do not occur for smaller wind farms, such as the Horns Rev offshore wind farm (Porté-Agel et al., 2020). These effects do also not occur in simulation setups in which the wind farm is effectively infinitely

wide in the cyclic y -direction, such as in [Stevens et al. \(2016\)](#), [Allaerts and Meyers \(2017\)](#), [Wu and Porté-Agel \(2017\)](#) and [Maas \(2022b\)](#).

The third remarkable feature is the counterclockwise deflection of the flow that reaches a maximum of approximately -8° at the center of the trailing edge of the wind farm. As shown by [Maas and Raasch \(2022\)](#) and [Maas \(2022b\)](#) this deflection is caused by a reduction of the Coriolis force in the wind speed deficit region and occurs for wind farm flows for which the Rossby number is on the order of 1 or smaller. The Rossby number in this study is

$$Ro = \frac{U_g}{L_x f} = \frac{9 \text{ ms}^{-1}}{45 \text{ km} \times 1.2 \times 10^{-4}} \approx 1.7, \quad (7)$$

which is close to 1 and thus flow deflection occurs. The combination of the divergence and the flow deflection results in a wind direction change of more than -10° in the northern part of the wind farm. In the wake, the wind direction turns back clockwise and at the outflow boundary it reaches the initial value of the inflow. The clockwise wake turning has also been shown by [Maas \(2022b\)](#) for an infinitely wide wind farm, where it was related to supergeostrophic wind speeds in the wake due to an inertial oscillation. But in this study the wind speed in the wake does not become supergeostrophic. The clockwise deflection in the wake is rather a result of the pressure distribution.

The pressure distribution (see [Figure 3B](#)) generally has the expected pattern with a high pressure region in the upstream part of the wind farm and a low pressure region in the wake. The streamwise variation in the pressure is related to stationary gravity waves in the stably stratified free atmosphere that are described in the next section. However, in the wake the pressure distribution has a high asymmetry in the y -direction with higher pressure at the northern wake edge and lower pressure at the southern wake edge. This crosswise pressure gradient results in a southward pointing tendency so that the wind direction in the wake turns clockwise and adjusts to the wind direction of the surrounding flow. Also the high pressure region in the upstream part of the wind farm is not symmetric. This is the result of the fact that the flow in the free atmosphere is veered by approximately 10° to the right relative to the flow at hub height (see [Figure 2](#)). Thus the gravity wave related pressure field is also rotated by 10° to the right.

[Figure 3C](#) shows the TI at hub height. The ambient TI at hub height is approximately 3.5% (see also [Figure 2](#)). Upstream of the wind farm there is a slight increase in TI which is caused by the reduction in wind speed rather than an increase in TKE (see Eq. 5). Inside the wind farm the TI increases to more than 12% within two turbine columns and is approximately constant up to the trailing edge of the wind farm. In the wake the TI drops to below 5% within 10 km. At the northern wake edge the TI stays at a higher level (approx. 5%) and at the southern wake edge the TI drops to below 3%. It is not yet fully understood why these streaks of higher and lower TI occur and why they persist for over 100 km.

3.2 Inversion layer displacement and gravity waves

The flow deceleration inside the wind farm does not only cause a crosswise divergence but also a vertical divergence. Consequently, the inversion layer is displaced upwards, as can be seen in [Figure 4](#).

Here, the inversion layer displacement is defined as the inversion layer height relative to the inversion layer height at the recycling plane at $x = 20$ km:

$$\delta = z_i - \langle z_i(x = 20 \text{ km}) \rangle_y. \quad (8)$$

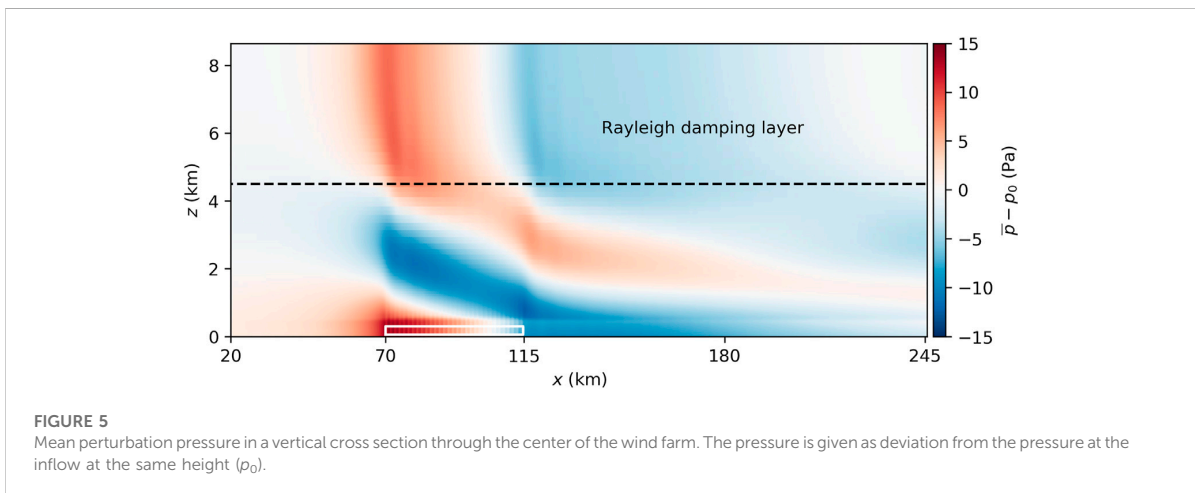
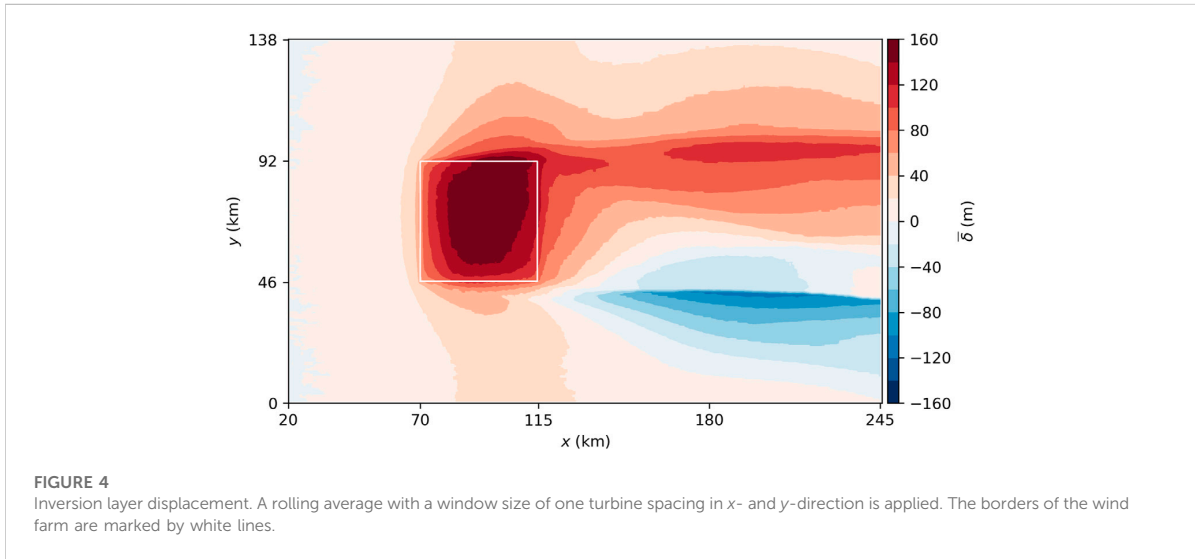
The inversion layer height is defined as the height at which the maximum vertical potential temperature gradient occurs. The maximum displacement of +120 m occurs in the north-eastern part of the wind farm, where also the minimum wind speed at hub height occurs. In the wake, the inversion layer displacement is very asymmetric with positive values in the northern part and negative values in the southern part. This asymmetry is caused by the wake deflection that leads to a crosswise convergence and thus ascending motion in the northern part of the wake and to a crosswise divergence and thus descending motion in the southern part of the wake (not shown). On average, there is a positive inversion layer displacement in the wake.

The inversion layer displacement triggers gravity waves in the overlying free atmosphere, as described by, e.g., [Allaerts and Meyers \(2017\)](#) and [Maas \(2022b\)](#). The gravity waves affect the velocity, pressure and temperature fields. A detailed discussion of the gravity waves is beyond the scope of this study. Thus, only one vertical cross-section of the perturbation pressure in the center of the wind farm is shown in [Figure 5](#). It shows that the pressure distribution in the wind farm (see [Figure 3B](#)) is related to the above lying gravity waves. The waves have upstream inclined phase lines indicating upwards propagating energy. The Rayleigh damping layer reduces the reflectivity of the upper domain boundary to less than 10%. The reflectivity is obtained by the method described by [Allaerts and Meyers \(2017\)](#), which is a modified version of the method described by [Taylor and Sarkar \(2007\)](#).

3.3 Energy budget analysis

In this section the kinetic energy budgets inside the wind farm are investigated in detail. The results can be used to explain potential discrepancies between the wake models and PALM in the next section. Additionally, it is possible to quantify the effect of the lateral (south/north) wind farm boundaries on the wind farm energy budgets by comparing the results with semi-infinite wind farm LES studies. The analysis is very similar to the energy budget analysis made by [Allaerts and Meyers \(2017\)](#); [Maas \(2022b\)](#) but is extended to also cover the energy fluxes through the south/north boundaries of the wind farm. These are net zero in the aforementioned studies due to the cyclic boundary conditions at the south/north boundaries of the domain and because the wind farm extends over the entire domain in the y -direction. The energy budgets are calculated for $16 \times 16 = 256$ wind turbine control volumes Ω_{wt} . Each control volume (CV) covers 4 wind turbines as sketched in [Figure 6](#). The CVs have a streamwise and crosswise length of 2 turbine spacings. The bottom and top boundaries of Ω_{wt} are $(z_b, z_t) = (50, 310)$ m, which is 1 dz larger than the rotor diameter, to cover the smeared forces of the wind turbine model. The sum of all wind turbine CVs gives the wind farm CV $\Omega_{wf} = \Sigma \Omega_{wt}$.

The equation for the conservation of the mean resolved-scale kinetic energy can be obtained by multiplying PALM's equation for momentum conservation (Eq. 2) with u_b , averaging in time, assuming stationarity and integrating over the CV Ω :



$$\begin{aligned}
 0 = & \underbrace{-\int_{\Omega} \frac{\partial \bar{u}_j \bar{E}_k}{\partial x_j} d\Omega}_A \\
 & \underbrace{-\int_{\Omega} \frac{\partial}{\partial x_j} \bar{u}_i \bar{u}'_i \bar{u}'_j d\Omega + \int_{\Omega} \frac{\partial}{\partial x_j} \bar{u}_i \bar{\tau}_{ij} d\Omega - \int_{\Omega} \frac{\partial}{\partial x_j} \frac{1}{2} \bar{u}'_j \bar{u}'_i \bar{u}'_i d\Omega - \int_{\Omega} \frac{\bar{u}'_i \partial \pi'}{\rho_0 \partial x_i} d\Omega}_F \\
 & \underbrace{+ \int_{\Omega} (\bar{u}_2 f_{3u_{g,1}} - \bar{u}_1 f_{3u_{g,2}}) d\Omega}_G \underbrace{- \int_{\Omega} \frac{\bar{u}_i \partial \bar{\pi}'}{\rho_0 \partial x_i} d\Omega}_P + \underbrace{\int_{\Omega} \frac{g}{\theta_0} (\bar{\theta} - \theta_0) \bar{u}_3 d\Omega}_B \\
 & \underbrace{- \int_{\Omega} \frac{\partial \bar{u}_i}{\partial x_j} d\Omega - \mathcal{R}}_D + \underbrace{\int_{\Omega} \bar{u}_i \bar{d}_i d\Omega}_W,
 \end{aligned} \tag{9}$$

Note that the mean kinetic energy (KE, \bar{E}_k) contains the kinetic energy of the mean flow and the turbulence kinetic energy (TKE) of the resolved flow:

$$\bar{E}_k = \frac{1}{2} \bar{u}_i \bar{u}_i = \frac{1}{2} \bar{u}_i \bar{u}_i + \frac{1}{2} \bar{u}'_i \bar{u}'_i \tag{10}$$

The terms of Eq. 9 are categorized as follows:

- A : Divergence of KE advection
- F : Turbulent fluxes
- G : Energy input by the geostrophic forcing
- P : Energy input by mean perturbation pressure gradients
- B : Energy input by buoyancy forces
- D : Dissipation by SGS model less the residual \mathcal{R}
- W : Energy extraction by the wind turbines

The turbulent fluxes (\mathcal{F}) can be subdivided into the transport of kinetic energy of the mean flow by resolved turbulent stresses (term 1), transport of KE by SGS stresses (term 2), turbulent transport of resolved-scale TKE by velocity fluctuations (term 3) and turbulent transport of KE by perturbation pressure fluctuations (term 4). Eq. 9 has a positive residual \mathcal{R} , because the magnitude of the calculated dissipation is underestimated, which has two reasons: First, the local

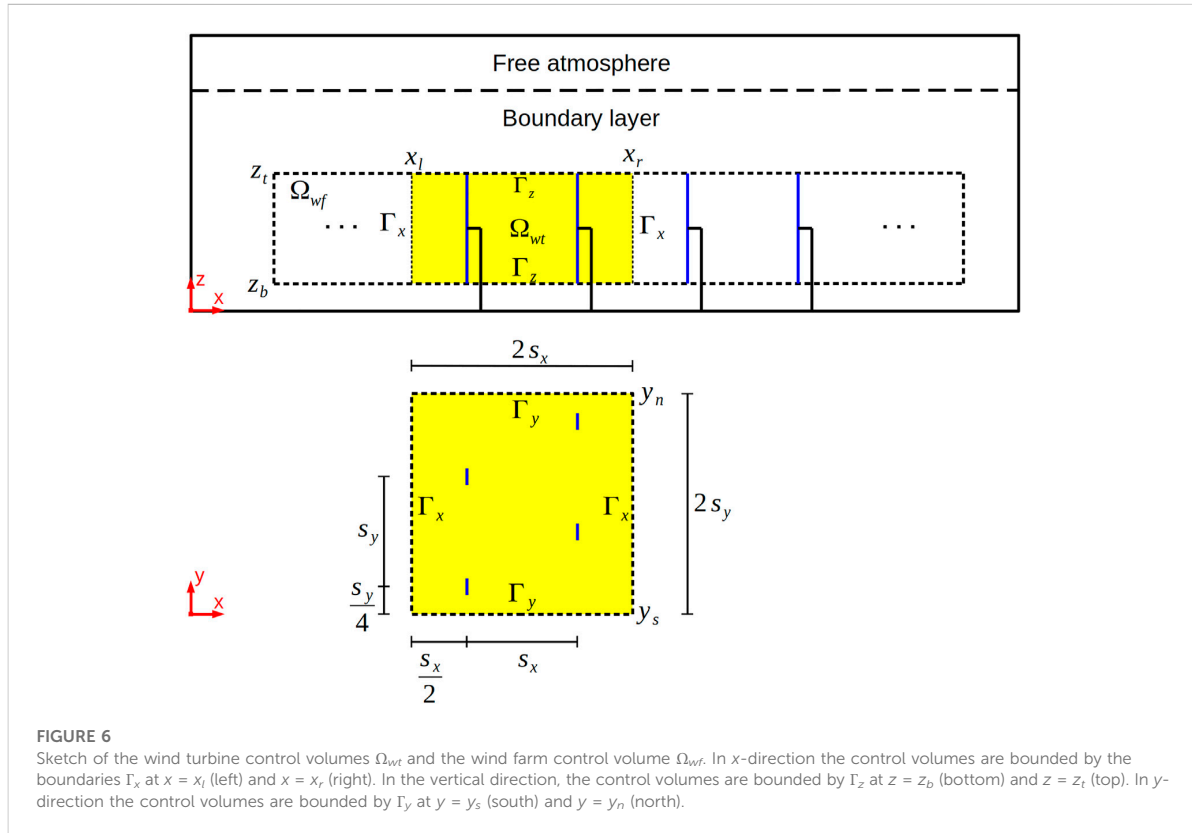


FIGURE 6 Sketch of the wind turbine control volumes Ω_{wt} and the wind farm control volume Ω_{wf} . In x -direction the control volumes are bounded by the boundaries Γ_x at $x = x_l$ (left) and $x = x_r$ (right). In the vertical direction, the control volumes are bounded by Γ_z at $z = z_b$ (bottom) and $z = z_t$ (top). In y -direction the control volumes are bounded by Γ_y at $y = y_s$ (south) and $y = y_n$ (north).

velocity gradients are underestimated, because they are calculated with central differences. Second, the fifth order upwind advection scheme of Wicker and Skamarock (2002) has numerical dissipation, suppressing the magnitude of the smallest eddies, for which the gradients and the dissipation are highest (Maronga et al., 2013). The positive residual is subtracted from the negative dissipation term \mathcal{D} to compensate for the underestimated magnitude of the calculated dissipation.

Instead of calculating terms \mathcal{A} and \mathcal{F} as a volume integral, they can also be calculated as a surface integral over the CV boundaries (Gauss's theorem):

$$\mathcal{A} = \underbrace{\left[\int_{\Gamma_x} (-\bar{u}_1 \bar{E}_k) d\Gamma_x \right]_{x_l}^{x_r}}_{\mathcal{A}_x} + \underbrace{\left[\int_{\Gamma_y} (-\bar{u}_2 \bar{E}_k) d\Gamma_y \right]_{y_s}^{y_n}}_{\mathcal{A}_y} + \underbrace{\left[\int_{\Gamma_z} (-\bar{u}_3 \bar{E}_k) d\Gamma_z \right]_{z_b}^{z_t}}_{\mathcal{A}_z}, \quad (11)$$

$$\mathcal{F} = \underbrace{\left[\int_{\Gamma_x} \left(-\bar{u}_i \bar{u}_i' \bar{u}_i' + \bar{u}_i \tau_{i1} - \frac{1}{2} \bar{u}_i' \bar{u}_i' \bar{u}_i' - \frac{\bar{u}_i' \pi'}{\rho_0} \right) d\Gamma_x \right]_{x_l}^{x_r}}_{\mathcal{F}_x} + \underbrace{\left[\int_{\Gamma_y} \left(-\bar{u}_i \bar{u}_i' \bar{u}_i' + \bar{u}_i \tau_{i2} - \frac{1}{2} \bar{u}_i' \bar{u}_i' \bar{u}_i' - \frac{\bar{u}_i' \pi'}{\rho_0} \right) d\Gamma_y \right]_{y_s}^{y_n}}_{\mathcal{F}_y} + \underbrace{\left[\int_{\Gamma_z} \left(-\bar{u}_i \bar{u}_i' \bar{u}_i' + \bar{u}_i \tau_{i3} - \frac{1}{2} \bar{u}_i' \bar{u}_i' \bar{u}_i' - \frac{\bar{u}_i' \pi'}{\rho_0} \right) d\Gamma_z \right]_{z_b}^{z_t}}_{\mathcal{F}_z}, \quad (12)$$

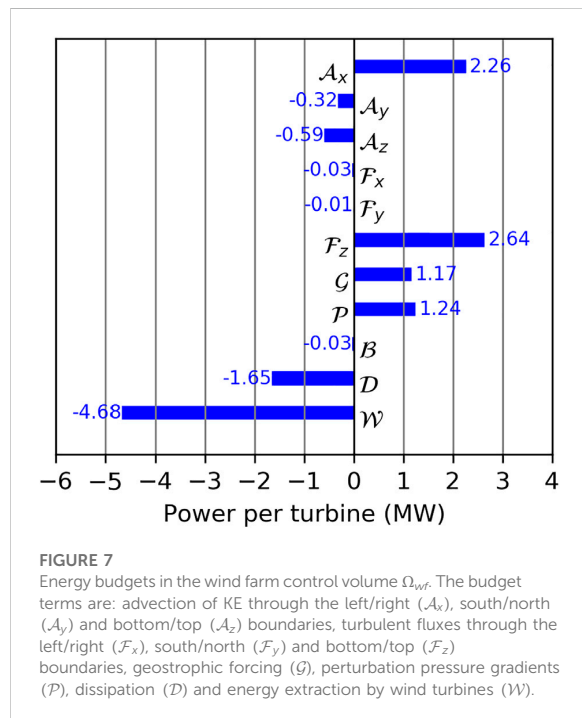


FIGURE 7 Energy budgets in the wind farm control volume Ω_{wf} . The budget terms are: advection of KE through the left/right (\mathcal{A}_x), south/north (\mathcal{A}_y) and bottom/top (\mathcal{A}_z) boundaries, turbulent fluxes through the left/right (\mathcal{F}_x), south/north (\mathcal{F}_y) and bottom/top (\mathcal{F}_z) boundaries, geostrophic forcing (\mathcal{G}), perturbation pressure gradients (\mathcal{P}), dissipation (\mathcal{D}) and energy extraction by wind turbines (\mathcal{W}).

where \mathcal{A}_x , \mathcal{A}_y and \mathcal{A}_z are the advection of KE through the left/right, south/north and bottom/top boundaries, respectively, and \mathcal{F}_x , \mathcal{F}_y and \mathcal{F}_z are turbulent fluxes through the left/right, south/north and bottom/top boundaries, respectively.

3.3.1 Wind farm energy budgets

The energy budgets for the wind farm CV Ω_{wf} are shown in Figure 7. The budget terms of Eq. 9 are converted from $\text{W}\cdot\text{p}^{-1}$ to MW per turbine to make them more meaningful. Inside the CV there is a total energy sink of $\mathcal{D} + \mathcal{W} = -6.33$ MW. 74% of this energy is extracted by the wind turbines ($\mathcal{W} = -4.68$ MW) and 26% is dissipated ($\mathcal{D} = -1.65$ MW). This ratio has also been reported by Maas (2022b) for a semi-infinite wind farm with a turbine spacing of 8 D. The extracted energy is provided by different energy sources. One of this energy sources is the advection of KE through the left/right boundaries of the CV ($\mathcal{A}_x = 2.26$ MW). It is the second largest energy source. However, 14% of \mathcal{A}_x is lost through the south/north boundaries ($\mathcal{A}_y = -0.32$ MW) and 26% of \mathcal{A}_x is lost through the bottom/top boundaries ($\mathcal{A}_z = -0.59$ MW). It is interesting to note that this gives a ratio of 40% between energy loss ($\mathcal{A}_y + \mathcal{A}_z$) and source (\mathcal{A}_x), which is the same ratio reported by Maas (2022b) for $\mathcal{A}_z/\mathcal{A}_x$ for a semi-infinite wind farm for which $\mathcal{A}_y = 0$. Thus, the total advective energy loss is not affected by the south/north boundaries, because the additional loss through these boundaries is compensated by a reduction in \mathcal{A}_z . The energy loss through the south/north boundaries is caused by the crosswise flow divergence in the wind farm that was described in Section 3.1 and can be seen in Figure 3A. The sum of all advection terms gives $\mathcal{A} = 1.35$ MW, which is 21% of the total energy sink ($\mathcal{D} + \mathcal{W}$), confirming that the advection of KE is not the largest energy source for a multi-GW wind farm in contrast to smaller wind farms (Maas, 2022b).

The largest source of KE is the vertical turbulent flux of KE ($\mathcal{F}_z = 2.64$ MW), contributing with 42% to the total energy sink. The fluxes through the lateral boundaries \mathcal{F}_x and \mathcal{F}_y are 2 orders of magnitude smaller than \mathcal{F}_z . The reason is that the surface area of the lateral boundaries is two orders of magnitude smaller than the surface area of the top or bottom boundary ($\Gamma_x \approx \Gamma_y \approx 11 \text{ km}^2$ and $\Gamma_z \approx 2000 \text{ km}^2$). Thus, turbulent fluxes through the left/right and south/north boundaries of the wind farm are negligible for the wind farm energy budget.

The energy input by the geostrophic forcing \mathcal{G} and the mean perturbation pressure gradient \mathcal{P} contribute with 1.17 MW and 1.24 MW, respectively. This corresponds to 18% and 20%, respectively, of the total energy sink. Consequently, \mathcal{A} , \mathcal{G} and \mathcal{P} have approximately the same magnitude ($\approx 20\%$). The energy input by buoyancy forces is negligible small ($\mathcal{B} = -0.03$ MW). This is an expected result for a neutrally stratified boundary layer.

3.3.2 Wind turbine energy budgets

The energy budgets for each wind turbine CV Ω_{wt} are shown in Figure 8. Due to the large spread of values it is difficult to derive quantitative statements from this Figure. However, the Figure shows the qualitative variation along the two dimensions of the wind farm. In general, there is a greater variation along the x -direction than along the y -direction. The variation along the x -direction is discussed in more detail in the next section. Variations along the y -direction occur, e.g., for \mathcal{A}_x , which is greater at the northwestern and southwestern wind farm corners. This correlates with \mathcal{W} ,

i.e., greater wind turbine powers also occur at these wind farm corners. The reason is the variation in the wind direction inside the wind farm: In the central, western part of the wind farm the wind direction is parallel to the turbine rows and thus the turbines in the third turbine column are in the full wake of the first turbine column (remember the staggered configuration). At the wind farm corners the wind direction is different (see Figure 3A) and thus the turbines are not in a full wake. This results in a higher turbine power but also in a larger difference between incoming and outgoing advection of KE and thus a greater \mathcal{A}_x . There is also a correlation between the vertical turbulent fluxes and the wind turbine power, i.e., greater wind turbine powers occur where the fluxes are greater. The energy input by the perturbation pressure gradient \mathcal{P} is greatest at the southeastern wind farm corner, where also the largest pressure gradients occur (see Figure 3B). The energy input by the geostrophic forcing is approximately constant in the entire wind farm.

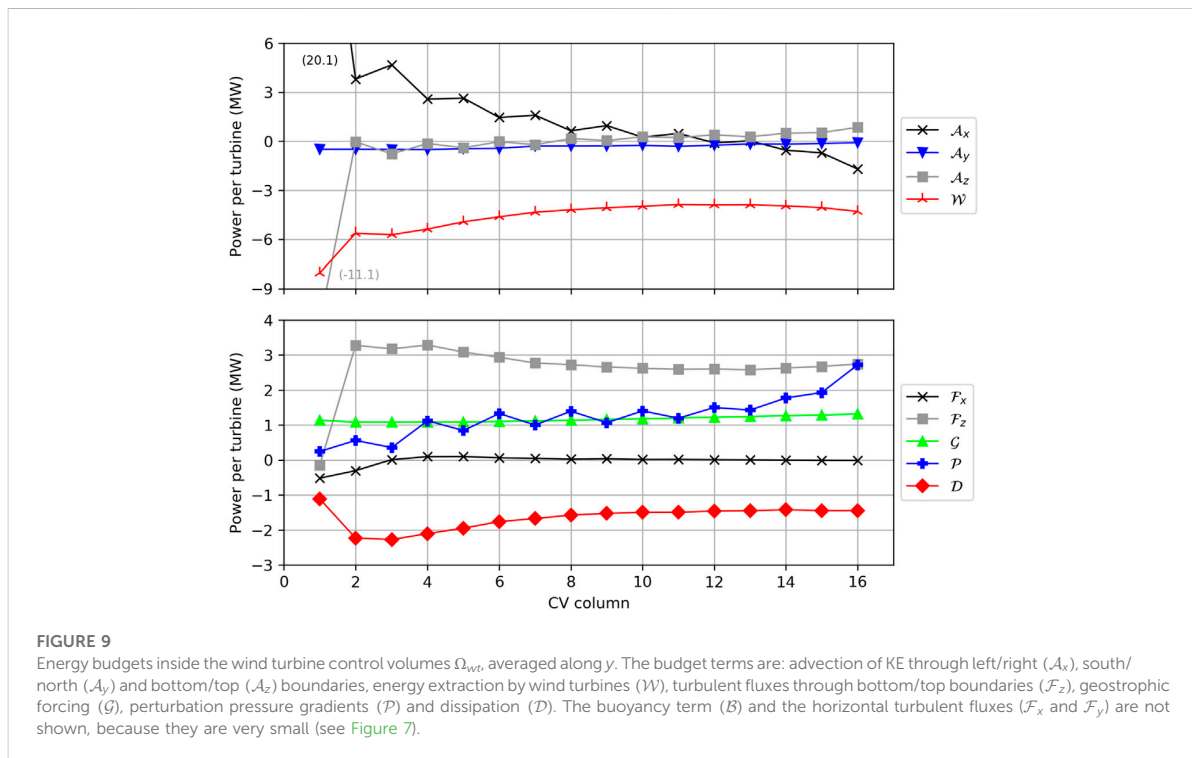
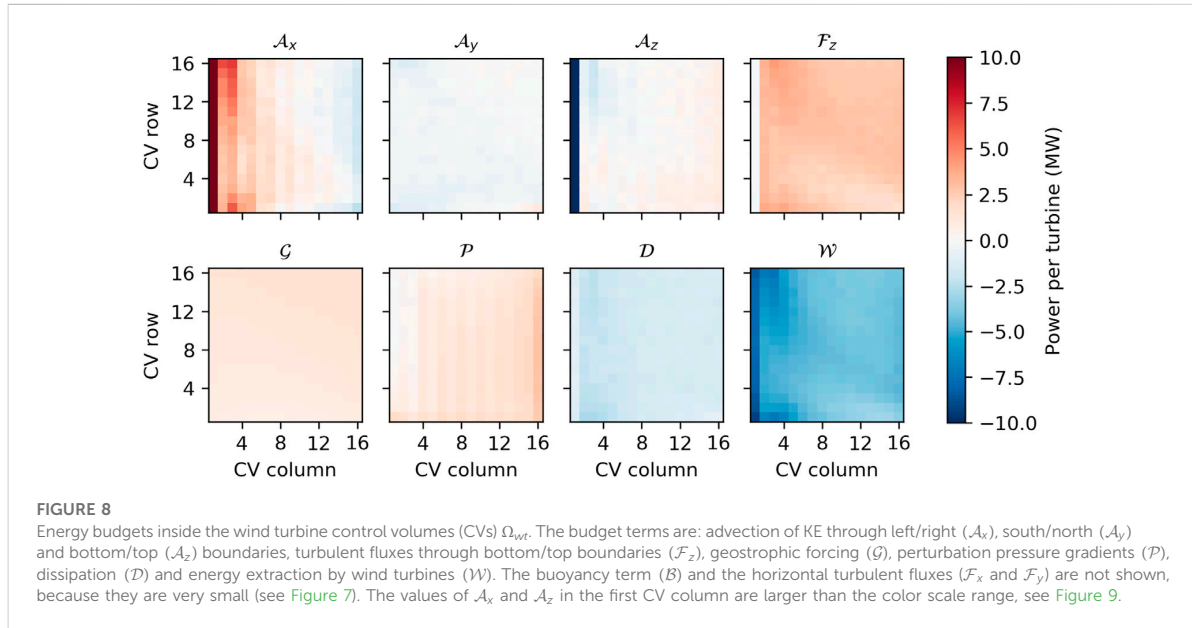
3.3.3 Wind turbine energy budgets averaged by column

To obtain more quantitative statements about the energy budgets inside the wind farm, Figure 9 shows the wind turbine CV energy budgets averaged by column. The terms \mathcal{B} (buoyancy forces) and \mathcal{F}_y (turbulent fluxes at the south/north boundaries) are not shown, because they are smaller than 0.05 MW in every column. In general, the budget terms show the same development as in the semi-infinite wind farm case presented in Maas (2022b).

The advection of KE through the left/right boundaries (Figure 9A) is very large in the first CV (20.1 MW) and becomes negative (-1.7 MW) in the last CV. The flow accelerates in the last CV and thus more KE leaves the CV than it enters, resulting in a net negative KE budget. The streamwise acceleration (divergence) is related to a vertical convergence and thus KE enters the CV through the top boundary ($\mathcal{A}_z = +0.85$ MW). The opposite is the case in the first CV, where KE leaves the top boundary due to an ascending motion ($\mathcal{A}_z = -11.1$ MW). The evolution of \mathcal{A}_x and \mathcal{A}_z shows the same behavior as in semi-infinite wind farms (Allaerts and Meyers, 2017; Maas, 2022b). The advection of KE through the south/north boundaries of the CVs is $\mathcal{A}_y = -0.5$ MW at the first CV and decays to $\mathcal{A}_y = -0.1$ MW at the last CV. Thus, \mathcal{A}_y is not zero as it is for a semi-infinite wind farm like in Allaerts and Meyers (2017) or Maas (2022b), but it has a much smaller magnitude than \mathcal{A}_x . Note that \mathcal{A}_y is negative throughout the entire wind farm, indicating that the flow diverges in the y -direction up to the end of the wind farm and that the flow convergence is only present in the wake (see Figure 3). The development of \mathcal{W} is discussed in Section 3.4.2.

The turbulent fluxes through the left/right boundaries (Figure 9B) are a small sink in the first two CVs ($\mathcal{F}_x = -0.5$ MW), because the outgoing flow contains more TKE than the incoming flow. For the rest of the wind farm \mathcal{F}_x is approximately zero. The vertical turbulent fluxes are slightly negative in the first CV and reach their maximum value of $\mathcal{F}_z = 3.3$ MW in CV 2 and then decay to $\mathcal{F}_z = 2.6$ MW in CV 12.

The energy input by the geostrophic forcing \mathcal{G} increases from 1.1 MW at CV 1–1.3 MW at CV 16. This increase is caused by the counterclockwise wind direction change along x resulting in a larger ageostrophic wind speed component and thus a larger energy input by the geostrophic forcing, as already described by Maas (2022b).



The energy input by the perturbation pressure gradients \mathcal{P} increases from 0.2 MW at CV 1–2.7 MW at CV 16. The large value of \mathcal{P} at the last CV causes the flow to accelerate, causing A_x to decrease and the turbine power \mathcal{W} to increase in magnitude

towards the end of the wind farm. Note that \mathcal{P} shows oscillations with a wavelength of 2 CVs corresponding to 4 turbine spacings ($4s_x = 5.76$ km). These oscillations are related to small scale gravity waves that are triggered at the wind farm leading and trailing edge as

described by Maas (2022b). These gravity waves have a wavelength of approximately 5.3 km and induce pressure oscillations in the boundary layer. The small scale gravity waves are not visible in Figure 5 because their pressure amplitude is much smaller than that of the visible large scale gravity waves.

The dissipation by the SGS model (\mathcal{D}) has the largest magnitude in CV 2 and 3. This is the location where also the largest TI occurs (see Figure 3C).

3.4 Power output and comparison with analytical wake models

3.4.1 Description of the analytical wake models

In the next section the wind turbine power output of PALM is discussed and compared with two analytical wake models, which are described in this section shortly. The two wake models are the NP model (Niayifar and Porté-Agel, 2016) and the Turbulence Optimized Park (TurbOPark) model (Pedersen et al., 2022). These wake models are chosen because they have a Gaussian velocity deficit profile in the wake and because their wake expansion rate depends on the local TI. The Gaussian profile represents the velocity deficit in the wake much more accurately than, e.g., a top-hat profile, as comparisons with LES data and wind tunnel measurements have shown (Bastankhah and Porté-Agel, 2014). Accounting for the local TI, i.e., the sum of the ambient TI and the turbine generated TI, results in a more realistic wake expansion rate than accounting for only the ambient TI (Lissaman, 1979; Nygaard et al., 2022). Both wake models are based on the momentum-conserving velocity deficit model for a single turbine wake proposed by Bastankhah and Porté-Agel (2014). For each wind turbine there is an image wind turbine mirrored at $z = 0$ to account for the effect of the ground. The wake models differ in the wake superposition principle and the turbulence model.

In the NP model the superposition of wakes is performed by a linear sum of the velocity deficits, which conserves the momentum (Lissaman, 1979; Bastankhah and Porté-Agel, 2014). The turbine generated turbulence is modeled according to Crespo and Hernandez (1996). Note that this model is only valid for streamwise TIs between 7% and 14% and that the first 2 turbine columns are exposed to the ambient streamwise TI, which is only 4.3%. For a given location only the TI caused by the nearest upstream turbine is considered and no superposition is performed (Bastankhah and Porté-Agel, 2014, p. 5).

In the TurbOPark model the superposition of wakes is performed by a quadratic sum of the velocity deficits, which conserves the kinetic energy (Katic et al., 1987; Nygaard et al., 2022). The turbine generated turbulence is modeled according to Frandsen (2007). The superposition of the ambient TI with the turbine generated TI of all wakes at a given location is performed by a quadratic sum, which is a TKE- or variance-conserving method.

The computations for the wake models are performed with the open source wind farm simulation tool PyWake (Pedersen et al., 2019). Meteorological input parameters are the mean hub height wind speed ($9 \text{ m} \cdot \text{s}^{-1}$), the wind shear exponent (0.088), the ambient streamwise TI at hub height (4.3%) and the wind direction (270°). Wind turbine specific input parameters are the rotor diameter, the hub height, the coordinates of the wind turbines and the thrust and

power coefficients at different wind speeds, that are available at the data repository given in Gaertner et al. (2020).

3.4.2 Results of the wake model comparison

The electrical wind turbine power output of PALM and the two wake models is shown in Figure 10. There are large differences in the qualitative distribution of the turbine power between PALM and the wake models. For the TurbOPark model, the turbine power only varies along the turbine rows and is constant inside a turbine column. For the NP model the turbine power is larger at the southern and northern wind farm boundaries than inside the wind farm. This effect is largest for the most downstream located turbines and is caused by the linear superposition method for the velocity deficit but also by the different turbulence model used in the NP model. However, the largest variation inside a turbine column is present in PALM. In the first column, the highest turbine power occurs at the most northern and southern turbines, because the blockage effect (or pressure) is smallest there (see Figure 3B). But also for further downstream located columns the power variation is very large, e.g., 3.8 MW–6.2 MW in column 3. This large variation is caused by the spatial variation of the wind direction inside the wind farm that results in a full-wake situation for a row-parallel flow and to a partial or no-wake situation for other wind directions (see Figure 3A). Consequently the smallest turbine power occurs at row 1, column 23, where the wind direction is parallel to the turbine rows.

Because a quantitative comparison between the models is difficult with the color diagram shown in Figure 10, the column-wise averaged wind turbine power is shown in Figure 11. The figure shows the results of two different PyWake simulations. In Figure 11A the hub height wind speed is set to the hub height inflow wind speed in PALM ($v_1 = 9.00 \text{ m} \cdot \text{s}^{-1}$). In Figure 11B the hub height wind speed is set to the wind speed 2.5 D upstream of the first turbine column averaged along the wind farm width in PALM ($v_2 = 7.94 \text{ m} \cdot \text{s}^{-1}$) to account for the global blockage effect.

In PALM, the mean turbine power in the first column is 6.2 MW. This is 32% less than the power of the IEA 15 MW reference wind turbine at a hub height wind speed of $9.0 \text{ m} \cdot \text{s}^{-1}$ (9.1 MW). The reason is the global blockage effect, that reduces the mean hub height wind speed in the first column by approximately $1 \text{ m} \cdot \text{s}^{-1}$. In column 3 and 4 the mean turbine power has dropped to approximately 4.5 MW, because most of the turbines are in the wake of a turbine in column 1 or 2. Some turbines, however, are not in a full wake, as discussed above and thus there is a large spread between the minimum and maximum turbine power in these columns. Further downstream, the power drops further due to a decrease in the horizontal advection of KE \mathcal{A}_x and a decrease in the vertical turbulent fluxes \mathcal{F}_z (see Figure 9). At column 20 the mean turbine power has reached a minimum of 3.1 MW. Further downstream the mean turbine power increases to 3.6 MW at the last column. This increase in power is caused by an increase in the energy input by the pressure gradient \mathcal{P} (see Figure 9). The total wind farm power is $P_{wf,PALM} = 3.77 \text{ GW}$, resulting in a wind farm efficiency of:

$$\eta_{wf,PALM} = \frac{P_{wf,PALM}}{N_{wt} P_{ref}} = \frac{3.77 \text{ GW}}{1024 \times 9.1 \text{ MW}} = 40.5 \%. \quad (13)$$

In Figure 11A the mean turbine power in the first two columns of the NP and TurbOPark model is 9.1 MW, which is the power of the IEA 15 MW reference wind turbine at a hub height wind speed

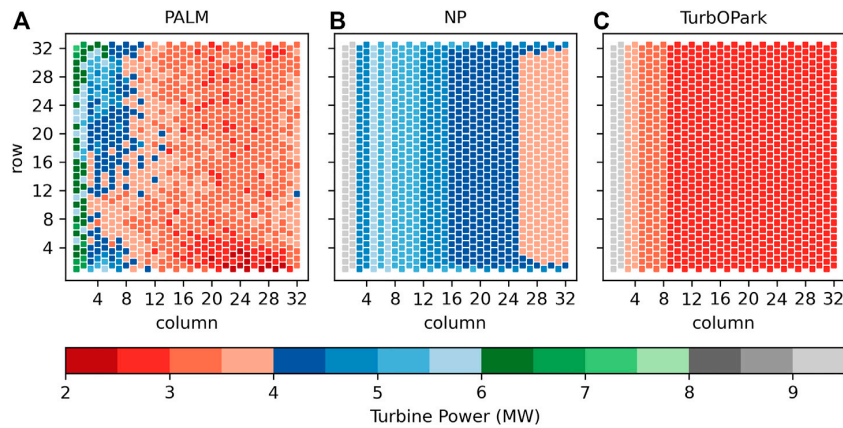


FIGURE 10 Wind turbine power of the LES model PALM (A), the Niayifar and Porté-Agel model (B) and the TurbOPark model (C). For PALM, the power is averaged over the last 4 h of the main simulation.

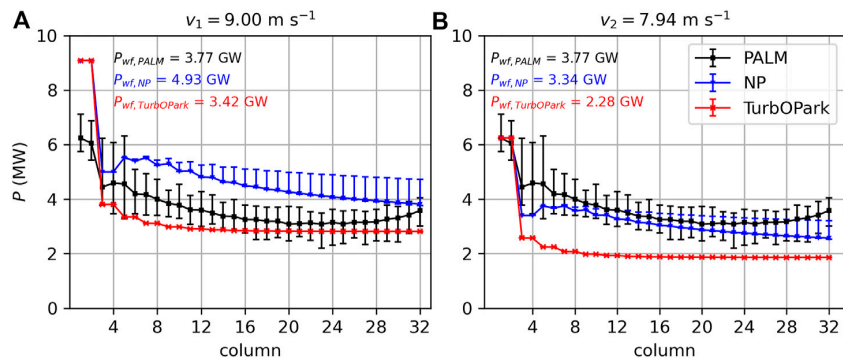


FIGURE 11 Wind turbine power of the LES model PALM, the Niayifar and Porté-Agel model (NP) and the TurbOPark model. The markers represent the column-wise averaged power and the error bars represent the maximal and minimal power in the respective wind farm column. In (A) the reference wind speed for the wake models is set to the inflow wind speed at hub height of the LES ($9.00 \text{ m} \cdot \text{s}^{-1}$). In the (B) the reference wind speed is reduced to $7.94 \text{ m} \cdot \text{s}^{-1}$, which is the wind speed $2.5 D$ upstream of the first column averaged along the wind farm width in PALM. The total wind farm powers (P_{wf}) are also given.

of $9.0 \text{ m} \cdot \text{s}^{-1}$. This is 47% more than in PALM because the NP and TurbOPark model do not account for the global blockage effect. In PyWake it is possible to account for the local blockage effect, i.e., the flow deceleration upstream of each rotor disc. However, using this local blockage model affects the wind farm power by less than 0.5%. Thus, the magnitude of the global blockage effect is approximately two orders of magnitude greater than the sum of the local blockage effects of all wind turbines. Similar results have also been reported by Centurelli et al. (2021).

In Figure 11B, where the hub height wind speed for the wake models is reduced to $v_2 = 7.94 \text{ m} \cdot \text{s}^{-1}$, the turbine power in the first column of the wake models agrees with that of PALM. Thus, the following discussion is based on Figure 11B.

For the NP model the turbine power drops to 3.4 MW in column 3 and 4 and then increases to 3.7 MW in column 7 due to the increases TI generated by the upstream turbines. From there on the turbine power decreases monotonically up to the end of the wind farm, where it reaches 2.6 MW. In the bulk of the wind farm the NP model underestimates the turbine power by only 7%. Larger differences of up to -28% occur towards the end of the wind farm. The total wind farm power output is $P_{wf,NP} = 3.34 \text{ GW}$, which is 11% less than that of PALM and corresponds to a wind farm efficiency of $\eta_{wf,NP} = 35.8\%$.

For the TurbOPark model the turbine power drops to 2.6 MW in column 3 and 4. Due to the quadratic superposition of the velocity deficits, the turbine power reaches an equilibrium value of 1.9 MW

at approximately column 16. This results in deviations of up to -51% relative to PALM in column 5. The total wind farm power output is $P_{wf,TurbOPark} = 2.28$ GW, which is 40% less than that of PALM and corresponds to a wind farm efficiency of $\eta_{wf,TurbOPark} = 24.5\%$.

What are the reasons for these large discrepancies between the results of the LES and the wake models? As described in the previous section, the wake models are momentum-conserving (or energy-conserving in case of the wake superposition in the TurbOPark model). That means that there are no momentum or energy sinks except the wind turbines itself. There are also no momentum or energy sources except the advection of KE into the wind farm. But, as the energy budget analysis of the LES shows, there are KE sources and sinks that are at least equally important than the advection of KE. The sources are the energy input by the geostrophic forcing (\mathcal{G}) and by the perturbation pressure gradients (\mathcal{P}). The vertical turbulent fluxes (\mathcal{F}_z) are also an energy source but they are part of the wake expansion process of the wake models (expansion and speed recovery through turbulent mixing). There are also important energy sinks like the loss of KE through the northern and southern wind farm boundaries \mathcal{A}_y , the bottom and top wind farm boundaries (\mathcal{A}_z) and the loss of KE by dissipation (\mathcal{D}). Because the wake models do not consider these energy sources and sinks, the wake models overestimate or underestimate the total wind farm power, depending on which reference hub height wind speed is chosen.

The LES results show that, if all relevant physics are modeled, many complex flow effects occur in a wind farm of this size. These relevant physics are, e.g., the consideration of Coriolis, pressure and buoyancy forces resulting in flow effects like gravity waves, global blockage effect, flow deflection and flow acceleration. The complexity of the flow causes a large spread in the wind turbine power, as shown in Figure 10A. The investigated wake models neglect the above named physics. This seems to be a valid simplification for small wind farms in which the named flow effects do not occur. But for large, multi-gigawatt wind farms as in this study this simplification is not valid any more. The analytical wake models thus underestimate the variation of the turbine power inside the turbine columns and underestimate the total wind farm power by up to 40% .

Improvements could be achieved by taking some of the neglected physics into account. The largest deviations occur at the first and last turbine column and are caused by the neglect of the perturbation pressure distribution. The perturbation pressure distribution is responsible for the global blockage effect and the flow acceleration at the end of the wind farm. Thus, taking these effects into account will probably significantly improve the large wind farm power prediction capability of the investigated wake models. Two tasks have to be solved to include these effects in to the wake models: First, modeling of the gravity wave induced pressure distribution in the wind farm. Second, modeling the effect of this pressure distribution on the velocity field, e.g., by applying Bernoulli's principle. Information for modeling gravity wave induced pressure gradients in wind farms is provided by Smith (2009), Allaerts et al. (2018), Allaerts and Meyers (2019), Lanzilao and Meyers (2021) and Devesse et al. (2022). A wake model that considers the effect of streamwise pressure gradients was recently proposed by Dar and Porté-Agel (2022). It is designed for topography induced pressure gradients but it might

also be suitable for gravity wave induced pressure gradients. Unfortunately, this model is not part of PyWake and could not be tested in this study.

4 Discussion

In this study the results of an LES of a 15 GW wind farm are presented and compared with analytical wake models. One aim of this study is to investigate differences between the flow field of the finite-size wind farm setup as used in this study with a semi-infinite wind farm setup as used in the study of Maas (2022b). The results show that the finite-size wind farm setup causes an even more complex flow than the semi-infinite wind farm setup. Additional effects are the crosswise flow divergence in the wind farm and the crosswise flow convergence in the wind farm wake. The semi-infinite wind farm setup of Maas (2022b) generates supergeostrophic wind speeds in the wake, which do not occur for the finite-size wind farm in this study. Thus, it can be concluded that using a semi-infinite wind farm setup for multi-gigawatt wind farms suppresses or amplifies important flow features that occur in the more realistic finite-size wind farm setup.

The energy budget analysis shows that there is an additional loss of KE through the southern and northern wind farm boundaries that do not exist for a semi-infinite wind farm setup. However, this additional loss is compensated by a reduction of the KE loss by advection through the bottom and top wind farm boundaries. The turbulent flux of KE through all lateral wind farm boundaries is two orders of magnitude smaller than the turbulent fluxes through the bottom and top wind farm boundaries and can thus be neglected.

The second aim of this study is to compare the wind turbine power output of the LES model PALM with two analytical wake models: The NP model (Niayifar and Porté-Agel, 2016) and the TurbOPark model (Pedersen et al., 2022). The comparison shows that there are large discrepancies between the wind farm power predicted by the wake models and by PALM. In the first turbine column the wake models overestimate the power by 47% , because they do not account for the global blockage effect. If the reference hub height wind speed of the wake models is reduced to account for the global blockage effect, then they underestimate the wind farm power by 11% and 40% for the NP and TurbOPark model, respectively. Due to the spatial variability of the wind direction in PALM, there is a large variation in the turbine power throughout the wind farm. This variability is not present in the wake models.

The large discrepancies between the results of PALM and the wake models occur because the wake models neglect most of the relevant physical processes. This has two consequences: First, the flow field do not feature the flow complexity, e.g., the wind direction variability, that the results of the LES reveal. Second, important energy sources and sinks, such as the energy input by the geostrophic forcing or the perturbation pressure gradients, are neglected. This seems to be a valid simplification for small wind farms in which the named flow effects do not occur and the largest energy source is the advection of KE. But for large, multi-gigawatt wind farms as in this study this simplification is not valid any more, because other energy sources and sinks become relevant. Improvements could be achieved by taking some of the neglected physics, especially the pressure distribution, into account.

The LES results provide interesting and valuable insights into the flow of potential large offshore wind farms. It should be noted, however, that the results are based on a very idealized simulation setup that might deviate from reality significantly. For example, stationarity, barotropic conditions, a constant wind and temperature stratification profile in the free atmosphere and a homogeneous surface are assumed. A deviation from these idealized conditions might weaken or strengthen the described flow effects. The wind farm blocks 1/3 of the domain width, so that the magnitude of the pressure gradients and the wake deflection might still be overestimated. Additionally, only one meteorological and wind farm setup is investigated. A different boundary layer height, stability, surface roughness or turbine arrangement may change the results. Further research is needed to quantify the effect of the named variations.

Data availability statement

The datasets presented in this study can be found in online repositories. The names of the repository/repositories and accession number(s) can be found below: <https://doi.org/10.25835/39jgn8ac> Research Data Repository of the Leibniz University Hannover.

Author contributions

The author confirms being the sole contributor of this work and has approved it for publication.

References

- Allaerts, D., and Meyers, J. (2017). Boundary-layer development and gravity waves in conventionally neutral wind farms. *J. Fluid Mech.* 814, 95–130. doi:10.1017/jfm.2017.11
- Allaerts, D., and Meyers, J. (2019). Sensitivity and feedback of wind-farm-induced gravity waves. *J. Fluid Mech.* 862, 990–1028. doi:10.1017/jfm.2018.969
- Allaerts, D., Broucke, S. V., van Lipzig, N., and Meyers, J. (2018). Annual impact of wind-farm gravity waves on the Belgian-Dutch offshore wind-farm cluster. *J. Phys. Conf. Ser.* 1037, 072006. doi:10.1088/1742-6596/1037/7/072006
- Bastankhah, M., and Porté-Agel, F. (2014). A new analytical model for wind-turbine wakes. *Renew. Energy* 70, 116–123. doi:10.1016/j.renene.2014.01.002
- BSH (2022). *Entwurf flächennutzungsplan*. Tech. rep. Hamburg: Bundesamt für Seeschifffahrt und Hydrographie.
- Centurelli, G., Vollmer, L., Schmidt, J., Dörenkämper, M., Schröder, M., Lukassen, L. J., et al. (2021). Evaluating global blockage engineering parametrizations with LES. *J. Phys. Conf. Ser.* 1934, 012021. doi:10.1088/1742-6596/1934/1/012021
- Crespo, A., and Hernandez, J. (1996). Turbulence characteristics in wind-turbine wakes. *J. Wind Eng. Indust. Aerodyn.* 61, 71–85. doi:10.1016/0167-6105(95)00033-X
- Dar, A. S., and Porté-Agel, F. (2022). An analytical model for wind turbine wakes under pressure gradient. *Energies* 15, 5345. doi:10.3390/en15155345
- Deardorff, J. W. (1980). Stratocumulus-capped mixed layers derived from a three-dimensional model. *Boundary-Layer Meteorol.* 18, 495–527. doi:10.1007/BF00119502
- Devesse, K., Lanzilao, L., Jamaer, S., Van Lipzig, N., and Meyers, J. (2022). Including realistic upper atmospheres in a wind-farm gravity-wave model. *Wind Energy Sci.* 7, 1367–1382. doi:10.5194/wes-7-1367-2022
- Dörenkämper, M., Witha, B., Steinfeld, G., Heinemann, D., and Kühn, M. (2015). The impact of stable atmospheric boundary layers on wind-turbine wakes within offshore wind farms. *J. Wind Eng. Indust. Aerodyn.* 144, 146–153. doi:10.1016/j.jweia.2014.12.011
- Frandsen, S. T. (2007). *Turbulence and turbulence-generated structural loading in wind turbine clusters*. Ph.D. thesis. Technical University of Denmark.
- Frederiksen, M., de Croo, A., Rutte, M., and Scholz, O. (2022). *The esbjerg declaration*. Tech. rep. The Federal Ministry for Economic Affairs and Climate Action of Germany.

Funding

This work was funded by the Federal Maritime and Hydrographic Agency (BSH, Grant No. 10044580) and supported by the North German Supercomputing Alliance (HLRN).

Acknowledgments

I thank my supervisor Siegfried Raasch for guiding the manuscript preparation.

Conflict of interest

The author declares that the research was conducted in the absence of any commercial or financial relationships that could be construed as a potential conflict of interest.

Publisher's note

All claims expressed in this article are solely those of the authors and do not necessarily represent those of their affiliated organizations, or those of the publisher, the editors and the reviewers. Any product that may be evaluated in this article, or claim that may be made by its manufacturer, is not guaranteed or endorsed by the publisher.

- Gaertner, E., Rinker, J., Sethuraman, L., Zahle, F., Anderson, B., Barter, G., et al. (2020). *Definition of the IEA wind 15-megawatt offshore reference wind turbine*. Tech. rep. Golden, CO: National Renewable Energy Laboratory.
- Katic, I., Højstrup, J., and Jensen, N. (1987). A simple model for cluster efficiency. *Eur. wind energy Assoc. Conf. Exhib.* 1, 407–410.
- Klemp, J. B., and Lilly, D. K. (1978). Numerical simulation of hydrostatic mountain waves. *J. Atmos. Sci.* 35, 78–107. doi:10.1175/1520-0469(1978)035<0078:NSOHW>2.0.CO;2
- Krüger, S., Steinfeld, G., Kraft, M., and Lukassen, L. J. (2022). Validation of a coupled atmospheric-aeroelastic model system for wind turbine power and load calculations. *Wind Energy Sci.* 7, 323–344. doi:10.5194/wes-7-323-2022
- Lanzilao, L., and Meyers, J. (2021). Set-point optimization in wind farms to mitigate effects of flow blockage induced by atmospheric gravity waves. *Wind Energy Sci.* 6, 247–271. doi:10.5194/wes-6-247-2021
- Lanzilao, L., and Meyers, J. (2022). Effects of self-induced gravity waves on finite wind-farm operations using a large-eddy simulation framework. *J. Phys. Conf. Ser.* 2265, 022043. doi:10.1088/1742-6596/2265/2/022043
- Lissaman, P. B. (1979). Energy effectiveness of arbitrary arrays of wind turbines. *J. energy* 3, 323–328. doi:10.2514/3.62441
- Maas, O., and Raasch, S. (2022). Wake properties and power output of very large wind farms for different meteorological conditions and turbine spacings: A large-eddy simulation case study for the German Bight. *Wind Energy Sci.* 7, 715–739. doi:10.5194/wes-7-715-2022
- Maas, O. (2022a). *LES of a 15 GW wind farm*. [Dataset]. doi:10.25835/39jgn8ac
- Maas, O. (2022b). Preprint: From gigawatt to multi-gigawatt wind farms: Wake effects, energy budgets and inertial gravity waves investigated by large-eddy simulations. *Wind Energy Sci. Discuss.* 2022, 1–31. doi:10.5194/wes-2022-63
- Maronga, B., Moene, A. F., van Dinter, D., Raasch, S., Bosveld, F. C., and Gioli, B. (2013). Derivation of structure parameters of temperature and humidity in the convective boundary layer from large-eddy simulations and implications for the interpretation of scintillometer observations. *Boundary-Layer Meteorol.* 148, 1–30. doi:10.1007/s10546-013-9801-6

- Maronga, B., Banzhaf, S., Burmeister, C., Esch, T., Forkel, R., Fröhlich, D., et al. (2020). Overview of the PALM model system 6.0. *Geosci. Model Dev.* 13, 1335–1372. doi:10.5194/gmd-13-1335-2020
- Miller, M. J., and Thorpe, A. J. (1981). Radiation conditions for the lateral boundaries of limited-area numerical models. *Q. J. R. Meteorol. Soc.* 107, 615–628. doi:10.1002/qj.49710745310
- Moeng, C.-H., and Wyngaard, J. C. (1988). Spectral analysis of large-eddy simulations of the convective boundary layer. *J. Atmos. Sci.* 45, 3573–3587. doi:10.1175/1520-0469(1988)045<3573:SAOLES>2.0.CO;2
- Munters, W., Meneveau, C., and Meyers, J. (2016). Shifted periodic boundary conditions for simulations of wall-bounded turbulent flows. *Phys. Fluids* 28, 025112. doi:10.1063/1.4941912
- Niayifar, A., and Porté-Agel, F. (2016). Analytical modeling of wind farms: A new approach for power prediction. *Energies* 9, 741–813. doi:10.3390/en9090741
- Nygaard, N. G., Poulsen, L., Svensson, E., and Pedersen, J. G. (2022). Large-scale benchmarking of wake models for offshore wind farms. *J. Phys. Conf. Ser.* 2265, 022008. doi:10.1088/1742-6596/2265/2/022008
- Orlanski, I. (1976). A simple boundary condition for unbounded hyperbolic flows. *J. Comput. Phys.* 21, 251–269. doi:10.1016/0021-9991(76)90023-1
- Pedersen, M. M., van der Laan, P., Friis-Møller, M., Rinker, J., and Réthoré, P.-E. (2019). *DTUWindEnergy/PyWake: PyWake*. [Dataset]. doi:10.5281/zenodo.2562662
- Pedersen, J. G., Svensson, E., Poulsen, L., and Nygaard, N. G. (2022). Turbulence Optimized Park model with Gaussian wake profile. *J. Phys. Conf. Ser.* 2265, 022063. doi:10.1088/1742-6596/2265/2/022063
- Porté-Agel, F., Bastankhah, M., and Shamsoddin, S. (2020). Wind-turbine and wind-farm flows: A review. *Boundary-Layer Meteorol.* 174, 1–59. doi:10.1007/s10546-019-00473-0
- Saiki, E. M., Moeng, C.-H., and Sullivan, P. P. (2000). Large-eddy simulation of the stably stratified planetary boundary layer. *Boundary-Layer Meteorol.* 95, 1–30. doi:10.1023/A:1002428223156
- Smith, R. B. (2009). Gravity wave effects on wind farm efficiency. *Wind Energy* 13, 449–458. doi:10.1002/we.366
- Steinfeld, G., Witha, B., Dörenkämper, M., and Gryschka, M. (2015). Hochauflösende Large-Eddy-Simulationen zur Untersuchung der Strömungsverhältnisse in Offshore-Windparks. *promet - Meteorol. Fortbild.* 39, 163–180.
- Stevens, R. J., Gayme, D. F., and Meneveau, C. (2016). Effects of turbine spacing on the power output of extended wind-farms. *Wind Energy* 19, 359–370. doi:10.1002/we.1835
- Taylor, J. R., and Sarkar, S. (2007). Internal gravity waves generated by a turbulent bottom Ekman layer. *J. Fluid Mech.* 590, 331–354. doi:10.1017/S0022112007008087
- Wicker, L. J., and Skamarock, W. C. (2002). Time-splitting methods for elastic models using forward time schemes. *Mon. Weather Rev.* 130, 2088–2097. doi:10.1175/1520-0493(2002)130<2088:TSMFEM>2.0.CO;2
- Witha, B., Steinfeld, G., Dörenkämper, M., and Heinemann, D. (2014). Large-eddy simulation of multiple wakes in offshore wind farms. *J. Phys. Conf. Ser.* 555, 012108. doi:10.1088/1742-6596/555/1/012108
- Wu, Y.-T., and Porté-Agel, F. (2011). Large-eddy simulation of wind-turbine wakes: Evaluation of turbine parametrisations. *Boundary-Layer Meteorol.* 138, 345–366. doi:10.1007/s10546-010-9569-x
- Wu, K. L., and Porté-Agel, F. (2017). Flow adjustment inside and around large finite-size wind farms. *Energies* 10, 2164–2169. doi:10.3390/en10122164
- Zhang, M., Arendshorst, M. G., and Stevens, R. J. (2019). Large eddy simulations of the effect of vertical staggering in large wind farms. *Wind Energy* 22, 189–204. doi:10.1002/we.2278

6 Summary and open research questions

6.1 Summary

The aim of this thesis was to study the power output and flow effects of multi-gigawatt wind farms using large-eddy simulations (LES). The results of this thesis are summarized and concluded by answering the questions of the introduction section:

How to design an LES setup that is suitable for simulating the flow in large wind farms? It can be concluded that an LES setup for large wind farms has to fulfill more requirements than a setup for small wind farms. Gravity waves, global blockage effect and flow divergence are only represented realistically if suitable boundary conditions and domain sizes are used. For example, to avoid the reflection of gravity waves at the domain top, a domain height of at least one wavelength plus a Rayleigh damping layer of similar thickness is required. To minimize interactions between the blockage effect and the turbulence recycling plane a large distance of approximately 100 km between the inflow and the wind farm is required. The second article used the semi-infinite wind farm setup, and the results showed that the wind farm triggers an inertial oscillation. This oscillation did not occur in the third article, which uses the finite wind farm setup. Additionally, flow divergence and convergence occurred in the third article but not in the second article. Thus it can be concluded that for large wind farm studies the finite wind farm setup should be used in the future.

What are the fundamental differences between the flow in small (sub-gigawatt) and large (multi-gigawatt) wind farms and why do they occur? One fundamental difference between small (sub-gigawatt) and large (multi-gigawatt) wind farms is their different length scale. Small wind farms have a size on the order of 10 km, and large wind farms have a size on the order of 100 km. This has several implications. First, the Rossby number of large wind farms is small enough for Coriolis effects to appear. This results in a significant counterclockwise flow deflection in the wind farm and the wake in the order of 10° , which is significantly more than the deflection angles reported by other studies. Second, due to the larger number of wind turbines in the streamwise direction, there is a larger speed deficit inside the wind farm and the boundary layer (BL). This results in a larger vertical displacement of the inversion layer (IL) and thus also to larger amplitudes of the gravity waves in the overlying free atmosphere. Consequently, the blockage effect is also greater for larger wind farms. In the second article, speed deficits of 8 % for the large wind farm and 5 % for the small wind farm were observed. The vertical IL displacement also causes an acceleration of the overlying flow resulting in a clockwise deflection due to an increased Coriolis force. This clockwise deflection has never been reported before. The third article, which uses the finite wind farm setup, has shown that the flow in large wind farms does not only diverge in the vertical direction but also in the crosswise direction, resulting in a wind direction change of several degrees at the wind farm corners. In the wake, the flow converges in the vertical and crosswise direction. These effects have not been observed in other wind farm studies due to the limited wind farm size or the use of the semi-infinite wind farm setup. The wakes of large wind farms are, in general, much longer (in the order of 100 km) than the wakes of small wind farms. The reason is that large wind farms have already extracted a large portion of the kinetic energy in the BL, so that the most important wake recovery process, the vertical turbulent flux of kinetic energy, is small. The wake recovery is mainly driven by the geostrophic forcing, which is a much weaker force. Results of the first and second

article have shown that, in terms of turbulence intensity, the wake length is in the order of 10 km and is independent of the wind farm size. The wind farm length independence of the turbulent wake is a new finding that has not been reported by other studies.

How does the wind farm wake of a large wind farm depend on the stability and the boundary layer height? Wakes of small wind farms are shorter for convective boundary layers (CBLs) and longer for stable boundary layers (SBLs). However, this statement could not be confirmed for large wind farms, as investigated in the first article. The wind speed deficit and the wake length were greater in the CBL case than in the neutral boundary layer (NBL) case. This effect could be explained by the greater wind shear in the NBL case, which causes a greater vertical turbulent energy flux and thus faster wake decay. For the SBL case, the speed deficit inside the wind farm is larger than in the NBL and CBL cases, but the wake has approximately the same length due to a much faster speed recovery. The speed recovery is driven by a negative pressure gradient induced by gravity waves. These results suggest that the stability has no direct impact on the wake length of large wind farms. The BL height, however, has a significant influence on the wake length of large wind farms as shown by the two CBL cases in the first article. A thicker BL results in a shorter wake due to a larger vertical kinetic energy flux in the wake. For small wind farms, the wake length is nearly independent of the BL height because the internal boundary layer does not reach the IL. The anticlockwise flow deflection is larger for smaller BLs due to a greater wind speed deficit and thus greater reduction in Coriolis force. Shallower BLs cause a greater wind speed deficit and consequently a larger IL displacement, larger gravity wave amplitudes and a stronger blockage effect, which is consistent with the findings of other studies with smaller wind farms.

Which wind farm efficiencies can be achieved in large wind farms and how do they depend on the stability, boundary layer height and turbine spacing? The results of the first article show that wind farm efficiencies of large (multi-gigawatt) wind farms are significantly smaller than wind farm efficiencies of small (sub-gigawatt) wind farms. For large wind farms in a NBL, the wind farm efficiency can be as low as 41 %, if the turbine spacing is as small as 5D, in contrast to 66 % for a small wind farm. The variation of the BL height in the CBL cases has shown that the wind farm efficiency of small wind farms is nearly independent of the BL height (88 % vs. 86 % for a doubling of the BL height). In contrast, the wind farm efficiency of large wind farms shows a clear dependence on the BL height (64 % vs. 54 %). The effect of stability on the wind farm efficiency could not be clearly stated because also other parameters vary if the stability changes. The CBL-700 and NBL-700 cases in the first article have approximately the same BL height, but in the NBL case the wind shear is greater, resulting in higher wind speeds in the bulk of the BL. The SBL and NBL cases have very different BL heights and can thus also not be directly compared.

What are the most important energy sources and sinks in a large wind farm? Both energy budget analyses performed in this thesis are unique and provide interesting insights into the energy budgets of large wind farms. The energy budget analysis in the second article compares the energy budgets in small and large wind farms systematically for the first time. The energy budget analysis in the third article investigates a multi-gigawatt finite-size wind farm for the first time. The results have shown that the advection of kinetic energy by the mean flow is a large energy source for small wind farms but plays a minor role for large wind farms. The reason is that the inflow of kinetic energy spreads over more turbines and that a large amount of kinetic energy leaves the wind farm due to the acceleration in the exit region. The largest energy source for large wind farms is the vertical turbulent flux of kinetic energy. The energy input by turbulent fluxes through the lateral boundaries of the wind farm is negligibly small. The control volume of a large wind farm has a higher

volume to surface area ratio so that volume sources like the energy input by the geostrophic forcing become more dominant. The energy input by the geostrophic forcing is enhanced by the counterclockwise deflection of the flow, which results in a higher ageostrophic wind speed component. Although the gravity wave induced pressure amplitude and the blockage effect are larger for the large wind farm, the pressure gradient and thus also its energy input is smaller for the large wind farm due to the greater wind farm length.

How do analytical wake models perform for large wind farms and how can they be improved? In this thesis analytical wake models have been compared with LES results of a multi-gigawatt wind farm for the first time. The results have shown that even advanced analytical wake models can not accurately predict the power output of a 15 GW wind farm. Deviations in the wind farm power output of up to 40 % between the wake models and the LES results were found. The wake models underestimated the power of the turbines in the first column by more than 30 % because they do not account for the global blockage effect. The large discrepancies occurred because the wake models neglect relevant energy sources and sinks, as the energy budget analysis revealed. The LES results showed a large spread of turbine powers inside a turbine column due to the large variability in wind direction caused by the flow deflection and divergence. This effect could not be reproduced by the wake models because they do not model the physical processes that lead to the wind direction variability. The wake models could be improved by modeling some of these physical processes. The greatest improvement would be achieved if the gravity wave induced pressure gradients were taken into account.

6.2 Open research questions

One open research task would be to systematically vary parameters like the BL height, the lapse rate in the free atmosphere and the turbine spacing for the finite wind farm setup. The results could be used for the improvement of existing wake models. Another interesting research task would be to investigate SBLs with a height that is smaller than the height of the wind turbines. This situation will occur more often in the future as offshore wind turbines are still increasing in size. The studies presented in this thesis use stationary and horizontal homogeneous inflow and forcing data. These are conditions that rarely occur in reality. Thus, an important research task would be to use less idealized setups and to investigate the impact of transient events or heterogeneous flow fields. The results of this thesis have shown that the counterclockwise flow deflection increases the energy input by the geostrophic forcing and thus the wind farm performance. An interesting research task would be to find out whether this effect could be enhanced by applying a systematic yaw misalignment to all turbines so that the flow deflection and thus the energy input by the geostrophic forcing increases further.

Acknowledgements

My greatest thanks go to my supervisor Prof. Dr. Siegfried Raasch. I could ask him for advice at any time and I had many constructive discussions with him. His support during the sometimes lengthy publication processes was of great value to me.

I would like to thank the Federal Maritime and Hydrographic Agency for the project funding and for the good cooperation. Many thanks to the North-German Supercomputing Alliance (HLRN) for providing the immense computational resources I needed for the simulations within this thesis.

I would like to thank my colleagues inside and outside the PALM group for the technical and/or entertaining conversations on the way to the mensa or during the coffee break. It was really a great time with you guys! Special thanks to Lara Remmer and Johannes Schwenkel for proofreading my thesis. I thank Björn Maronga and Mostafa Bakhoday Paskyabi for volunteering as coreferents.

Lastly, I would like to thank my wife Henrike. She has motivated and built me up especially in times of slow progress. It is thanks to her tireless and generous support that I was able to complete my thesis so quickly.

Bibliography

- Abkar, M. and Porté-Agel, F.: The effect of free-atmosphere stratification on boundary-layer flow and power output from very large wind farms, *Energies*, 6, 2338–2361, doi: 10.3390/en6052338, 2013.
- Abkar, M. and Porté-Agel, F.: Mean and turbulent kinetic energy budgets inside and above very large wind farms under conventionally-neutral condition, *Renewable Energy*, 70, 142–152, doi: 10.1016/j.renene.2014.03.050, 2014.
- Allaerts, D. and Meyers, J.: Effect of Inversion-Layer Height and Coriolis Forces on Developing Wind-Farm Boundary Layers, in: 34th Wind Energy Symposium, pp. 1–5, American Institute of Aeronautics and Astronautics, Reston, Virginia, doi: 10.2514/6.2016-1989, 2016.
- Allaerts, D. and Meyers, J.: Boundary-layer development and gravity waves in conventionally neutral wind farms, *Journal of Fluid Mechanics*, 814, 95–130, doi: 10.1017/jfm.2017.11, 2017.
- Allaerts, D. and Meyers, J.: Gravity Waves and Wind-Farm Efficiency in Neutral and Stable Conditions, *Boundary-Layer Meteorology*, 166, 269–299, doi: 10.1007/s10546-017-0307-5, 2018.
- Allaerts, D. and Meyers, J.: Sensitivity and feedback of wind-farm-induced gravity waves, *Journal of Fluid Mechanics*, 862, 990–1028, doi: 10.1017/jfm.2018.969, 2019.
- Allaerts, D., Broucke, S. V., van Lipzig, N., and Meyers, J.: Annual impact of wind-farm gravity waves on the Belgian-Dutch offshore wind-farm cluster, *Journal of Physics: Conference Series*, 1037, 072 006, doi: 10.1088/1742-6596/1037/7/072006, 2018.
- Andersen, S. J., Witha, B., Breton, S. P., Sørensen, J. N., Mikkelsen, R. F., and Ivanell, S.: Quantifying variability of Large Eddy Simulations of very large wind farms, *Journal of Physics: Conference Series*, 625, 0–12, doi: 10.1088/1742-6596/625/1/012027, 2015.
- Bleeg, J., Purcell, M., Ruisi, R., and Traiger, E.: Wind farm blockage and the consequences of neglecting its impact on energy production, *Energies*, 11, doi: 10.3390/en11061609, 2018.
- BSH: Entwurf Flächenentwicklungsplan, Tech. rep., Bundesamt für Seeschifffahrt und Hydrographie, Hamburg, URL https://www.bsh.de/DE/THEMEN/Offshore/Meeresfachplanung/Flaechenentwicklungsplan/flaechenentwicklungsplan_node.html, 2022.
- Calaf, M., Meneveau, C., and Meyers, J.: Large eddy simulation study of fully developed wind-turbine array boundary layers, *Physics of Fluids*, 22, 015 110, doi: 10.1063/1.3291077, 2010.
- Calaf, M., Parlange, M. B., and Meneveau, C.: Large eddy simulation study of scalar transport in fully developed wind-turbine array boundary layers, *Physics of Fluids*, 23, doi: 10.1063/1.3663376, 2011.

- Centurelli, G., Vollmer, L., Schmidt, J., Dörenkämper, M., Schröder, M., Lukassen, L. J., and Peinke, J.: Evaluating Global Blockage engineering parametrizations with LES, *Journal of Physics: Conference Series*, 1934, 012021, doi: 10.1088/1742-6596/1934/1/012021, 2021.
- Dai, Y., Basu, S., Maronga, B., and de Roode, S. R.: Addressing the Grid-Size Sensitivity Issue in Large-Eddy Simulations of Stable Boundary Layers, *Boundary-Layer Meteorology*, 178, 63–89, doi: 10.1007/s10546-020-00558-1, 2021.
- Deardorff, J. W.: Stratocumulus-capped mixed layers derived from a three-dimensional model, *Boundary-Layer Meteorology*, 18, 495–527, doi: 10.1007/BF00119502, 1980.
- Dörenkämper, M., Witha, B., Steinfeld, G., Heinemann, D., and Kühn, M.: The impact of stable atmospheric boundary layers on wind-turbine wakes within offshore wind farms, *Journal of Wind Engineering and Industrial Aerodynamics*, 144, 146–153, doi: 10.1016/j.jweia.2014.12.011, 2015.
- Elliott, W. P.: The growth of the atmospheric internal boundary layer, *Transactions, American Geophysical Union*, 39, 1048, doi: 10.1029/TR039i006p01048, 1958.
- Gaertner, E., Rinker, J., Sethuraman, L., Zahle, F., Anderson, B., Barter, G., Abbas, N., Meng, F., Bortolotti, P., Skrzypinski, W., Scott, G., Feil, R., Bredmose, H., Dykes, K., Shields, M., Allen, C., and Viselli, A.: Definition of the IEA Wind 15-Megawatt Offshore Reference Wind Turbine, Tech. rep., National Renewable Energy Laboratory, Golden, CO, URL <https://www.nrel.gov/docs/fy20osti/75698.pdf>, 2020.
- Ghaisas, N. S., Archer, C. L., Xie, S., Wu, S., and Maguire, E.: Evaluation of layout and atmospheric stability effects in wind farms using large-eddy simulation, *Wind Energy*, 20, 1227–1240, doi: 10.1002/we.2091, 2017.
- Hansen, K. S., Barthelmie, R. J., Jensen, L. E., and Sommer, A.: The impact of turbulence intensity and atmospheric stability on power deficits due to wind turbine wakes at Horns Rev wind farm, *Wind Energy*, 15, 183–196, doi: 10.1002/we.512, 2012.
- IEA: World Energy Outlook 2022, Tech. rep., International Energy Agency, URL <https://www.iea.org/reports/world-energy-outlook-2022>, 2022.
- IRENA: Renewable capacity statistics 2023, Tech. rep., International Renewable Energy Agency, Abu Dhabi, URL www.irena.org, 2023.
- Johnstone, R. and Coleman, G. N.: The turbulent Ekman boundary layer over an infinite wind-turbine array, *Journal of Wind Engineering and Industrial Aerodynamics*, 100, 46–57, doi: 10.1016/j.jweia.2011.11.002, 2012.
- Jonkman, J., Butterfield, S., Musial, W., Scott, G., Jonkman, J., Butterfield, S., Musial, W., and Scott, G.: Definition of a 5-MW Reference Wind Turbine for Offshore System Development, Tech. Rep. February, National Renewable Energy Laboratory, doi: 10.2172/947422, 2009.
- Lanzilao, L. and Meyers, J.: Effects of self-induced gravity waves on finite wind-farm operations using a large-eddy simulation framework, *Journal of Physics: Conference Series*, 2265, 022043, doi: 10.1088/1742-6596/2265/2/022043, 2022.
- Lu, H. and Porté-Agel, F.: Large-eddy simulation of a very large wind farm in a stable atmospheric boundary layer, *Physics of Fluids*, 23, 065101, doi: 10.1063/1.3589857, 2011.

- Lu, H. and Porté-Agel, F.: On the Impact of Wind Farms on a Convective Atmospheric Boundary Layer, *Boundary-Layer Meteorology*, 157, 81–96, doi: 10.1007/s10546-015-0049-1, 2015.
- Maas, O.: LES of a 15 GW wind farm, Research Data Repository of the Leibniz University Hannover, [dataset], doi: 10.25835/39jgn8ac, 2022.
- Maas, O.: From gigawatt to multi-gigawatt wind farms: wake effects, energy budgets and inertial gravity waves investigated by large-eddy simulations, *Wind Energy Science*, 8, 535–556, doi: 10.5194/wes-8-535-2023, 2023a.
- Maas, O.: Large-eddy simulation of a 15 GW wind farm: Flow effects, energy budgets and comparison with wake models, *Frontiers in Mechanical Engineering*, 9, 1–23, doi: 10.3389/fmech.2023.1108180, 2023b.
- Maas, O. and Raasch, S.: Wake properties and power output of very large wind farms for different meteorological conditions and turbine spacings: a large-eddy simulation case study for the German Bight, *Wind Energy Science*, 7, 715–739, doi: 10.5194/wes-7-715-2022, 2022.
- Maronga, B., Moene, A. F., van Dinter, D., Raasch, S., Bosveld, F. C., and Gioli, B.: Derivation of Structure Parameters of Temperature and Humidity in the Convective Boundary Layer from Large-Eddy Simulations and Implications for the Interpretation of Scintillometer Observations, *Boundary-Layer Meteorology*, 148, 1–30, doi: 10.1007/s10546-013-9801-6, 2013.
- Maronga, B., Gryschka, M., Heinze, R., Hoffmann, F., Kanani-Sühring, F., Keck, M., Ketelsen, K., Letzel, M. O., Sühring, M., and Raasch, S.: The Parallelized Large-Eddy Simulation Model (PALM) version 4.0 for atmospheric and oceanic flows: Model formulation, recent developments, and future perspectives, *Geoscientific Model Development*, 8, 2515–2551, doi: 10.5194/gmd-8-2515-2015, 2015.
- Maronga, B., Banzhaf, S., Burmeister, C., Esch, T., Forkel, R., Fröhlich, D., Fuka, V., Gehrke, K. F., Geletič, J., Giersch, S., Gronemeier, T., Groß, G., Heldens, W., Hellsten, A., Hoffmann, F., Inagaki, A., Kadasch, E., Kanani-Sühring, F., Ketelsen, K., Khan, B. A., Knigge, C., Knoop, H., Krč, P., Kurppa, M., Maamari, H., Matzarakis, A., Mauder, M., Pallasch, M., Pavlik, D., Pfafferoth, J., Resler, J., Rissmann, S., Russo, E., Salim, M., Schrempf, M., Schwenkel, J., Seckmeyer, G., Schubert, S., Sühring, M., von Tils, R., Vollmer, L., Ward, S., Witha, B., Wurps, H., Zeidler, J., and Raasch, S.: Overview of the PALM model system 6.0, *Geoscientific Model Development*, 13, 1335–1372, doi: 10.5194/gmd-13-1335-2020, 2020.
- Meyers, J. and Meneveau, C.: Large Eddy Simulations of large wind-turbine arrays in the atmospheric boundary layer, 48th AIAA Aerospace Sciences Meeting Including the New Horizons Forum and Aerospace Exposition, doi: 10.2514/6.2010-827, 2010.
- Meyers, J. and Meneveau, C.: Flow visualization using momentum and energy transport tubes and applications to turbulent flow in wind farms, *Journal of Fluid Mechanics*, 715, 335–358, doi: 10.1017/jfm.2012.523, 2013.
- Moeng, C.-H. and Wyngaard, J. C.: Spectral Analysis of Large-Eddy Simulations of the Convective Boundary Layer, *Journal of the Atmospheric Sciences*, 45, 3573–3587, doi: 10.1175/1520-0469(1988)045<3573:SAOLES>2.0.CO;2, 1988.

- Nilsson, K., Ivanell, S., Hansen, K. S., Mikkelsen, R., Sørensen, J. N., Breton, S.-P., and Henningson, D.: Large-eddy simulations of the Lillgrund wind farm, *Wind Energy*, 18, 449–467, doi: 10.1002/we.1707, 2015.
- Platis, A., Siedersleben, S. K., Bange, J., Lampert, A., Bärfuss, K., Hankers, R., Cañadillas, B., Foreman, R., Schulz-Stellenfleth, J., Djath, B., Neumann, T., and Emeis, S.: First in situ evidence of wakes in the far field behind offshore wind farms, *Scientific Reports*, 8, doi: 10.1038/s41598-018-20389-y, 2018.
- Porté-Agel, F., Wu, Y. T., and Chen, C. H.: A numerical study of the effects of wind direction on turbine wakes and power losses in a large wind farm, *Energies*, 6, 5297–5313, doi: 10.3390/en6105297, 2013.
- Porté-Agel, F., Lu, H., and Wu, Y. T.: Interaction between large wind farms and the atmospheric boundary layer, *Procedia IUTAM*, 10, 307–318, doi: 10.1016/j.piutam.2014.01.026, 2014.
- Porté-Agel, F., Bastankhah, M., and Shamsoddin, S.: Wind-Turbine and Wind-Farm Flows: A Review, *Boundary-Layer Meteorology*, 174, 1–59, doi: 10.1007/s10546-019-00473-0, 2020.
- Saiki, E. M., Moeng, C.-H., and Sullivan, P. P.: Large-Eddy Simulation Of The Stably Stratified Planetary Boundary Layer, *Boundary-Layer Meteorology*, 95, 1–30, doi: 10.1023/A:1002428223156, 2000.
- Segalini, A. and Chericoni, M.: Boundary-layer evolution over long wind farms, *Journal of Fluid Mechanics*, 925, 1–29, doi: 10.1017/jfm.2021.629, 2021.
- Smith, R. B.: Gravity wave effects on wind farm efficiency, *Wind Energy*, 13, 449–458, doi: 10.1002/we.366, 2009.
- Steinfeld, G., Witha, B., Dörenkämper, M., and Gryschka, M.: Hochauflösende Large-Eddy-Simulationen zur Untersuchung der Strömungsverhältnisse in Offshore-Windparks, *promet - Meteorologische Fortbildung*, 39, 163–180, 2015.
- Stevens, R. J., Gayme, D. F., and Meneveau, C.: Effects of turbine spacing on the power output of extended wind-farms, *Wind Energy*, 19, 359–370, doi: 10.1002/we.1835, 2016.
- Van Der Laan, M. P. and Nørmark Sørensen, N.: Why the Coriolis force turns a wind farm wake clockwise in the Northern Hemisphere, *Wind Energy Science*, 2, 285–294, doi: 10.5194/wes-2-285-2017, 2017.
- VerHulst, C. and Meneveau, C.: Large eddy simulation study of the kinetic energy entrainment by energetic turbulent flow structures in large wind farms, *Physics of Fluids*, 26, 025 113, doi: 10.1063/1.4865755, 2014.
- Wicker, L. J. and Skamarock, W. C.: Time-splitting methods for elastic models using forward time schemes, *Monthly Weather Review*, 130, 2088–2097, doi: 10.1175/1520-0493(2002)130<2088:TSMFEM>2.0.CO;2, 2002.
- Witha, B., Steinfeld, G., Dörenkämper, M., and Heinemann, D.: Large-eddy simulation of multiple wakes in offshore wind farms, *Journal of Physics: Conference Series*, 555, 12 108, doi: 10.1088/1742-6596/555/1/012108, 2014.
- Wu, K. L. and Porté-Agel, F.: Flow adjustment inside and around large finite-size wind farms, *Energies*, 10, 4–9, doi: 10.3390/en10122164, 2017.

- Wu, Y.-T. and Porté-Agel, F.: Large-Eddy Simulation of Wind-Turbine Wakes: Evaluation of Turbine Parametrisations, *Boundary-Layer Meteorology*, 138, 345–366, doi: 10.1007/s10546-010-9569-x, 2011.
- Wu, Y.-T. and Porté-Agel, F.: Modeling turbine wakes and power losses within a wind farm using LES: An application to the Horns Rev offshore wind farm, *Renewable Energy*, 75, 945–955, doi: 10.1016/j.renene.2014.06.019, 2015.
- Zhang, M., Arendshorst, M. G., and Stevens, R. J.: Large eddy simulations of the effect of vertical staggering in large wind farms, *Wind Energy*, 22, 189–204, doi: 10.1002/we.2278, 2019.

Curriculum Vitae

Personal Details

Name	Oliver Maas
Date of Birth	27.04.1992
Birthplace	Hamburg
Nationality	German

Career

since May 2023	CFD Specialist for Site Simulation and Meteorology, Wobben Research and Development GmbH (Enercon), Bremen, Germany
Mar 2019 – Apr 2023	Research Associate, Institute of Meteorology and Climatology, Leibniz University Hannover, Germany

Education

Feb 2019	Master of Science, Wind Energy Engineering, Leibniz University Hannover, Germany
Oct 2015	Bachelor of Science, Maritime Technologies, main topic Wind Energy Technology, University Bremerhaven, Germany
Mai 2011	General Higher Qualification for University Entrance, Georg-Sonnin-Schule (Technical secondary school), Lüneburg, Germany

Awards

2021	MacCready Award, Congress of the International Scientific and Technical Soaring Organisation, 23 July 2021
------	--

Publications

Journals

Wenz, F., Maas, O., Arnold, M., Lutz, T. and Krämer, E.: Assessment of low-frequency aeroacoustic emissions of a wind turbine under rapidly changing wind conditions based on an aero-servo-elastic CFD simulation, *Wind Energy*, 2023, 1–18, doi: 10.1002/we.2826, 2023.

Gasch, P., Kasic, J. , Maas, O. and Wang, Z.: Advancing airborne Doppler lidar wind profiling in turbulent boundary layer flow – an LES-based optimization of traditional scanning-beam versus novel fixed-beam measurement systems, EGU sphere [preprint], doi: 10.5194/egusphere-2023-548, 2023.

Maas, O.: Large-eddy simulation of a 15 GW wind farm: Flow effects, energy budgets and comparison with wake models, *Frontiers in Mechanical Engineering*, 9, 1–23, doi: 10.3389/fmech.2023.1108180, 2023.

Maas, O.: From gigawatt to multi-gigawatt wind farms: wake effects, energy budgets and inertial gravity waves investigated by large-eddy simulations, *Wind Energy Science*, 8, 535–556, doi: 10.5194/wes-8-535-2023, 2023.

Maas, O. and Raasch, S.: Wake properties and power output of very large wind farms for different meteorological conditions and turbine spacings: a large-eddy simulation case study for the German Bight, *Wind Energy Science*, 7, 715–739. doi: 10.5194/wes-7-715-2022, 2022.

Conference Contributions

Maas, O.: Large-eddy simulation of a 15 GW wind farm and comparison with advanced wake models, EERA DeepWind Conference, 18–20 January 2023, Trondheim, Norway, 2023.

Maas, O. and Raasch, S.: Wake properties and power output of very large wind farms for different meteorological conditions and turbine spacings: A large-eddy simulation case study for the German Bight, *Wind Energy Science Conference*, 25–28 May 2021, Hannover (virtual), Germany, 2021.

Maas, O. and Raasch, S.: Energieertrag und Nachlaufeigenschaften sehr großer Windparks in der Deutschen Bucht: Grobstruktursimulationen für verschiedene meteorologische Bedingungen, *Deutsche Klimatagung*, 15–18 March 2021, Hamburg (virtual), Germany, 2021.

Maas, O. and Raasch, S.: Wake properties and power output of very large wind farms for different meteorological conditions and turbine spacings: A large-eddy simulation case study for the German Bight, *EERA DeepWind Conference*, 13–15 January 2021, Trondheim (virtual), Norway, 2021.

Theses

Maas, O.: Detailed measurements in the atmospheric boundary layer near wind turbines, Master thesis, Leibniz University Hannover, Germany, 2019.

Maas, O.: Development of Software Tools For Improving Mechanical Load Measurements According to IEC 61400-13 Using Lidar Techniques, Bachelor thesis, University Bremerhaven, Germany, 2015.

Other

Maas, O. and Etling, D.: On the influence of moisture on the strength of thermals: A large-eddy simulation case study, *TECHNICAL SOARING*, 45, 20–26, 2021.